Master's thesis

NTNU
Norwegian University of Science and Technology
Faculty of Engineering
Department of Marine Technology

Eivind Hexeberg Dysvik

Experimental and Numerical Study of Non-Linear Motions of Ocean Farm 2 at Inspection Draught

Master's thesis in Marine Technology
Supervisor: Trygve Kristiansen
June 2022

NTNU
Norwegian University of Science and Technology

GLOBAL MARITIME

Eivind Hexeberg Dysvik

Experimental and Numerical Study of Non-Linear Motions of Ocean Farm 2 at Inspection Draught

Master's thesis in Marine Technology
Supervisor: Trygve Kristiansen
June 2022

Norwegian University of Science and Technology
Faculty of Engineering
Department of Marine Technology

NTNU
Kunnskap for en bedre verden

Preface

This thesis finalizes the Master of Science degree in Marine Hydrodynamics at the Department of Marine Technology, Norwegian University of Science and Technology, at Trondheim. The thesis was written in the spring of 2022. The studies consist of experiments and numerical simulations of the Ocean Farm 2 fish farm at inspection draught.

The thesis is written in collaboration with Global Maritime AS. The Ocean Farm 2 is designed by Global Maritime, providing the necessary data and information.

Eivind Hexeberg Dysvik
Trondheim, Norway
June 11, 2022

Acknoledgement

This thesis has been done under the supervision of Professor Trygve Kristiansen at the Department of Marine Technology, NTNU. I highly appreciate the deep knowledge and enthusiasm about hydrodynamics. He has always been available for guidance, even at weekends and late hours. I could not have asked for a better supervisor.

I would also like to thank Vibeke Browne at Global Maritime for proposing the subject for this thesis and providing the necessary information and data. In addition, she was always available for questions and discussions during my work.

Furthermore, Mael Korentin Ivan Morau deserves to be mentioned for instructing me on WAMIT and the generation of the panel models.

The lab team consisting of Emil Bratlie, Torgeir Wahl, Terje Rosten, Trond Innset, Ole Erik Vinje and Robert Opland deserves special recognition. Their guidance during the experiment's planning, setup and execution is highly appreciated.

Lastly, I would like to thank my colleagues and friends at office C 1.076 for creating a fun and social environment.

Abstract

The rapidly growing population and challenges regarding climate change require a significant increase in sustainable food production. Ocean fish farming is an expanding industry which can help mitigate these challenges. Today's industry-standard fish farms in Norway can handle a relatively low sea-state, limiting possible locations to inside fjords. Therefore, to enable further expansion, the farms must be able to handle harsher weather conditions and move to a more exposed location. The Ocean Farm 2 is designed for exposed locations, and its motions at inspection draught are the topic of this thesis.

The freeboard at inspection draught is only 30 cm, which likely makes wave overtopping and pontoon deck flooding occur frequently. These strongly non-linear effects and their implications on the global motion of the structure are studied in this thesis.

The solution strategy to estimate the non-linear motions involves a three-step process. First, estimate the linear motions with WAMIT. Secondly, study wave overtopping and pontoon deck flooding for a 2D cross-section of the bottom pontoon. Lastly, combine the linear solution with non-linear correction factors in a time-domain simulator.

The potential flow solver WAMIT was used for calculating the linear motions. A panel model of the submerged part of the structure was made for this purpose. Surge, heave and pitch motions were found, in addition to added mass, damping, restoring and excitation coefficients. The pressures at each panel from diffraction and radiation were also obtained, which were used in the time-domain simulator to locally correct for wave overtopping and deck flooding.

Experiments were performed on a Froude scaled model with an equal cross-section as the bottom pontoon of Ocean Farm 2. The experiment consists of the fixed model in incident regular waves for studying the excitation forces and forced heave to find added mass and damping. The tests were performed with and without a removable top extension, prohibiting wave overtopping and pontoon deck flooding. The results were compared to establish non-linear correction factors, used later by the time-domain simulator.

Incident waves were also simulated by use of the CFD software OpenFOAM. The mesh and time-step convergence study showed that simulation of small-amplitude waves was the most demanding. The results coincided well with the experiments, especially for increasing wave periods.

Furthermore, a time-domain simulator was established to combine the linear results from WAMIT with the non-linear correction factors found in the experiments and CFD simulations. The simulator corrected the diffraction and radiation pressure depending on the level of wave overtopping and deck flooding at the location of each panel. The restoring stiffness was also adjusted depending on the water plane area, which is significantly reduced when the structure is submerged below the freeboard.

The findings show that wave overtopping cause a reduction in the excitation forces, while pontoon deck flooding results generally in increased added mass and damping. The result of these non-linear effects is a significant reduction in the motion amplitude, and the magnitude depends on the wave steepness. The increased added mass caused the resonance period to shift slightly towards higher wave periods.

Sammendrag

Den raskt voksende befolkningen og utfordringene knyttet til klimaendringer krever en betydelig økt matproduksjon, som må være bærekraftig. Fiskeoppdrett er en ekspanderende næring som kan bidra til å løse disse utfordringene. Dagens standard for oppdrettsanlegg i Norge kan håndtere en relativt lav sjøtilstand, noe som begrenser aktuelle plasseringer til inne i fjorder. Derfor, for å muliggjøre ytterligere vekst må fiskemerdene kunne håndtere tøffere værforhold og flytte til mer utsatte lokasjoner. Ocean Farm 2 er designet for utsatte områder, og dens bevegelser ved inspeksjonsdypgang er tema for denne oppgaven.

Fribordet ved inspeksjonsdypgang er bare 30 cm, hvilket mest sannsynlig gjør at bølger vil overtoppe pontongen og den vil neddykkes ofte. Disse sterkt ikke-lineære effektene og deres implikasjoner på den globale bevegelsen til strukturen er studert nærmere. Metoden for å estimere de ikke-lineære bevegelsene involverer en tre-trinns prosess. Først er de de lineære bevegelsene estimert med WAMIT. Videre er bølge-overtopping og neddykking av pontongene for et 2D-tverrsnitt av bunnpontongen studert. Til slutt er den lineære løsningen kombinert med ikke-lineære korreksjonsfaktorer i en tidsdomene-simulator.

Den potensielle strømningsløseren WAMIT ble brukt for å beregne de lineære bevegelsene. En panel modell av den våte delen av strukturen ble laget for dette formålet. Jag, hiv og stamp bevegelser ble funnet, i tillegg til tilleggs-masse, demping, stivhet og eksitasjonskoeffisienter. Trykkene på hvert panel fra diffraksjon og radiasjon ble også funnet, og ble brukt i tidsdomene-simulatoren for å lokalt korrigere for bølge-overtopping og vann på pontongdekket.

Forsøk ble utført på en Froude-skalert modell med likt tverrsnitt som bunnpontongen til Ocean Farm 2. Forsøkene besto av den fastholdte modellen i innkommende regulære bølger for å studere eksitasjonskreftene og tvunget hiv for å finne tilleggs-masse og demping. Testene ble utført med og uten en avtagbar toppforlengelse, som hindret bølgeovertopping og vann på pontongdekket. Resultatene ble sammenlignet for å etablere ikke-lineære de korreksjonsfaktorene, som ble brukt senere i tidsdomene-simulatoren.

Innkommende regulære bølger ble også simulert ved bruk av CFD-programvaren OpenFOAM. Konvergensstudie av domenets dekomponering og tidssteg viste at simulering av bølger med liten amplitude var mest krevende. Resultatene stemte godt overens med eksperimentene, spesielt for økende bølge perioder.

Videre ble det etablert en tidsdomene-simulator for å kombinere de lineære resultatene fra WAMIT med de ikke-lineære korreksjonsfaktorene funnet i eksperimentene og CFD-simuleringene. Simulatoren korrigerte diffraksjons og radiasjonstrykket avhengig av bølgeovertoppingen og dekkoversvømmelse ved plasseringen av hvert panel. Den gjenopprettende stivheten var også justeres avhengig av vannplanområdet, som reduseres betydelig når strukturen lavere enn fribordet.

Resultatene viser at bølgeovertopping forårsaker en reduksjon i eksitasjonskreftene, mens vann på pontongdekket resulterer generelt i økt tilleggs-masse og demping. Resultatet av disse ikke-lineære effektene er en betydelig reduksjon i bevegelsesamplituden og størrelsen avhenger blant annet av bølgesteilheten. Den økte tilleggs-massen førte til at resonansperioden endret seg litt mot høyere bølgeperioder.

Table of Contents

Nomenclature

ϕ	velocity potential
ω	wave angular frequency
T	wave or oscillation period
ΔT	increment in wave period between runs
t	time
k	wave number
λ	wave length
ζ	wave profile
ζ_a	wave amplitude
H	wave height
ϵ	wave steepness
p_Dyn	dynamic pressure
h	water depth
l	hinge position above tank bottom
S	wave maker stroke
z	vertical coordinate, positive upwards
u	fluid particle velocity
L	characteristic length
ρ	water density
g	acceleration of gravity
S_{0B}	body surface
T_s	surface tension
f_{st}	fraction of surface tension contribution
c_p	wave phase velocity
$c_{p,st}$	wave phase velocity, including surface tension
c_g	wave group velocity
H_p	pontoon height
B_p	pontoon breadth
L_p	pontoon length
f_p	pontoon freeboard
α_f	fraction of water in cell
α	scaling factor
Fr	Froude number
α_E	non-linear excitation factor
α_A	non-linear added mass factor
α_B	non-linear damping factor
dt	time-step
x_E	variable measuring the local degree of wave overtopping
x_{AB}	variable measuring the local degree of pontoon flooding
VCG	vertical center of gravity

σ	surface tension
GM	metacentric height
R_{jj}	radii of gyration in mode j
I_{jj}	moment of inertia in mode j
A_{wp}	water plane area
l_p	distance from wave maker to pontoon
D_p	center to center diameter of pontoon
n_{pan}	number of panels
F	force
p_D	pressure from the diffraction problem
p_j	pressure from the radiation problem in mode j
η_j	motion in mode j
$H(\omega)$	transfer function, RAO
A_{33}	added mass in heave
B_V	viscous damping
B_{WR}	wave radiation damping
A_3	far field wave amplitude
B_{33}	total heave damping
C_{33}	heave restoring coefficient
C_v	coefficient of variance
C_d	drag coefficient
C	Courant number
$\Re\{x\}$	real part of x
$\Im\{x\}$	imaginary part of x

Chapter 1

Introduction

The oceans covers 70 % of the earth. However, only 7 % of the globally consumed protein and 2 % of the consumed calories come from the sea [1]. In addition, seafood generally causes a much lower environmental footprint than land-based meat production. With the global population increasing and climate change being an increasingly pressing issue, we need to produce more food in a sustainable way. Fish farming can be an essential part of the solution. The Norwegian fish farming industry has set a goal of growing five times by 2050 [2]. There is not enough space in the Norwegian fjords to accommodate such an increase, so we need to move to more exposed locations.

The Ocean Farm 2 (OF2) is designed to operate in exposed locations outside the fjords with harsher weather conditions than traditional Norwegian fish farms. Between each cycle of fish stock, the structure will be ballasted up in order to be inspected. It will then float on the bottom pontoon ring with a freeboard of only 30 cm, called the inspection draught. In this condition, wave overtopping and pontoon deck flooding can occur for even modest wave heights. These strongly non-linear effects are not accounted for by linear theory. The goal of the Master Thesis will be to estimate the motions of the Ocean Farm 2 when accounting for wave overtopping and pontoon deck flooding.

1.1 Literature Review

The influence of wave overtopping has been topic of research for several types of marine structures. The research is mainly done by numerical simulations or model tests. Two relevant structures are breakwaters and wave energy converters (WEC) which will be elaborated briefly below.

Breakwaters are coastal defence structures which aim to protect harbours and other infrastructure against waves. It can be both bottom-fixed and floating, depending on the water depth. An important parameter for floating breakwaters is the transmitted waves, which should be as low as possible to give the best protection. The shape of the breakwater is often similar to the rectangular bottom pontoon of the OFM2. T. Kaftis and P. Prinos [3] conducted experiments with rectangular shaped breakwaters and found that wave overtopping occurred for freeboard-/incident wave height less than 0.78 and that wave overtopping resulted in smaller waves being transmitted.

The influence of wave overtopping was studied numerically by K.L. Jeong and Y.G Lee [4] by looking at floating breakwaters with quadratic cross-section. The floating breakwater was moored by a linear spring in the x-direction. The study simulated the floating breakwater with two different freeboards, 0.02 m and 0.01 m, with a wave height of 0.03 m for both cases. The floating breakwater with the least freeboard experienced a higher degree of wave overtopping,

which resulted in reduced motions in surge, heave and roll due to reduced pressure on the weather side.

Wave Energy Converters (WEC) can vary a lot in design and shape, which only makes some of the types relevant for this study. The heave buoy type of WEC has been found most relevant. Especially the ones with a rectangular cross-section which is similar to the pontoon cross-section of the OFM2. D. Short studied a heave buoy WEC numerically and experimentally in Ladertanken at Tyholt for his master thesis [5]. 2^{nd} harmonic forces were found to contribute significantly to the total force in cases with wave overtopping. Furthermore, since the experiments performed by D. Short were done in the same facilities as used in this thesis, the numerical and experimental setup of high relevance is described.

1.2 Scope of Work

The scope of work for this thesis is to estimate the motions of Ocean Farm 2, including the non-linear effects from wave overtopping and pontoon deck flooding. Ideally, a 3D model of the complete should be built and tested in the ocean basin at Tyholt. However, due to the low pontoon freeboard, such a model would need to be very large not to encounter issues regarding surface tension. Such a large model and the facilities needed would be quite costly and, most likely, require much more work than intended for a Master's thesis. Therefore, a three-step approach is chosen instead, which consists of:

1. Computing the motions without considering non-linear effects with the linear potential flow solver WAMIT.
2. Performing experiments and CFD simulations on a 2D cross-section of the pontoon to study the wave-induced forces, added mass and damping.
3. Combine the WAMIT results with non-linear correction factors using strip theory in a time-domain simulator.

1.3 Limitations

- The 2D results from experiments and CFD has been applied to the 3D structure with strip theory
- Experiments and CFD simulations has only considered regular waves.
- All waves tested and simulated hit the pontoon head on. No other wave headings have been tested.
- Surge, heave and pitch is the rigid body motions of interest due to only head sea waves
- Pontoon model held fixed during experiments. In reality, the wave-induced forces will cause motions of the floating structure.
- The waves and flow in the physical wave flume is assumed to be 2D.
- No turbulence model has been applied to the numerical CFD simulations.
- No parameter study with different geometries or levels of freeboard has been performed.
- The waves overtopping the pontoons will hit the legs and braces of Ocean Farm 2, which, most likely, result in increased forces. However, this effect has not been accounted for.
- The time-domain simulator use undisturbed waves to calculate the non-linear correction factors. In reality, the wave pattern from the structure is likely very complex.

1.4 Structure of the Thesis

Chapter 2 describes the relevant theory behind the methods and results presented in this thesis.

Chapter 3 presents the Ocean Farm 2. Dimensions and mass properties are listed together with sketches of the bottom pontoon ring and cross-section of the pontoons.

Chapter 4 gives an overview of WAMIT and its usage in this thesis. The panel model, together with a refinement study, is presented, in addition to the additional inputs specified to WAMIT.

Chapter 5 goes through the numerical CFD simulations with OpenFOAM. This chapter includes mainly a description of the computational domain, solution procedure, convergence study and the post-processing procedure.

Chapter 6 describes the experiments performed in Ladertanken at Tyholt, Trondheim. The model and setup are shown. The instrumentation, error sources, and experimental precision are also described in this chapter.

Chapter 7 presents the non-linear time-domain simulator, which combines the linear motions from WAMIT with non-linear correction factors found in the experiments and CFD simulations.

Chapter 8 presents the results, where a brief discussion follows each finding. The chapter is divided into three parts, presenting the results for each of the three steps: linear motions from WAMIT, 2D experimental and CFD results, and the results from the time-domain simulator.

Chapter 9 provides a conclusion together with a recommendation for further work.

Chapter 2

Theory

This chapter outlines the most relevant theory behind the methods and results presented in this thesis. This includes a brief derivation of the potential flow theory, wave maker theory, the radiation and diffraction problem, the fourth-order Runge-Kutta method, the equations of motion, Froude scaling and surface tension.

2.1 Potential Flow Theory

This thesis focus on wave-induced forces and motions of a floating structure. Therefore, the potential flow theory, including linear and second-order Stokes wave theory, is briefly described below.

We assume the flow to be inviscid, irrotational and incompressible, i.e. an ideal or potential flow. The fluid velocity, in a 2D Cartesian coordinate system, can be described by the derivatives of the velocity potential in each direction, as shown in Equation 2.1 [6].

$$\mathbf{V} = \nabla\phi = \mathbf{i}\frac{\partial\phi}{\partial x} + \mathbf{k}\frac{\partial\phi}{\partial z} \tag{2.1}$$

Since the flow is irrotational, the vorticity vector $\nabla \times \mathbf{V} = 0$ everywhere in the fluid. The assumption about incompressible fluid means that $\nabla \cdot \mathbf{V} = 0$ and yields the fluid to satisfy the Laplace equation, Equation 2.2, everywhere in the domain.

$$\nabla^2\phi = \frac{\partial^2\phi}{\partial x^2} + \frac{\partial^2\phi}{\partial z^2} = 0 \tag{2.2}$$

In addition to the Laplace equation, three boundary value problems must also be satisfied. The first is the bottom boundary condition, Equation 2.3, which states that no flow is to go through the sea bed.

$$\left.\frac{\partial\phi}{\partial z}\right|_{z=-h} = 0 \tag{2.3}$$

Then we have the non-linear dynamic free surface boundary condition in Equation 2.4. This condition demands that the pressure in the fluid at the free surface has to be equal to the ambient pressure.

$$\frac{\partial\phi}{\partial t} + \underbrace{\frac{1}{2}\left[\left(\frac{\partial\phi}{\partial x}\right)^2 + \left(\frac{\partial\phi}{\partial z}\right)^2\right]}_{\text{non-linear}} + g\zeta = 0 \qquad \text{at } z = \zeta \tag{2.4}$$

Lastly, we have the non-linear kinematic free surface boundary condition in Equation 2.5, which require the fluid particles on the free surface to have the same velocity as the free surface, which again ensures them to remain on the free surface.

$$\frac{\partial \zeta}{\partial t} = \frac{\partial \phi}{\partial z} - \underbrace{\frac{\partial \phi}{\partial x}\frac{\partial \zeta}{\partial x}}_{\text{non-linear}} \qquad \text{at } z = \zeta \tag{2.5}$$

The velocity potential, ϕ, has to satisfy the Laplace equation, Equation 2.2, and all boundary conditions, i.e. Equation 2.3, 2.4 and 2.5. In order to be able to solve this including higher orders will we assume that the velocity potential, ϕ, and surface elevation, ζ, can be expressed as perturbation series as shown in Equation 2.6 and 2.7, where $\epsilon = k\zeta_a$.

$$\phi = \epsilon\phi_1 + \epsilon^2\phi_2 + ... \tag{2.6}$$

$$\eta = \epsilon\eta_1 + \epsilon^2\eta_2 + ... \tag{2.7}$$

Substituting the perturbation series into the continuity equation and bottom boundary condition can be done directly. However, the non-linear free surface boundary conditions have to be applied on the free surface, which location is unknown beforehand. In order to approximate the location of the free surface, a Taylor expansion about $z = 0$ is performed and combined with the perturbation series for the free surface boundary conditions.

M. Rahman [7] derived the linear and quadratic solutions using the perturbation series and Taylor expansions. Then, by rearranging the expression, we can write the linear solutions, ϕ_l and ζ_l, as they are defined in the software OpenFOAM [8], as shown in Equation 2.8, 2.9, 2.10 and 2.11. OpenFOAM will be used for CFD simulations to simulate Stokes II waves.

$$\phi_l = \frac{g\zeta_a}{\omega}\frac{\cosh k(z+h)}{\cosh kh}\cos\left(kx - \omega t\right) \tag{2.8}$$

$$\zeta_l = \zeta_a \cos(kx - \omega t) \tag{2.9}$$

Similarly did M. Rahman derive the quadratic solution, ϕ_q and ζ_q, which can be rearranged as shown in Equation 2.10 and 2.11.

$$\phi_q = \frac{3\omega\zeta_a^2}{8}\frac{\cosh 2k(z+h)}{\sinh^4 kh}\sin 2(kx - \omega t) \tag{2.10}$$

$$\zeta_q = k\zeta_a^2\,\frac{3 - \tanh^2 kh}{4\tanh^3 kh}\cos 2(kx - \omega t) \tag{2.11}$$

2.1.1 Linear Wave Theory

The velocity potential and surface elevation, according to linear theory, consist only of the linear solution given in Equation 2.8 and Equation 2.9. Other useful formulas according to linear theory are listed below. The equations for finite water depth are given on the left-hand side, while the equations for infinite water depth are given on the right. The water depth is often taken as deep water when the depth is at least half the wavelength. The equations are taken from Faltinsen (1993) [6]. The wave number is defined as $k = 2\pi/\lambda$, ω is the angular wave frequency, λ is the wavelength, and h is the water depth.

Dispersion relation:

$$\frac{\omega^2}{g} = k \tanh kh \qquad \frac{\omega^2}{g} = k \tag{2.12}$$

Wave length:

$$\lambda = \frac{g}{2\pi} T^2 \tanh \frac{2\pi}{\lambda} h \qquad \lambda = \frac{g}{2\pi} T^2 \tag{2.13}$$

Group velocity:

$$c_g = \frac{\partial \omega}{\partial k} = \frac{g\left(\frac{hk}{\cosh^2(hk)} + \frac{\sinh(hk)}{\cosh(hk)}\right)}{2\sqrt{\frac{gk\sinh(hk)}{\cosh(hk)}}} \qquad c_g = \frac{1}{2}\sqrt{\frac{g}{k}} \tag{2.14}$$

Dynamic pressure:

$$p_{Dyn} = \rho g \zeta_a \frac{\cosh k(z+h)}{\cosh kh} \cos(\omega t - kx) \qquad p_{Dyn} = \rho g \zeta_a \mathrm{e}^{kz} \cos(\omega t - kx) \tag{2.15}$$

Wave steepness:

$$\epsilon = \frac{H}{\lambda} \tag{2.16}$$

2.1.2 Stokes Second-Order Waves

The velocity potential and surface elevation for a Stokes II order wave is the sum of the linear and quadratic terms as shown in Equation 2.17 and Equation 2.18.

$$\phi_{StokesII} = \phi_l + \phi_q = \frac{g\zeta_a}{\omega} \frac{\cosh k(z+h)}{\cosh kh} \sin(kx - \omega t) + \frac{3\omega\zeta_a^2}{8} \frac{\cosh 2k(z+h)}{\sinh^4 kh} \sin 2(kx - \omega t) \tag{2.17}$$

$$\zeta_{StokesII} = \zeta_l + \zeta_q = \zeta_a \cos(kx - \omega t) + k\zeta_a^2 \frac{3 - \tanh^2 kh}{4\tanh^3 kh} \cos 2(kx - \omega t) \tag{2.18}$$

Figure 2.1 shows the Stokes II order wave profile in solid line together with the linear and quadratic terms. It can be observed that the Stokes II order wave has a higher and steeper peak and flatter trough than the linear wave profile.

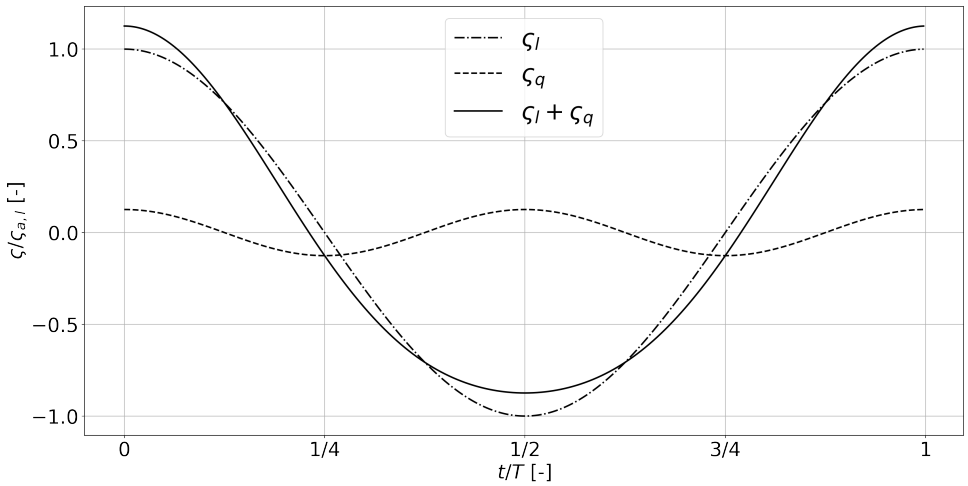

Figure 2.1: Stokes II order wave profile normalized regarding wave period, T, on the horizontal axis and first order wave amplitude, ζ_a, on the vertical axis.

The appropriate wave theory for modelling gravity waves depends on the wave period, wave height, and water depth. For deep water and low steepness, linear potential wave theory is often sufficient to model the processes. However, for increasing steepness and decreasing water depths will the need for a non-linear theory increase. Le Mehaute, 2013 [9] established a figure showing recommended potential wave theories regarding wave height, period and water depth as shown in Appendix B. All waves which are planned to be tested lay within the region covered by Stokes II order potential wave theory. This wave theory will therefore be used in the CFD simulations.

2.2 Wave maker theory

The wave flume to be used in the experiments, Ladertanken at Tyholt, is a single flap hinged wavemaker with the hinge located 0.120 m above the tank bottom. Therefore, the wavemaker theory relevant to this kind of wavemaker is briefly elaborated below.

Dean and Dalrymple (1991) [10] argue that the velocity potential for a wave produced by a wave maker can be established by requiring it to satisfy the Laplace equation and the linearized boundary conditions as elaborated in section 2.1. Furthermore, the velocity potential must also satisfy an additional kinematic condition on the wavemaker flap. The wavemaker is located at $x = 0$. The kinematic condition can then be written as shown in Equation 2.19, which states that the velocity of the fluid located at the wavemaker has to be equal to the wavemaker velocity at the same point. $S(z)$ is the stroke of the wavemaker.

$$u(0, z, t) = \frac{S(z)}{2}\omega \cos \omega t \tag{2.19}$$

S. A. Hughes (1993) [11] derived an expression, Equation 2.20, for the wave height to stroke ratio for a wavemaker with a flap located above the tank bottom as shown in Figure 2.2. S_a is the stroke amplitude, and l is the vertical distance from the tank bottom to the flap hinge. This relation is used to calculate the stroke amplitude, which will be given as input to the wave maker.

$$\frac{H}{S_a} = \frac{4\sinh(kh)}{\sinh(2kh) + 2kh}\left[\sinh(kh) + \frac{\cosh(kl) - \cosh(kh)}{k(h-l)}\right] \tag{2.20}$$

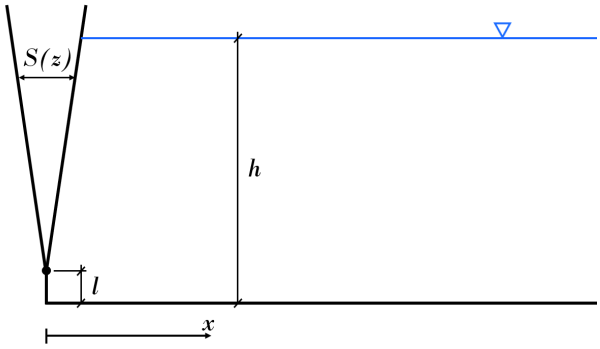

Figure 2.2: Flap type wavemaker hinged above the tank bottom. $z = 0$ is defined at the free surface, positive upwards.

Both Dean and Dalrymple (1991) [10] and S. A. Hughes (1993) [11] used linear theory and assumed small amplitude motions of the flap and small wave heights. Therefore, the generation of large-amplitude waves or high steepness is predicted less accurate than less steep waves. Calibration of the wavemaker based on empirical methods may therefore be necessary to make higher and steeper waves accurately.

The wavemaker in Ladertanken is known to require two additional transfer functions. The first is a mechanical transfer function. The wavemaker may not reach the asked stroke amplitude for high frequency or large stroke amplitudes. Therefore, a frequency-dependent factor must be multiplied to get the stroke amplitude specified. This will be solved by measuring the stroke amplitude for different wave periods and wave heights, comparing the measured stroke with the specified value, and then using the ratio between those as a correction factor. This may be an iterative process. The other factor which has to be compensated for is that the flap does not cover the whole breadth of the wave flume, which is assumed in Equation 2.20. After the mechanical transfer function is found, the second transfer function will be established based on measured wave heights compared with the specified wave height. This transfer function is also frequency-dependent.

2.3 Radiation and Diffraction

In order to analyse the linear motion of a floating structure, the radiation and diffraction problem is to be solved. This will be done with the software WAMIT in this project thesis, and the theory will therefore be outlined below.

Linear potential flow theory is assumed, in addition to deep water, regular incident waves, steady-state condition and zero forward speed. The assumption of linearity and steady-state condition make the superposition principle valid, and the velocity potential can be decomposed into eight problems, one for each of the degrees of freedom, one for the undisturbed incoming wave and one for the diffracted wave. These problems can be solved independently, and the solution will be the sum of each solution.

For the diffraction problem, the body is fixed and interacting with incident waves. The problem is decomposed as shown in equation 2.21 where ϕ_0 is the velocity potential of the undisturbed incident wave, and ϕ_7 is the diffraction term which has to satisfy the impermeability condition given in equation 2.22. The impermeability condition has to be satisfied at the body surface, S_{0B}, which is fixed.

$$\phi_{diff.} = \phi_0 + \phi_7 \tag{2.21}$$

$$\left.\frac{\partial(\phi_0 + \phi_7)}{\partial n}\right|_{S_{0B}} = 0 \tag{2.22}$$

For the radiation problem, there are no incident waves, and the body is instead forced to oscillate in the six degrees of freedom (DOF). The problem is decomposed into six terms, one for each DOF, as shown in equation 2.23. When the body oscillates, it creates radiated waves which cause hydrodynamic and hydrostatic loads on the body. Added mass and damping comes from the hydrodynamic loads and is therefore frequency-dependent. In contrast, the restoring terms come from the hydrostatic loads associated with the change of buoyancy due to the forced body motions. As for the diffraction problem, does the radiation problem have to satisfy the impermeability condition on the body surface, as shown in equation 2.24.

$$\phi_{rad.} = \sum_{j=1}^{6} \phi_j \tag{2.23}$$

$$\left.\frac{\partial \phi_j}{\partial n}\right|_{S_{0B}} = n_j \qquad j = 1...6 \tag{2.24}$$

Then the total wave-body interaction problem can be expressed as the sum of the diffraction and radiation problem as shown in equation 2.25.

$$\phi(x, y, z, t) = \phi_{diff.} + \phi_{rad.} \tag{2.25}$$

2.4 Added Mass and Damping

2.4.1 Added Mass

The added mass is a phenomenon which occur when a body moves in fluids. Especially in water, where the fluid density is significant, will the added mass be important. The added mass is caused by the acceleration of fluid particles nearby the moving body. The fluid particles has to accelerate because they are being pushed by the body. Added mass is frequency dependent and it can even be negative, which means that it is out of phase with the motion of the body.

2.4.2 Damping

Damping is related to energy leaving the system and reducing the structure's motions. Damping is critical around resonance being the only factor limiting the response. The types of damping relevant are wave radiation and viscous damping.

2.4.3 Wave Radiation Damping

Wave radiation damping can be calculated from potential theory, which is done in WAMIT. The potential theory assumes an inviscid flow and is therefore not accounting for viscous damping. The wave radiation damping in heave can be calculated from the far-field radiated wave amplitude, A_3, as shown in Equation 2.26 [6]. The wave can be taken as far-field when it is more than $2B$ from a body with a width of B as a rule of thumb. This can be used to separate the forces from wave radiation damping from the total measured force.

$$B_{33} = \frac{\rho g^2}{\omega^3} \left(\frac{A_3}{|\eta_{3a}|} \right)^2 \tag{2.26}$$

2.4.4 Viscous Damping

Viscous damping includes skin friction and flow separation. This can be estimated by experiments, CFD or by using empirical results for simple geometries. Damping from flow separation is important for structures with sharp corners where the flow easily separates and creates vortices. The pontoons of OF2 have a rectangular cross-section, and it is therefore expected that viscous damping due to flow separation will be significant. The viscous damping can be estimated by the following equation:

$$F_{viscous}(\omega, \eta_{3a}) = \frac{1}{2}\rho C_d A_{wp} \frac{8}{3\pi} \eta_{3a}^2 \omega^2 \tag{2.27}$$

2.5 The 4th Order Runge-Kutta Method

The Runge-Kutta methods are well known ordinary differential equation solvers. The fourth-order method is maybe the most common and will be described in this section. This method will be used in the simulator by solving the equation of motion in time-domain. The equations are taken from C.M. Larsen et al. [12].

The Runge-Kutta methods are an improved version of the Euler's integration method, which can be written as:

$$x_{i+1} = x_i + \dot{x_i} h \tag{2.28}$$

Where $\dot{x_i}$ is the derivative of x_i. The problem with Euler's integration method is that it assumes the derivative to be constant over the time step. This is often not true and can lead to significant numerical errors over time. Therefore, an estimate of the derivative at different times is included. The derivative can be expressed as:

$$f(t, x) = \frac{dx}{dt} \tag{2.29}$$

The fourth-order Runge-Kutta adds an intermediate point defined as:

$$t_{i+0.5} = t_i + \frac{h}{2} \tag{2.30}$$

First, the derivative at the present point is evaluated as:

$$K_0 = f(t_i, x_i) \tag{2.31}$$

Then, the derivative at the first point is used for estimating the derivative at the intermediate point:

$$K_1 = f(t_{i+0.5}, x_i + \frac{h}{2} K_0) \tag{2.32}$$

Further, a better estimate of the intermediate derivative is obtained by:

$$K_2 = f(t_{i+0.5}, x_i + \frac{h}{2} K_1) \tag{2.33}$$

Lastly, the derivative at t_{i+1} is estimated by:

$$K_3 = f(t_{i+1}, x_i + hK_2) \tag{2.34}$$

Finally, the solution for x_{i+1} can be found as the weighed average of the four derivatives:

$$x_{i+1} = x_i + \frac{h}{6}(K_0 + 2K_1 + 2K_2 + K_3) \tag{2.35}$$

If the fourth-order Runge-Kutta method is to be applied to the equation of motions, does it require the problem to be written as a system of first-order equations.

2.6 The equations of motions

The equations of motion for a rigid body can be written as [6]:

$$\sum_{k=1}^{6}[(M_{jk}+A_{jk})\ddot{\eta_k}+B_{jk}\dot{\eta_k}+C_{jk}\eta_k]=F_j \qquad j=1,...,6 \tag{2.36}$$

Where M_{jk}, A_{jk}, B_{jk} and C_{jk} are the mass, added mass, damping and restoring in mode j caused by motion in mode k. F_j is the excitation force.

By assuming harmonic motions can the undamped resonance period be estimated by:

$$T_{n,j}=2\pi\sqrt{\frac{M_{jj}+A_{jj}}{C_{jj}}} \tag{2.37}$$

The rigid body motions is often described by the Response Amplitude Operator (RAO) denoted $H(\omega)$, as defined in Equation 2.38.

$$H_j(\omega)=\frac{\eta_{ja}}{\zeta_a} \tag{2.38}$$

Further, the linear RAOs can be estimated by [12]:

$$\frac{\eta_{3a}}{\zeta_a}=\frac{f_{3a}}{-\omega^2(M+A_{33})+i\omega B_{33}+C_{33}} \tag{2.39}$$

Where ζ_a is the wave amplitude, ω is the wave angular frequency, f_{3a} is the heave excitation amplitude and i is the imaginary unit.

2.6.1 Duffing equation

The Duffing equation is variant of the equation of motion which includes a non-linear restoring term. This second-order differential equation is shown in Equation 2.40 [13]. The equation includes a non-linear restoring term.

$$m\ddot{x}+b\dot{x}+c_1x+c_2x^3=f(t) \tag{2.40}$$

Where m is the mass, b is the damping coefficient, and c_1 and c_2 is restoring coefficients. The time varying excitation force is denoted $f(t)$.

2.7 Equations Governing the CFD Simulations

The Navier-Stokes equations are a set of well-known equations derived from Newton's 2. law. This thesis will not elaborate the full derivation of the theory behind the equations since we are utilizing a well-known CFD program, OpenFOAM. Details regarding how OpenFOAM operates can be found in the documentation [14]. In order to simulate a multiphase flow is the solver *interIsoFoam* used. The Navier-Stokes equations as defined for the *interIsoFoam* solver are shown below [15]. This solver uses the Volume Of Fluid (VOF) method to keep track of the free surface and can apply waves from different wave theories. For example, the Stokes II wave is used in this thesis.

Continuity equation:

$$\frac{\partial u_j}{\partial x_j} = 0 \tag{2.41}$$

Momentum equation:

$$\frac{\partial(\rho u_i)}{\partial t} + \frac{\partial}{\partial x_j}(\rho u_j u_i) = -\frac{\partial p}{\partial x_i} + \frac{\partial}{\partial x_j}(\tau_{ij} + \tau_{tij}) + \rho g_i + f_{\sigma i} \tag{2.42}$$

Where u is the fluid velocity, g the gravitational acceleration, p the pressure, τ_{ij} and τ_{tij} the viscose and turbulent stresses and $f_{\sigma i}$ the surface tension.

The fraction of the two fluids in a cell is defined by α_f, where the value is equal to 1 when it's only water inside it and equal to 0 when it's only air. The combined density of the fluid in the cell is calculated by Equation 2.43.

$$\rho = \alpha_f \rho_1 + (1 - \alpha_f)\rho_2 \tag{2.43}$$

Then *interIsoFoam* solves Equation 2.44 to keep track of the interface, i.e. the free surface.

$$\frac{\partial \alpha}{\partial t} + \frac{\partial(\alpha u_j)}{\partial x_j} = 0 \tag{2.44}$$

The CFD simulations use an adaptable time-step calculated by the Courant number. The Courant number determines the required time-step based on the cell size, Δx, and fluid velocity, u, as shown in Equation 2.45.

$$C = \frac{u\Delta t}{\Delta x} \leq C_{max} \tag{2.45}$$

2.8 Froude Scaling

The Froude number is the ratio between inertia and gravity forces and is defined as shown in Equation 2.46. Equal Froude number ensures that gravity forces are correctly scaled and is often used for gravity-driven waves.

$$\mathrm{Fr} = \frac{u}{\sqrt{gL}} \tag{2.46}$$

When using Froude scaling, the model have the same geometry as the full size structure, and all dimensions are linearly scaled. Other quantities scales according to Table 2.1, taken from E. P.Bachynski [16].

Table 2.1: Scaling factors. Where α is the scaling factor, ρ_m and ρ_f is the water density for the model and full size structure, respectively.

	Scales with	$\alpha = 36$, $\rho_m = \rho_f$
Time	$\sqrt{\alpha}$	6
Length	α	36
Velocity	$\sqrt{\alpha}$	6
Acceleration	1	1
Force	$\alpha^3 \frac{\rho_m}{\rho_f}$	46656
Mass	$\alpha^3 \frac{\rho_m}{\rho_f}$	46656

However, using Froude scaling, the Reynolds number for the flow in model and full scale will be very different. With the scaling factor, $\alpha = 36$, which is used for the experiments and CFD simulations, the full-size Reynolds number will be 216 times larger than in model-scale. Equality in Reynolds number ensures correctly scaled viscous forces, and therefore, may the mismatch in Reynolds number affect the scaling of the results if viscous forces are of importance.

2.9 Surface Tension

For very short waves, effects from surface tension can be significant. This is not a topic of concern for real-world ocean waves because the wavelength is far greater than the ones that are influenced by the surface tension. However, it may be of importance at the model scale. Furthermore, if surface tension not can be neglected for model-scale, will up-scaling of the results be problematic.

The combined free surface condition, when including the surface tension, taken from Faltinsen and Timokha (2009) [17], can be written as:

$$\frac{\partial^2 \phi}{\partial t^2} + g\frac{\partial \phi}{\partial z} - \frac{T_s}{\rho}\frac{\partial^2}{\partial x^2}\frac{\partial \phi}{\partial z} = 0 \qquad \text{on } z = 0 \tag{2.47}$$

When using ϕ as given Equation 2.8 for infinite water depth can the dispersion relation for a wave, including surface tension, be written as [17]:

$$\omega^2 = gk + \frac{T_s}{\rho_w}k^3 \tag{2.48}$$

Then by using the definition of the wave number, $k = 2\pi/\lambda$, and the phase speed:

$$c_p = \frac{\omega}{k} \tag{2.49}$$

We get an expression for the phase speed for a wave where both the gravity and surface tension effects are included as:

$$c_{p,st} = \frac{\lambda}{2\pi}\sqrt{\underbrace{g\frac{2\pi}{\lambda}}_{\text{gravity term}} + \underbrace{\frac{T_s}{\rho_w}\left(\frac{2\pi}{\lambda}\right)^3}_{\text{surface tension term}}} \tag{2.50}$$

Then the fraction of surface tension contribution relative to the sum of gravity and surface tension, f_{st}, can be computed as:

$$f_{st} = \frac{\frac{T_s}{\rho_w}\left(\frac{2\pi}{\lambda}\right)^3}{g\frac{2\pi}{\lambda} + \frac{T_s}{\rho_w}\left(\frac{2\pi}{\lambda}\right)^3} \tag{2.51}$$

When using $T_s = 0.074$ N/m [17] and $\rho_w = 1000$ kg/m^3, the fraction of the surface tension contribution can be plotted as shown in Figure 2.3. For wavelengths of 0.20 m, the surface tension contribution is 0.7 %, which often can be neglected. The shortest wave to be tested is 0.56 m, and the effect of surface tension can therefore be assumed to be negligible.

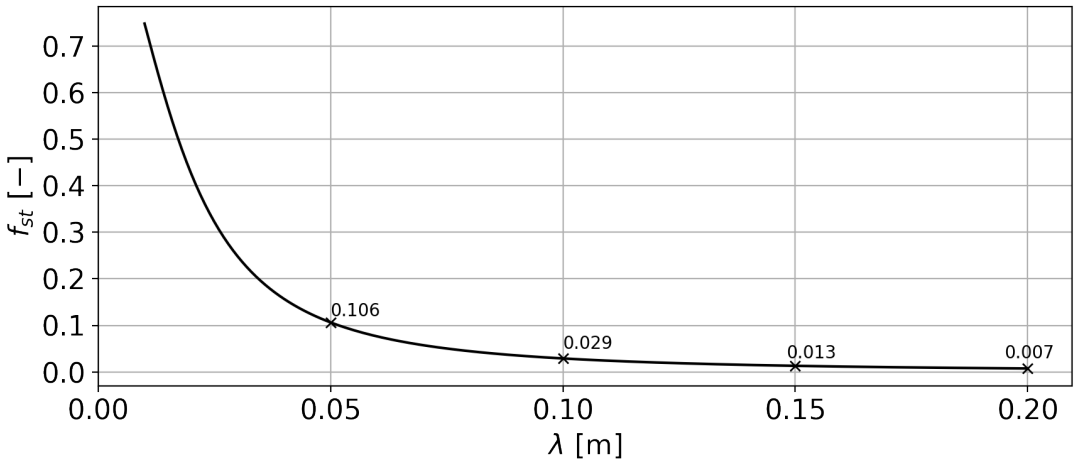

Figure 2.3: Fraction of surface tension contribution relative to the sum of surface tension and gravity contribution. The surface tension contribute only 0.7 % to the phase speed with a wave length of 0.20 m.

Chapter 3

Description of Ocean Farm 2

This chapter describes the Ocean Farm 2 along with its dimensions and mass properties. The data and information presented is provided by Global Maritime AS.

The Ocean Farm 2 (OF2) is shown in Figure 3.1. This is the new generation of Ocean Farm 1, the first fish farm designed for exposed waters when installed in 2017. Global Maritime AS has designed the hull.

3.1 Overview

The design consists of a bottom pontoon and top ring, 12 outer columns, 36 smaller braces between the outer columns, 6 lower braces, 6 upper braces and a centre column. The unit has three draughts: inspection, operation and survival. The topic of this master thesis will be the inspection draught where the structure floats on the bottom pontoon. The freeboard in this condition is 0.3 m and the draught 6.7 m.

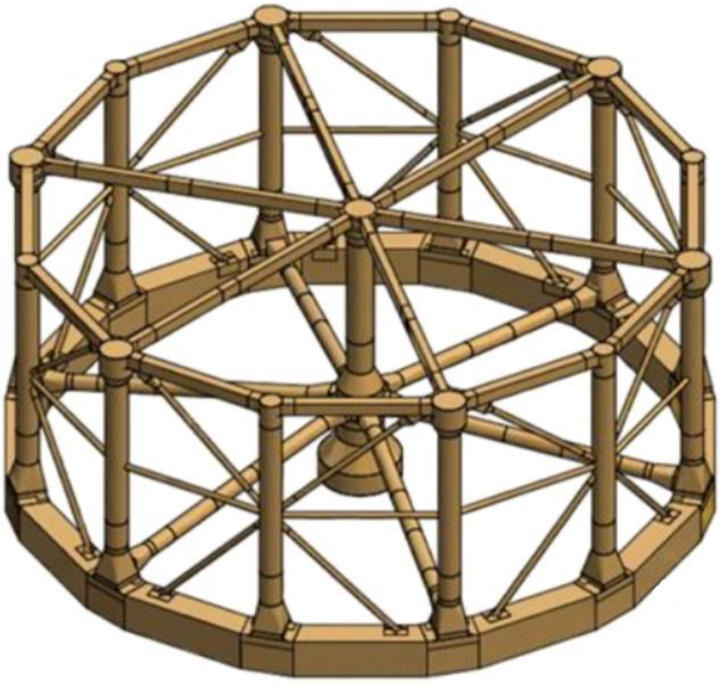

Figure 3.1: Image of Ocean Farm 2 provided by Global Maritime AS.

3.2 Dimensions and Mass Properties

Table 3.1 and 3.2 lists the dimensions and inertia properties of Ocean Farm 2 provided by Global Maritime AS 6$^{\text{th}}$ of October 2021. Potential adjustments applied after this date is therefore not included in this thesis.

Table 3.1: Pontoon and center tank dimensions

	Value	Unit
H_p	7.00	m
B_p	5.00	m
f_p	0.30	m
D_p	115.00	m
$D_{ct,0}$	14.00	m
$D_{ct,1}$	8.00	m
$H_{ct,0}$	4.00	m
$H_{ct,0}$	4.00	m

Table 3.2: Inertia properties. The VCG is defined from the mean free surface, positive upwards.

	Value	Unit
M	12788.4	tonnes
VCG	14.56	m
R_{44}	44.91	m
R_{55}	44.07	m
R_{66}	51.81	m
I_{44}	2.5793E+10	kg m^2
I_{55}	2.4837E+10	kg m^2
I_{66}	3.4328E+10	kg m^2
GM	201	m

The moment of inertia for each mode has been found with Equation 3.1.

$$I_{jj} = MR_{jj}^2 \tag{3.1}$$

A model of the bottom pontoon and centre column based on the dimensions provided by Global Maritime AS are shown in Figure 3.2 and 3.3. The WAMIT panel model is also based on these dimensions. The structure is symmetric about both the horizontal axes.

Figure 3.2 shows a top view of the bottom pontoon. The diameter measured from the center of each pontoons is 115.0 m. The center tank is circular and is connected rigidly to the pontoons by the horizontal braces.

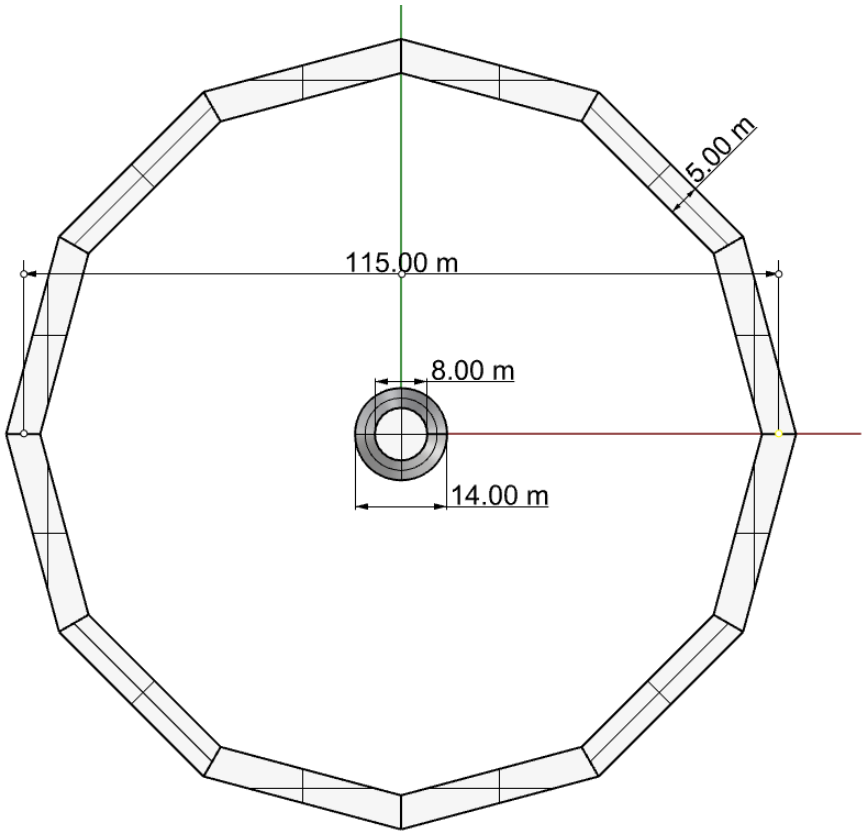

Figure 3.2: Overview over main dimensions of the pontoon and center tank of OF2.

The cross-section of the pontoon and center tank is shown in Figure 3.3a and 3.3b. The pontoon cross-section is 5.0 m wide and 7.0 m high, with a freeboard of only 0.3 m.

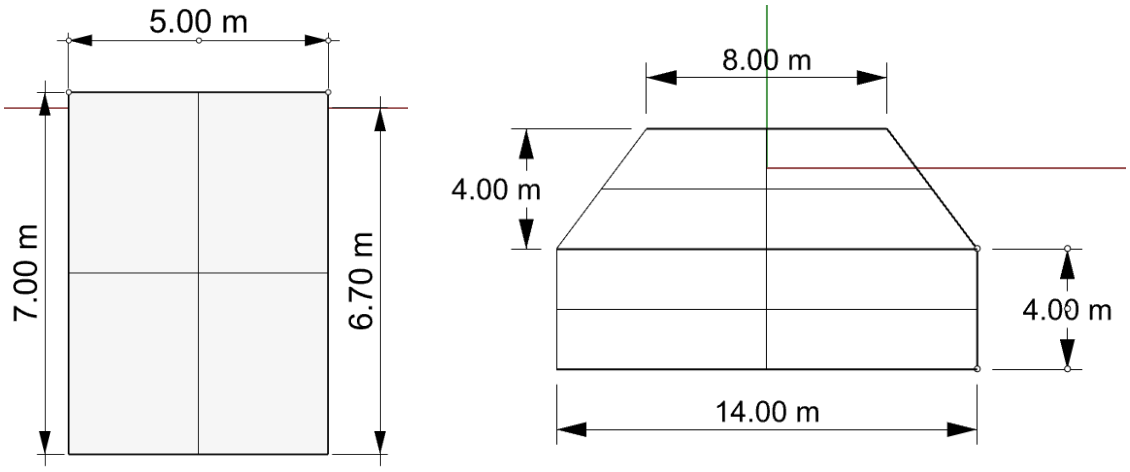

(a) Pontoon

(b) Center tank

Figure 3.3: Dimensions of pontoon cross-section and center tank. The horizontal red line marks the mean free surface.

Chapter 4

WAMIT

This chapter describes the linear potential flow solver WAMIT version 7.4. This panel program is developed for linear analysis of floating or submerged structures in waves.

The submerged part of Ocean Farm 2 was modelled as a panel model, for which WAMIT calculates the linear motions. The results from the WAMIT solver, i.e. the added mass, damping, restoring and excitation, will be used as a basis in the time domain simulator.

4.1 Overview of WAMIT

The linear potential flow solver WAMIT is used to solve the radiation and diffraction problem. The added mass and damping are obtained from the radiation problem, while the excitation forces come from the diffraction problem. Then the results are combined to obtain the rigid body motions, which are presented as RAOs.

WAMIT can output the radiation and diffraction pressure at each panel in complex quantities. This option is used to get added mass, damping and excitation forces locally for each panel. The sum of the pressures multiplied by panel area and normal vectors equals the respective coefficients.

4.2 Methodology

4.2.1 Panel Model

A panel model was first created with the dimensions described in chapter 3. Figure 4.1 shows such a panel model with a total of 1800 panels. The panel models were made by use of a Matlab script developed by Mael Korentin Ivan Moreau. Since WAMIT is a linear potential solver, only the geometry up to the mean water level is needed. The OF2 is symmetric about both the horizontal axis and can therefore be modelled by only one-quarter of the structure and specify the symmetry planes to WAMIT. This reduces the CPU time.

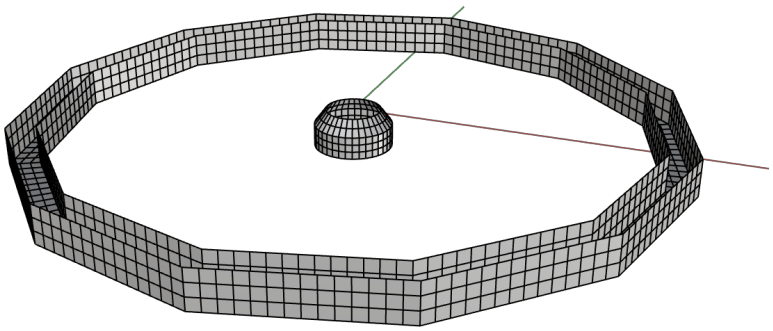

Figure 4.1: Panel model of the submerged part of Ocean Farm 2. The red and green lines are pointing in the positive x- and y-direction, respectively. The waves are propagating in positive x-direction.

4.2.2 Additional WAMIT Inputs

In addition to the panel model, a wide range of inputs can be specified, which are presented in this section.

Only zero heading, i.e. head-on waves, is studied. Therefore, only surge, heave and pitch the motions of interest. However, all modes are enabled for calculation in WAMIT.

The center of gravity is specified to 14.56 m above the mean water level. The mass matrix, $\boldsymbol{M}$, given to WAMIT is shown in Equation 4.1 [6]. I_{46} is zero due to symmetry. The values for M, z_g, I_{44}, I_{55} and I_{66} can be found in section 3.2.

$$\boldsymbol{M} = \begin{bmatrix} M & 0 & 0 & 0 & Mz_g & 0 \\ 0 & M & 0 & -Mz_g & 0 & 0 \\ 0 & 0 & M & 0 & 0 & 0 \\ 0 & -Mz_g & 0 & I_{44} & 0 & -I_{46} \\ Mz_g & 0 & 0 & 0 & I_{55} & 0 \\ 0 & 0 & 0 & -I_{46} & 0 & I_{66} \end{bmatrix} \tag{4.1}$$

No damping or restoring matrices is provided as input. WAMIT calculates the restoring matrix based on the geometry of the panel model. However, stiffness from mooring has to be specified in the restoring matrix as input. This has not been done because the location of the fish farm and thus stiffness properties of the mooring have not yet been found. It is also assumed that the mooring stiffness will be relatively soft, resulting in a low impact on first order motions.

4.3 Mesh Refinement

A mesh refinement study is needed to find the level of mesh size required to get converged results. All panel models were generated using a MATLAB script where one could specify a target number of panels. Therefore, the number of panels for each refinement can be somewhat odd. The structure is symmetric about both horizontal axes, which WAMIT can utilize for faster computational time [18]. The number of panels described below is therefore given as the number of panels for one-quarter of the structure. Figure 4.2 shows the mesh sizes of three of the panel models used in the refinement study.

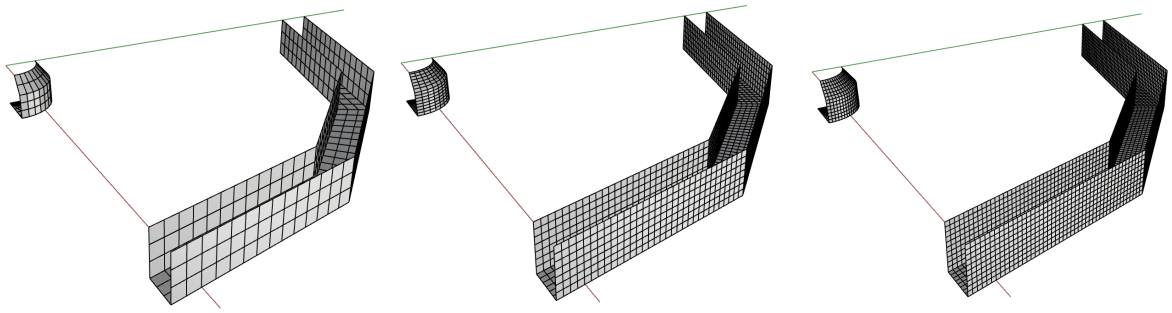

(a) 450 panels **(b)** 2093 panels **(c)** 4074 panels

Figure 4.2: Mesh of the submerged part of OFM2 to be used in WAMIT.

The heave RAO and added mass are shown in Figure 4.3 and 4.4, respectively, for the different panel models tested. The heave RAO does not differ much with respect to the number of panels. However, the model with 1070 panels has a local peak at around T=4.6 s, which is not present for any of the others. This panel model should therefore not be used.

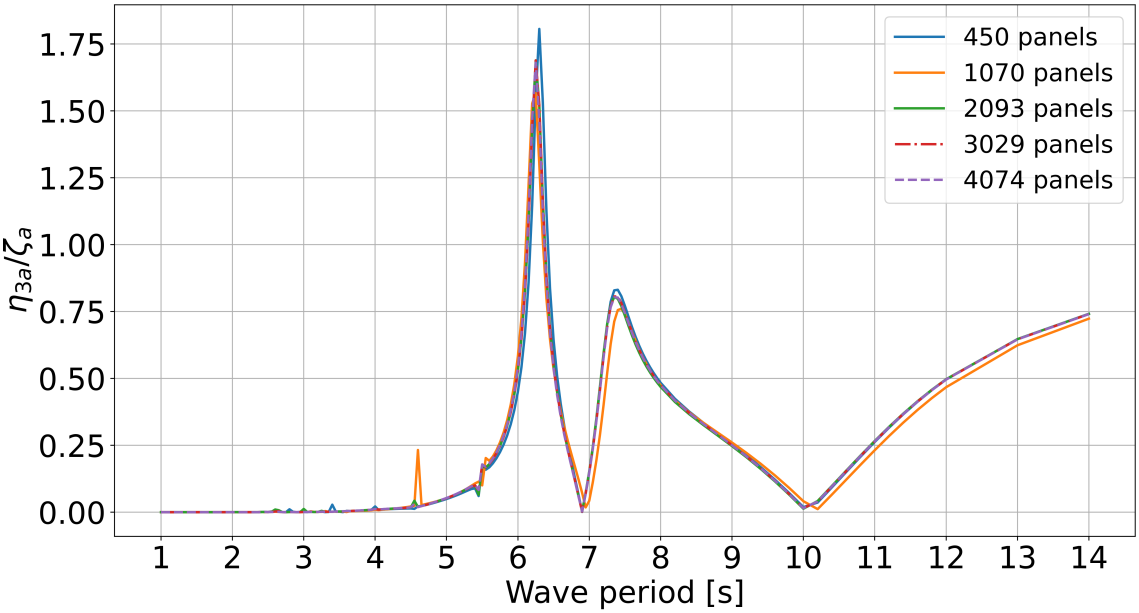

Figure 4.3: Mesh refinement study of heave RAO.

The heave added mass, shown in Figure 4.4, shows slightly more differences than the heave RAO. The models with 2093, 3029 and 4074 panels give similar added mass values for incident wave periods above 4 seconds. Furthermore, in the panel model with 2093, there are some negative peaks of negative added mass for T = 2.5 s - 3.5 s, which are not found in the other cases. Only minor differences are observed between the results from the model with 3029 and 4074 panels.

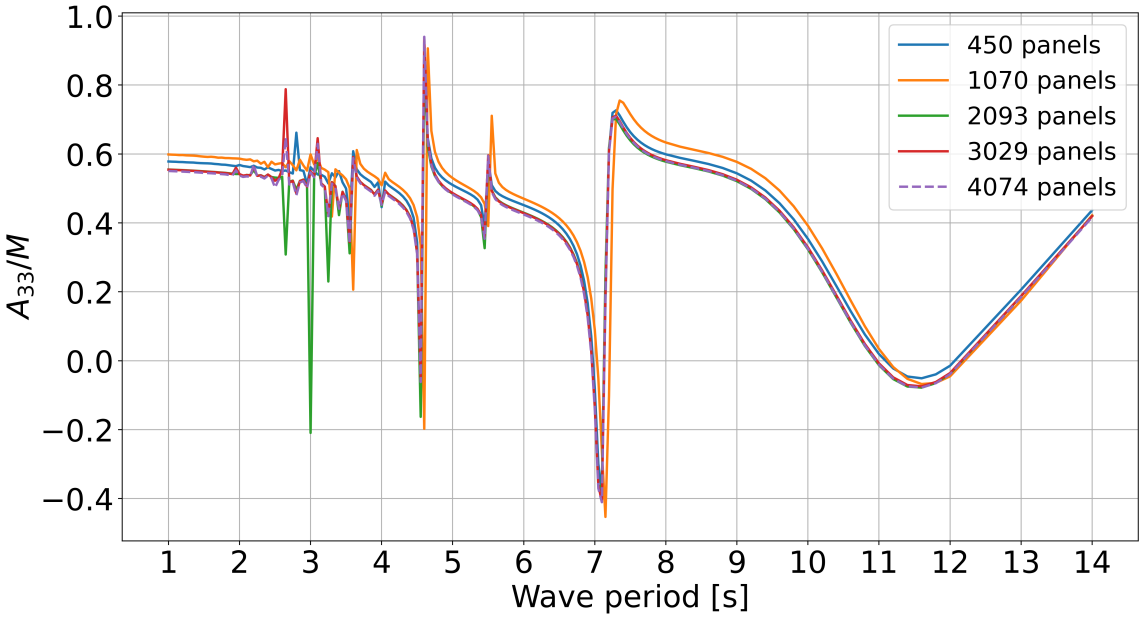

Figure 4.4: Mesh refinement study of added mass in heave.

Other WAMIT results, such as the damping and RAO for pitch and surge, have been studied for the different number of panels. They all show convergence for the models with 2093, 3029 and 4074 panels. Thus we can conclude that the results have converged for the model with 4074 panels, which are chosen for the further studies.

4.4 Limitations and Assumptions

The potential flow theory, as elaborated in Section 2.1, assumes inviscid, irrotational and incompressible flow. Especially the assumption about inviscid flow may be a problematic simplification in our case. The bottom of the pontoons has sharp corners, which will create flow separation and vortices. This effect is not captured by WAMIT and can therefore be a source of error relative to the real world.

Chapter 5

CFD with OpenFOAM

This chapter describes the Computational Fluid Dynamics (CFD) solver OpenFOAM along with the settings and setup of the CFD simulations. The objective is to replicate the experiment described in chapter 6 to get additional results. It is not expected that the results match each other exactly, but the order of magnitude should be approximately the same.

The CFD software OpenFOAM (version 2106) is a common and well-known program. It is open-source, and many different tutorial cases which can be adjusted as needed are available. The case to be simulated is a fixed pontoon in incident waves. The Stokes II tutorial [19] was used as a basis and modified thereafter. Initially, the forced heave case was also planned to be replicated with CFD as well, but this was not done due to limited time.

A total of 12 waves are simulated. The waves simulated has a steepness of 1/60, 1/45 and 1/30 and periods of 1.0 s, 1.1 s, 1.2 s and 1.3 s.

5.1 Computational Domain

Figure 5.1 shows the domain used for all simulations, which is in 2D. The domain is 10.00 m long and 2.00 m high, with 1.00 m water depth. The waves propagate from left to right as indicated by the inlet and outlet. The pontoon model is positioned with the centre of the pontoon at 5.00 m from both the inlet and outlet.

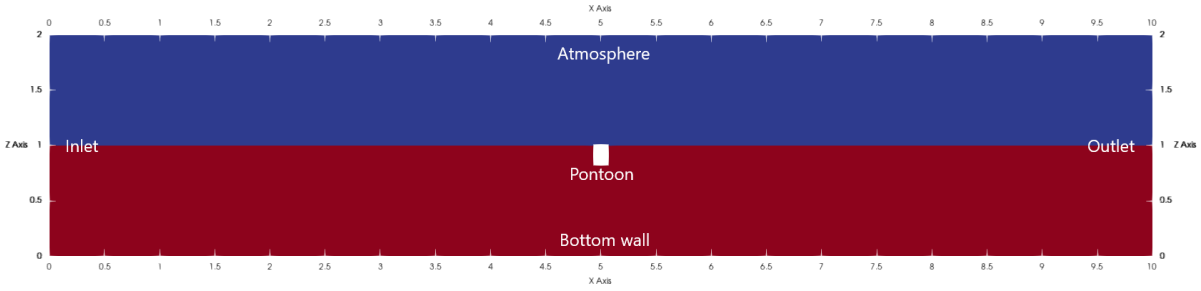

Figure 5.1: Numerical wave flume for CFD analysis. The domain is 10.00 m long, 2.00 m high and 0.59 m wide. The water depth is 1.00 m.

The bottom wall and pontoon surface have a no-slip boundary condition. The atmosphere is modelled with a boundary condition called *pressureInletOutletVelocity* which assigns a zero-gradient condition for flow out of the domain, and the flow into the domain is based on the flux in the normal direction [20]. The inlet boundary is a built-in wave generation boundary called *waveVelocity* which can generate Stokes waves up to the fifth order. Second-order waves are, according to Le Mahaute [9], found to be appropriate for the waves planned to be simulated in

this study. The outlet is modelled with an absorption boundary condition called *shallowWater-Absorption*. This absorption condition shall dampen out the waves and avoid reflection.

The pontoon was modelled as a .STL file which can be read by the *snappyHexMesh* command. Rhinoceros was used for creating the .STL file. The dimensions of the pontoon are the same as for the physical model used in the experiments. The height is 194 mm, the breadth 139 mm, and the freeboard is 9 mm.

Both air and water are defined as Newtonian fluids, with a kinematic viscosity of $1.48{\cdot}10^{-5}$ m^2/s and $1.0{\cdot}10^{-6}$ m^2/s and density of 1.2 kg/m^3 and 1000 kg/m^3, respectively. Surface tension, σ, is set to 0.07 N/m.

5.2 Solver and Numerical Schemes

5.2.1 Solver

The multiphase solver *interIsoFoam* is utilised with the Stokes II order wave inlet boundary condition. This is a modified version of the *interFoam* solver. They both use the volume of fluid (VOF) method for surface tracking and can be used on two-phase incompressible flows. The *interIsoFoam* solver is different from *interFoam* by adding a isoAdvector scheme which gives a sharper interface between the two phases [21]. It is important for this study to have a sharp interface because of the low freeboard and to model the wave overtopping as accurately as possible.

A number of different solvers are available for solving the systems of equations. The Geometric-Algebraic multi-grid (GAMG) method, which is the default method in the tutorial case, is used for the pressure matrices with a DICG Gauss-Seidel smoother. The preconditional biconjugate gradient solver, PBiCG, is used for the velocity. The PBiCG is also the default in the tutorial case.

The function *interfaceHeight* calculates the free surface elevation at specified points, while the *forces* function gives the vertical and horizontal forces acting on the pontoon by integrating the pressure over the body. Here, both viscous and pressure forces are included.

5.2.2 Numerical Schemes

The schemes used in the tutorial case of Stokes II waves from *interFoam* were used as a basis, and most schemes were kept as the default. The Euler time derivative scheme, *ddtSchemes*, the Gauss linear-gradient scheme, *gradSchemes* and linear interpolation scheme, *interpolation-Schemes*, were kept the same as for the tutorial case. The divergence scheme, *divSchemes*, was also kept the same with a Gauss linear upwind gradient scheme for the velocity, Gauss van Leer scheme for the interface variable α and Gauss linear schemes for the density and pressure. The Laplacian scheme was changed from Gauss linear orthogonal to the Gauss linear corrected scheme. Furthermore, the surface normal gradient schemes, *snGradSchemes*, were changed from orthogonal to the corrected scheme.

5.3 Turbulence Model

The sharp edges of the pontoon model are expected to create a lot of vortices. The flow in these vortices is highly turbulent, and a turbulent model should definitely be used. The Reynolds-Averaged Navier Stokes (RANS) k-omega turbulence model [22] was implemented in the OpenFOAM simulations, but it caused significant wave dissipation. A buoyancy modified k-omega model exists, which reduces this effect. The buoyancy modified turbulence model was studied for regular breaking waves by B. Devolder et al. [23] and was found to reduce the wave damping. However, this version was not found as an option in the OpenFOAM tutorials and required

to be implemented by modifying the source code. Time limitations and insufficient knowledge of how to implement the buoyancy modifications hindered this implementation. Therefore, no turbulence model was implemented in the simulations, which is a weakness of this numerical setup.

5.4 Solution Procedure

The simulations are run in Ubuntu using different commands. This section lists the different commands used. A remote computer with 72 cores has been used for the simulations to speed up the computation time. Here, 45 processors have been utilised for all simulations.

1. A background mesh is generated with *blockMesh*
2. The geometry from the .STL file is extracted with *surfaceExtract*
3. *snappyHexMesh* is used to introduce the pontoon model and refine the mesh around the pontoon and free surface
4. *extrudeMesh* is transforming the mesh from 3D to 2D
5. The *setFields* command defines the regions with water
6. *decomposePar* is used to decompose the domain to use multiple processors
7. The following command is then used for running the simulations: *mpirun -np N interIsoFoam -parallel > log &*, where N=45 is the number of processors used.
8. *reconstructPar* is finally run to reconstruct the solution from the different processors

5.5 Convergence Study

A convergence study regarding mesh size and time step has to be performed to ensure both quantities are small enough for the solution to be independent of both. The solution has converged when further refinement of mesh size and time step does not change the result.

Initially, the larger waves were assumed to require the most refined mesh and time-step. This assumption was made based on the hypothesis that waves causing the most violent overtopping, i.e. the larger waves, would demand the most refinement. However, it later showed that the mesh and time step appropriate for the larger waves gave poor agreement with the experimental results for the small waves. Small waves require a fine mesh and small time steps to get modelled accurately. Therefore, a second mesh and time step refinement were needed for the smallest waves.

The original idea was to run CFD simulations of waves with periods of 0.60 s, 1.00 s and 1.30 s with steepness of 1/100, 1/60, 1/45 and 1/30. However, the waves with periods of 0.60 s and steepness of 1/100 proved to be very computationally demanding to get modelled accurately. Moreover, since the topic of interest in this thesis is wave overtopping, the focus was shifted towards the periods from 1.0 s and above and steepness of 1/60 and steeper.

This section will further describe the two mesh and time step refinements. Two waves are chosen for the refinement study with characteristics as listed in Table 5.1. With a period of 1.3 s, the first wave is chosen because it causes significant overtopping of the pontoon model. The second wave with a period of 1.0 s is the smallest wave to be simulated and will test that the mesh and time step is small enough to correctly model the wave height of only 2.6 cm. The strictest level of mesh size and time step will then be chosen for the simulations.

Table 5.1: Wave characteristics for mesh refinement study.

T [s]	ϵ [-]	λ [m]	H [m]
1.0	1/60	1.56	0.026
1.3	1/45	2.60	0.058

5.5.1 Mesh Refinement

The different mesh sizes simulated are listed in Table 5.3. A background mesh with each cell spanning 0.04 m × 0.04 m was first generated by the use of the command *blockMesh*. The different refinement levels are halves of the length in each direction. So a mesh level 1 means each cell within this region is 0.02 m × 0.02 m, and so on. The width/height of each refinement level are listed in Table 5.2. The refinements are applied on the free surface and around the pontoon with the command *snappyHexMesh*.

Table 5.2: Width and height of the refinement levels.

Refinement level	Cell width/height [cm]
1	2.0000
2	1.0000
3	0.5000
4	0.2500
5	0.1250
6	0.0625

Table 5.3: Mesh levels for mesh refinement study.

Mesh	Free surface refinement	Cells per H=0.058 m	Cells per H=0.026	Body refinement	Cells over pontoon height	Cells
1	Level 1	2.9	1.3	Level 2	19	26524
2	Level 2	5.8	2.6	Level 2	19	65881
3	Level 2	5.8	2.6	Level 3	39	74201
4	Level 3	11.6	5.2	Level 3	39	207968
5	Level 3	11.6	5.2	Level 4	78	219620
6	Level 3	11.6	5.2	Level 5	155	240987
7	Level 4	23.2	10.4	Level 5	155	692094
8	Level 5	46.4	20.8	Level 6	155	1661816

The forces on the pontoon were then found by pressure integration around the body for each time step. In order to remove mean forces and noise from the time series, a Fourier transformation was performed with a band pass filter, including frequencies between 0.2 and 4 times the wave frequency. Then an inverse Fourier transformation was performed on that frequency spectrum to get the time series without the mean level and noise. The time series of the inverse Fourier transformation of the horizontal and vertical force is shown in Figure 5.2.

5.5.2 Time-Step Refinement

The time step is controlled by the Courant number, which means that it changes depending on the fluid velocities relative to the cell size according to Equation 2.45. The simulations are run with different Courant numbers to find the required level. An upper limit of 0.01 s was set for the time step. The Courant number should also be less than 1.0 to avoid the fluid from passing through more than one cell per time step.

5.5.3 Convergence for Simulations with Significant Overtopping

The first refinement study was done with waves with ϵ=1/45, T=1.3 s and H=0.058 m. This wave caused significant wave overtopping.

Mesh Convergence

Different mesh refinement levels were first tested with a fixed Courant number of 0.2. The results are shown in Figure 5.2 and show that even mesh 1 models the forces quite well. Appendix C zooms in at Figure 5.2 in addition to plots of the first, second and third harmonic forces.

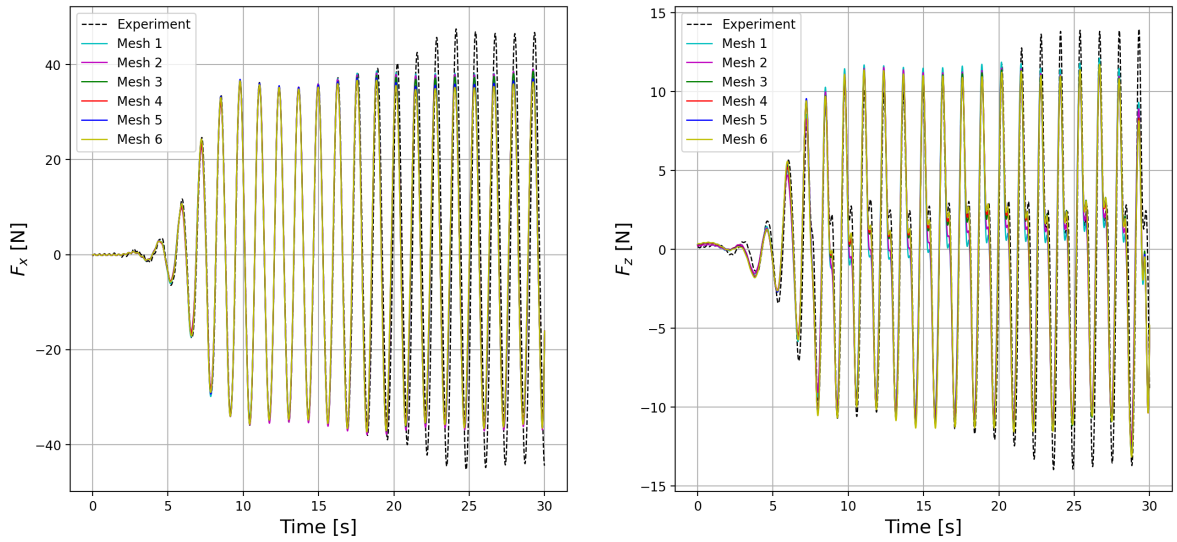

(a) F_x **(b)** F_z

Figure 5.2: Forces on pontoon for waves with ϵ=1/45, H=0.058 m, T=1.3 s. The Courant number was set to 0.2 for all cases. A Fourier transformation with a cut-off of 0.2 and 4 times the wave frequency has been applied. The experimental force amplitudes increase after around 20 s due to wave reflection. This is not occurring for the CFD results because of the absorption boundary at the outlet. The experimental pontoon forces after 20 s are not included in the assumed steady-state interval.

The vertical force shows more variation regarding the mesh refinement level. Especially for the second peak between each maximum and minimum is the difference between each refinement level noticeable. Table 5.4 lists the harmonic force amplitudes for each refinement level.

Table 5.4: Harmonic forces for the mesh refinement study of waves with ϵ=1/45, H=0.058 m, T=1.3 s.

	Fx			Fz		
	1st	2nd	3rd	1st	2nd	3rd
Mesh 1	34.852	2.455	1.065	8.521	3.483	0.857
Mesh 2	35.357	2.555	1.079	8.979	3.337	0.795
Mesh 3	34.817	2.391	1.106	8.666	3.504	0.849
Mesh 4	34.721	2.335	1.079	8.706	3.414	0.846
Mesh 5	35.075	2.391	1.105	8.655	3.567	0.800
Mesh 6	34.737	2.550	1.133	8.680	3.741	0.765
Experiment	35.386	2.448	1.021	8.407	3.787	0.930

The results are assumed to have converged for mesh 5, which are used further in the time step refinement study. Figure 5.3 shows mesh 5 while Figure 5.4 shows a close-up the meshing around the pontoon with mesh 5.

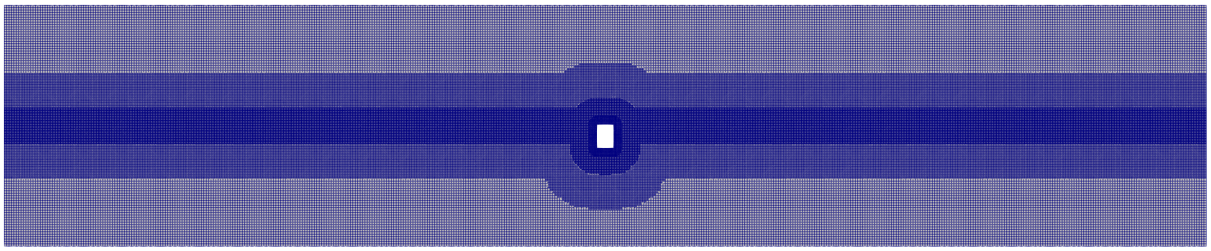

Figure 5.3: Mesh 5

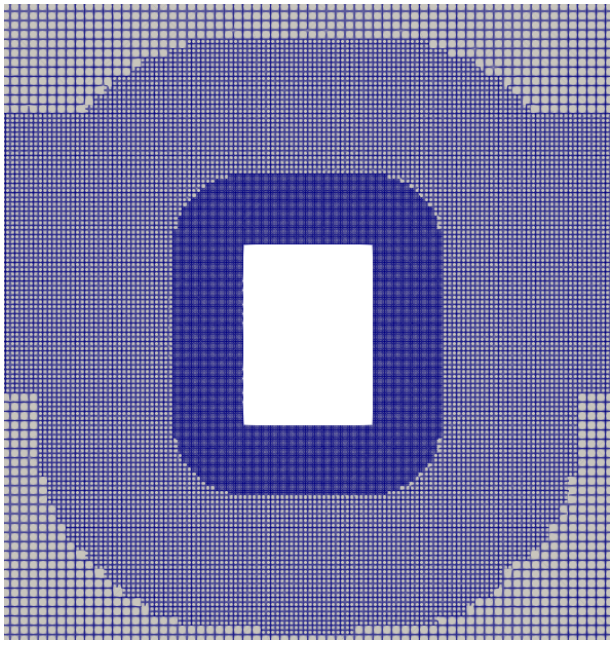

Figure 5.4: Mesh 5, close-up of meshing around the pontoon.

Time-Step Refinement

Courant numbers ranging from 1.0 to 0.1 was tested for the time step refinement study. Appendix D shows a zoomed in version of Figure 5.5 between 10 s and 15 s..

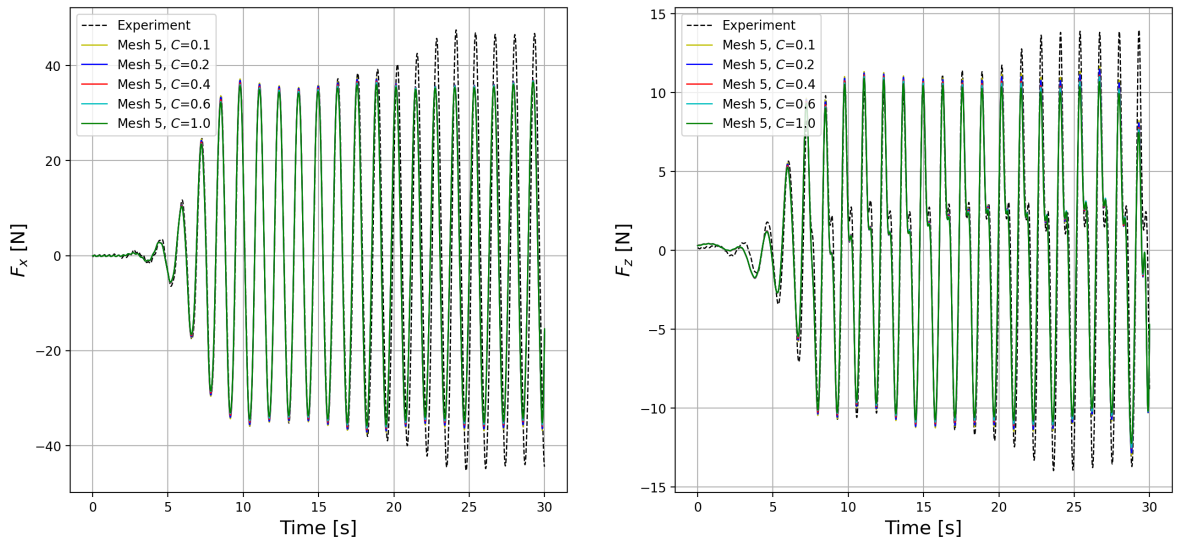

(a) F_x **(b)** F_z

Figure 5.5: Forces on pontoon for waves with ϵ=1/45, H=0.058 m, T=1.3 s. A Fourier transformation with a cut-off of 0.2 and 4 times the wave frequency has been applied. The experimental force amplitudes increase after around 20 s due to wave reflection. This is not occurring for the CFD results because of the absorption boundary at the outlet. This means that the experimental pontoon forces after 20 s are not included in the assumed steady-state interval.

Table 5.5 list the harmonic force amplitudes for each Courant number. The result showed little dependency regarding different Courant numbers. Even though the Courant number of 1.0 shows satisfying results, the Courant number of 0.6 is chosen because the Courant number should be less than 1.0 as mentioned above.

Table 5.5: Harmonic forces for the time-step refinement study of waves with ϵ=1/45, H=0.058 m, T=1.3 s.

	Fx			Fz		
	1st	2nd	3rd	1st	2nd	3rd
C=1.0	33.989	2.303	1.078	8.400	3.374	0.743
C=0.6	34.377	2.333	1.083	8.495	3.447	0.767
C=0.4	34.658	2.355	1.092	8.551	3.494	0.780
C=0.2	35.075	2.391	1.105	8.655	3.567	0.800
C=0.1	35.289	2.408	1.112	8.714	3.602	0.813
Experiment	35.386	2.448	1.021	8.407	3.787	0.930

Computational Time

Another essential factor to consider is the computational time, which increases drastically for finer mesh and time-step. Table 5.6 list the execution time for each of the different configurations of mesh and time-steps in the convergence study. The chosen combination of mesh 5 and Courant number of 0.2 took 3 hours and 37 minutes to get a 30 s simulation.

Table 5.6: Computational time of 30 s simulation time.

	Courant number	Execution time
Mesh 1	0.2	33 min
Mesh 2	0.2	37 min
Mesh 3	0.2	1 h, 17 min
Mesh 4	0.2	1 h, 40 min
Mesh 5	1.0	1 h, 25 min
Mesh 5	0.6	1 h, 39 min
Mesh 5	0.4	2 h, 2 min
Mesh 5	0.2	3 h, 37 min
Mesh 5	0.1	7 h, 22 min
Mesh 6	0.2	8 h, 3 min
Mesh 7	0.2	16 h, 30 min

5.5.4 Convergence for Simulations with Small Waves

As mentioned at the beginning of this section, initially was the convergence study only performed on the wave with ϵ=1/45, T=1.3 s and H=0.058 m. The assumption behind this decision was that the significant overtopping these waves caused would be hard to simulate accurately and thus had the strictest mesh size and time step requirements. However, when mesh 5 and Courant number of 0.2 were used for simulating smaller waves, the resulting pontoon forces differed significantly from the experimental results. This demanded a closer look at the mesh and time-step requirements for simulating small waves.

The pontoon forces were much lower than anticipated, and this was due to the waves being lower than the height specified. Therefore, the wave amplitudes are studied closer in the following convergence study. The pontoon is removed from the numerical domain, and consequently, the mesh refinement is only applied on the free surface. Figure 5.6 shows mesh 5 without the pontoon model as an example of how the numerical domain looks like without the pontoon. This makes it possible to measure the waves at the point where the pontoon model will be positioned later. This is also the same procedure used for calibrating the experimental wave maker. The computational time also decreases significantly when the pontoon is not present.

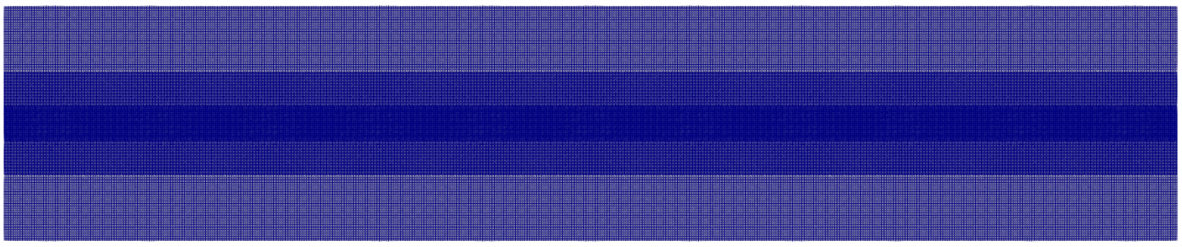

Figure 5.6: Mesh 5 without pontoon model.

The smallest wave planned for the simulations with ϵ=1/60, H=0.026 m and T=1.0 s were run with different mesh sizes and time-steps. Figure 5.7a and 5.7b shows the surface elevation with different mesh and Courant numbers, respectively. It can be observed that the wave heights depend significantly on both variables. The coarser the mesh and time-steps, the lower the waves are.

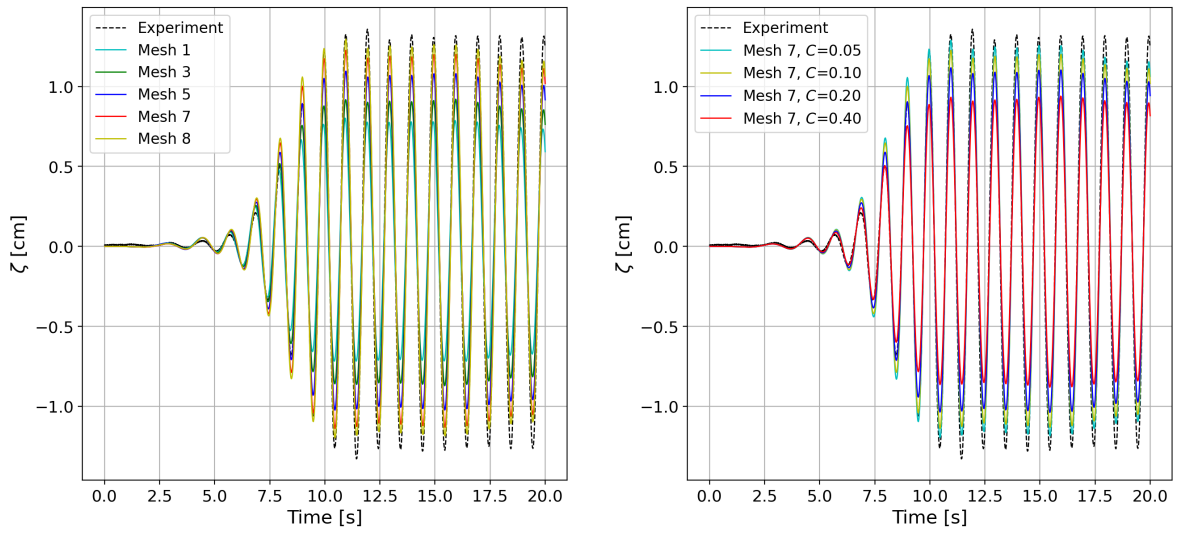

(a) Mesh refinement with C=0.10.

(b) Time-step refinement with mesh 7.

Figure 5.7: Free surface elevation at x=5.0 m for domain without pontoon model. ϵ=1/60, H=0.026 m, T=1.0 s.

Table 5.7 and 5.8 lists the wave heights measured 5.0 m from the inlet for different mesh sizes and Courant numbers, respectively. The wave heights have not converged for either the mesh or time-steps. On the other hand, the wave height approaches the target wave height of 2.6 cm for each refinement.

Table 5.7: Wave heights for different levels of mesh refinement. The results are calculated from the time series of the surface elevation shown in Figure 5.7a.

	Mesh 1	Mesh 3	Mesh 5	Mesh 7	Mesh 8	Experiment	Target value
H [cm]	1.46	1.74	2.04	2.26	2.37	2.57	2.60

Table 5.8: Wave heights with mesh 7 for different Courant numbers. The results are calculated from the time series of the surface elevation shown in Figure 5.7b.

Courant number	0.40	0.20	0.10	0.05	Experiment	Target value
H [m]	1.77	2.08	2.26	2.36	2.57	2.60

Finer mesh than mesh 8 or lower Courant numbers lower than 0.05 was not simulated due to the large computational time needed. Table 5.9 lists the execution time for the different combinations of mesh and Courant numbers used in this convergence study. Mesh 8 demands, for example, nearly six times the execution time as for mesh 7 with the same Courant number. Furthermore, these execution times are for the domain without the pontoon present. The domain with the pontoon model is expected to be more computationally demanding. Later, it was found that the execution time with mesh 7 with the pontoon model present and Courant number of 0.2 was 29 hours, 53 minutes and 56 seconds. That is around 15 times longer than without the pontoon present.

The combination of mesh 7 and Courant number of 0.10 was found to be the best combination available as a compromise between accuracy and computational efficiency. At the same time, it is known that the waves produced with this combination are around 13 % lower than the target

wave height of 2.60 cm, which is expected to affect the pontoon forces. However, the waves are assumed to be modelled increasingly more accurately for increasing wave heights.

Table 5.9: Computational time of 20 s simulation time.

	Courant number	Execution time
Mesh 1	0.10	5 min, 5 s
Mesh 3	0.10	12 min, 17 s
Mesh 5	0.10	45 min, 6 s
Mesh 7	0.05	2 h, 50 min, 34 s
Mesh 7	0.10	1 h, 58 min, 15 s
Mesh 7	0.20	54 min, 5 s
Mesh 7	0.40	41 min, 30 s
Mesh 8	0.10	11 h, 24 min, 6 s

5.5.5 Conclusion of Convergence Study

The conclusion of the convergence study is that mesh 7 and Courant number of 0.1 is chosen for all simulations. The limitations this combination has for small waves are discussed above. Figure 5.8 shows the entire domain with mesh 7, while Figure 5.9 shows a close-up of the meshing around the pontoon with mesh 7.

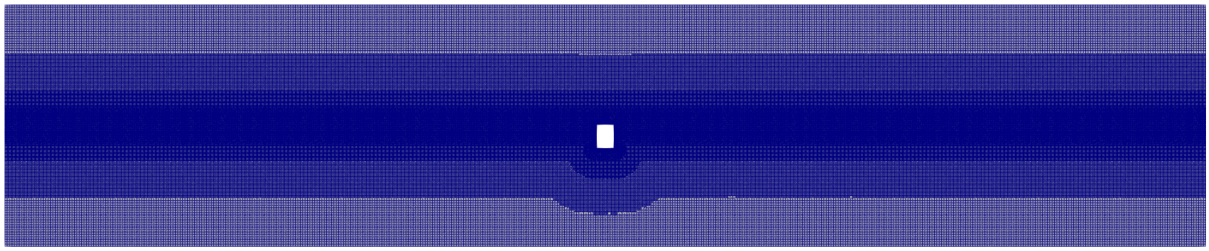

Figure 5.8: Mesh 7

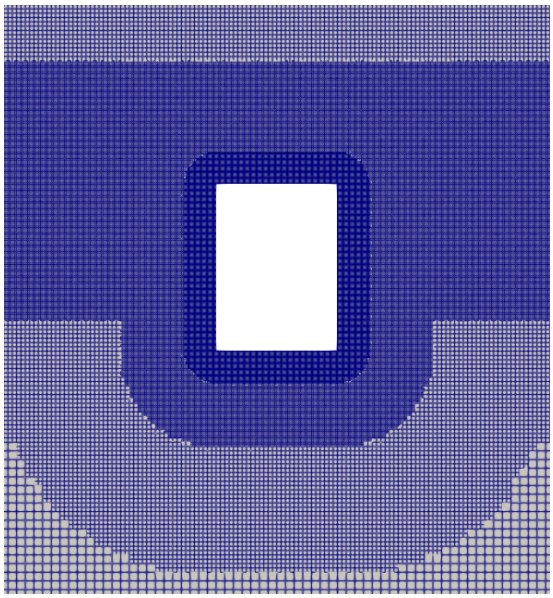

Figure 5.9: Mesh 7, close-up of meshing around the pontoon.

5.6 Wave Characteristics for Simulation

Table 5.10 lists the wave characteristics which are simulated in model- and full scale. The waves are generated as Stokes II order waves. All waves simulated were also tested in the experiment.

Table 5.10: Wave characteristics for OpenFOAM simulation.

T_{model} [s]	$T_{fullscale}$ [s]	ϵ [-]	λ_{model} [m]	H_{model} [m]	$\lambda_{fullscale}$ [m]	$H_{fullscale}$ [m]
1.0	6.0	1/30	1.56	0.052	56.2	1.87
		1/45	—"—	0.035	—"—	1.25
		1/60	—"—	0.026	—"—	0.94
1.1	6.6	1/30	1.88	0.063	67.7	2.27
		1/45	—"—	0.042	—"—	1.51
		1/60	—"—	0.031	—"—	1.11
1.2	7.2	1/30	2.23	0.074	80.28	2.66
		1/45	—"—	0.050	—"—	1.80
		1/60	—"—	0.037	—"—	1.33
1.3	7.8	1/30	2.60	0.087	93.6	3.12
		1/45	—"—	0.058	—"—	2.08
		1/60	—"—	0.043	—"—	1.56

5.6.1 Validity of Stokes Second-Order waves

Figure 5.10 shows a time series of the free surface elevation from the experiment, CFD simulation, and the theoretical Stokes II order wave with ϵ=1/30, H=0.087 m, T=1.3 s. Figure 5.11 shows a zoomed-in version of three periods from the same time series. The figures show that both time series match the shape of the theoretically Stokes II wave, which further strengthens the assumption that this wave theory is appropriate for the waves and water depth used in this study.

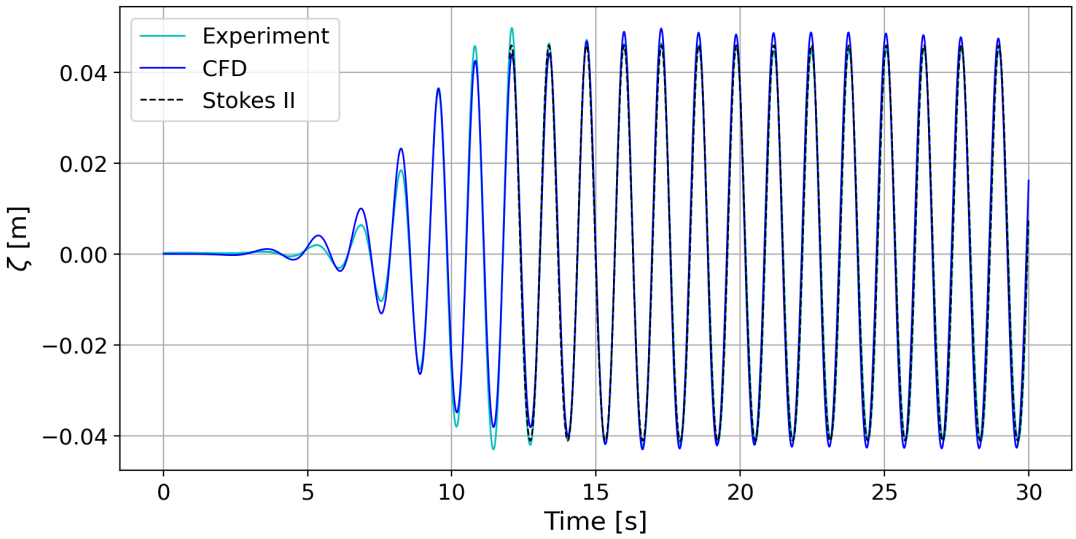

Figure 5.10: Free surface elevation from experiment and CFD at x=6.7 m compared with the theoretical Stokes II wave theory as defined in Equation 2.18. The wave has ϵ=1/30, H=0.087 m, T=1.3 s.

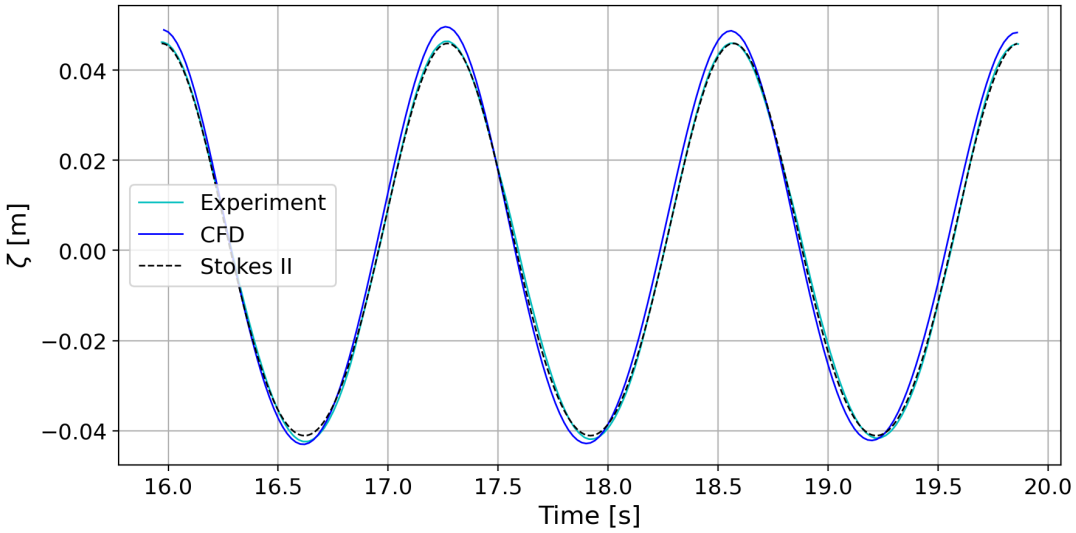

Figure 5.11: Free surface elevation from experiment and CFD at x=6.7 m compared with the theoretical Stokes II wave theory as defined in Equation 2.18. The wave has ϵ=1/30, H=0.087 m, T=1.3 s.

5.7 Post-Processing

The *forces* function in OpenFOAM returns time series of the vertical and horizontal forces for each simulation. This section goes through the post-processing of these force time series. The force time seires from the experiments are analyzed following the same methodology. Figure 5.12 shows, as an example, the time series of the vertical force for waves with ϵ=1/45, T=1.3 s and H=0.058 m. A band passed filter from 0.2ω to 4ω has been applied. Then a steady-state interval is chosen to analyze the harmonic forces. For the experiments, the chosen interval must be before the waves reflected off the back wall reach the model. On the other hand, for the OpenFOAM simulations, is this not a problem due to the boundary condition at the back wall.

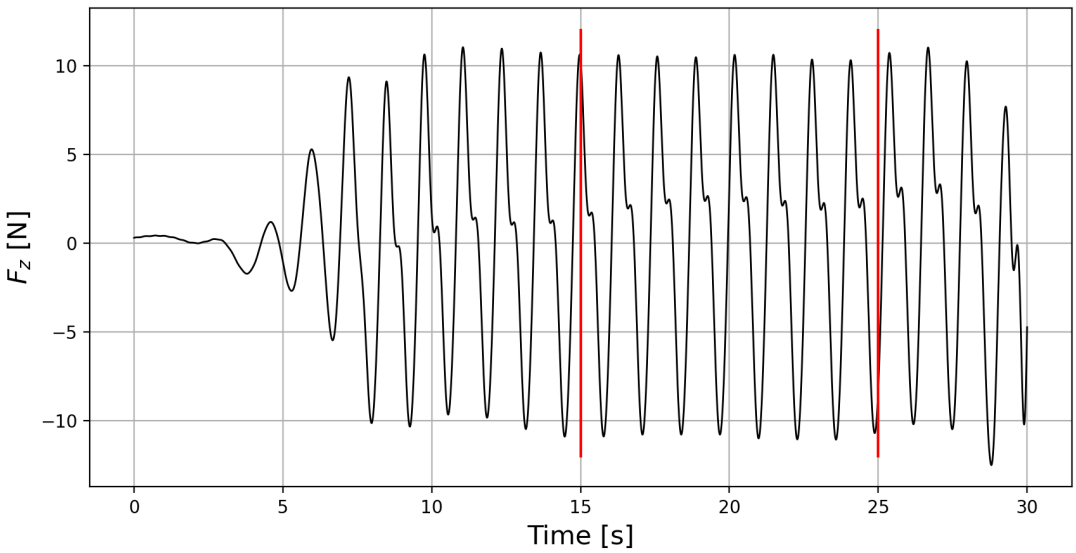

Figure 5.12: Time series of vertical force on the pontoon for incident waves with ϵ=1/45, T=1.3 s and H=0.058 m. Steady-state is assumed between 15 s and 25 s.

A Fourier transformation of the steady-state interval is performed using the *scipy* package in Python to get the frequency spectrum, as shown in Figure 5.13. The frequency spectrum shows

distinct peaks around $n \cdot \omega$, where n =1,2 and 3 and ω is the wave frequency.

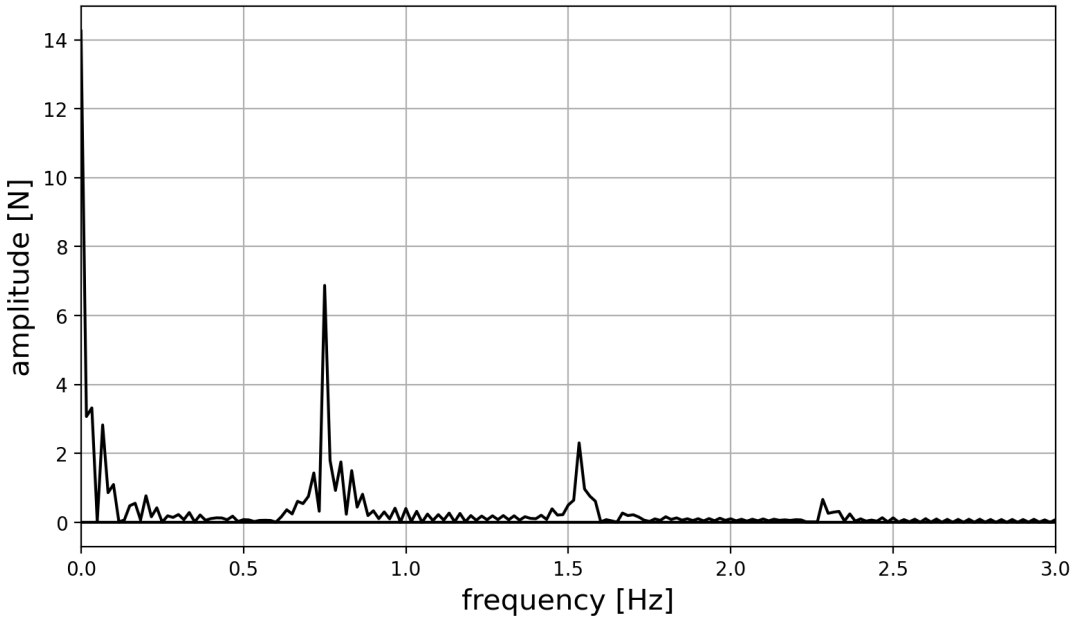

Figure 5.13: The frequency spectrum for the vertical force with $\epsilon = 1/45$, $T = 1.3$ s and $H = 0.058$ m is an example of a typical frequency spectrum for the vertical force with distinct peaks at the harmonic frequencies.

Then time series of the different order of force harmonics is obtained by taking the inverse Fourier transform around the frequency peaks. The band pass filters applied around each harmonic frequency were from 0.8 ω to 1.2 ω for the first harmonic and from 1.8 ω to 2.2 ω for the second, and from 2.8 ω to 3.2 ω for the third harmonic. The harmonic time series are shown in Figure 5.14.

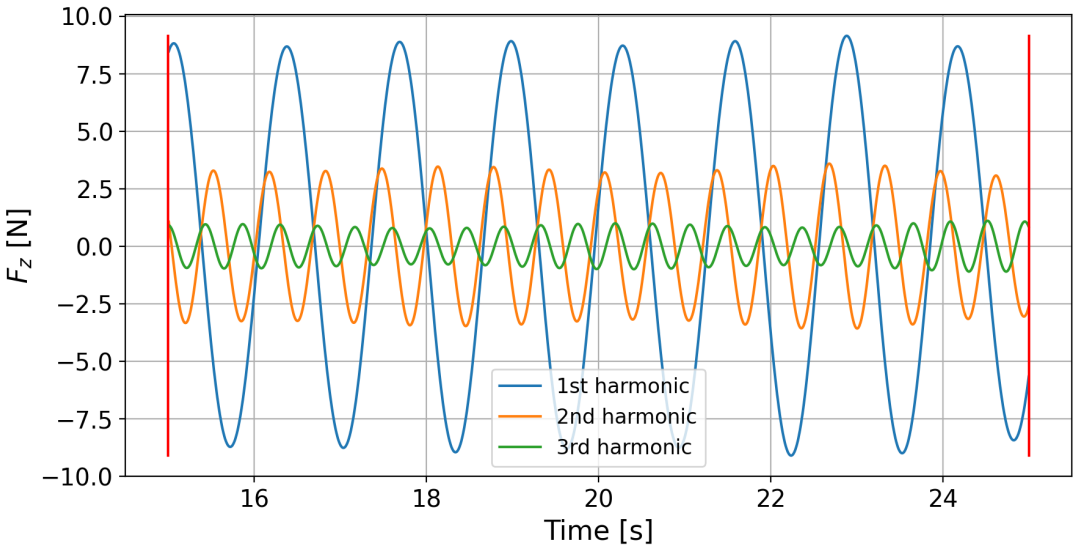

Figure 5.14: Time series of first, second and third harmonic vertical forces from waves with ϵ=1/45, T=1.3 s and H=0.058 m during steady state.

Lastly, the time series from the inverse Fourier around each frequency peak is studied to find the mean force amplitudes.

Chapter 6

Experiments

This chapter presents the experimental setup for the tests with incident waves and forced heave. The pontoon model is described with and without the top extension. The instrumentation, wave maker calibration, post-processing, possible error sources and experimental precision are also included.

The experiment consists of testing:

- Fixed model in regular waves
- Forced heave oscillations in calm water

The purpose of the model test is to study the forces acting on the pontoon in regular waves and added mass and damping from forced oscillation in the heave. For the test with incoming waves, the pontoon will be fixed. Therefore, the weight distribution of the model is not of importance. Furthermore, for the forced oscillation test in heave, the pontoon will oscillate with different amplitudes and frequencies.

6.1 Pontoon Model, Connection Rig and Beach

6.1.1 Pontoon Model

The model has the same cross-section as the bottom pontoons of the Ocean Farm 2. The pontoon height, H_p, and breadth, B_p, are Froude scaled with a scale of 1:36. The pontoon length, L_p, is 1.0 cm short of the wave flume breadth to have a small clearance to the walls. The model freeboard is 9 mm. Figure 6.1 shows a sketch of the pontoon model with dimensions. In addition are the dimensions listed in Table 6.1.

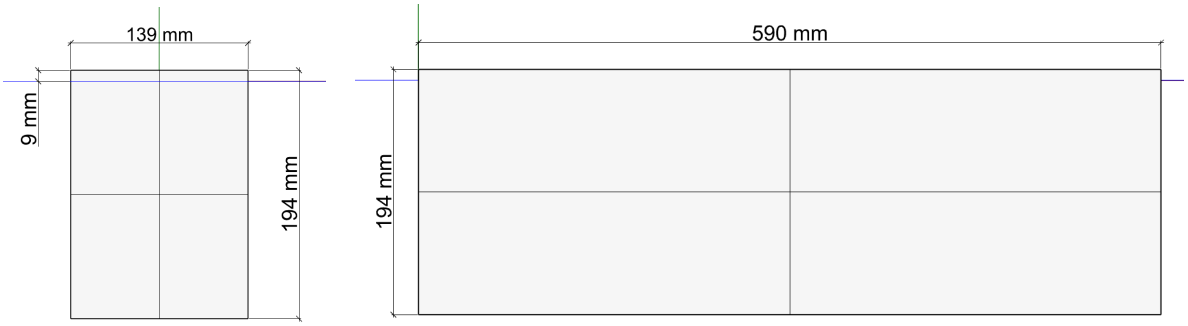

Figure 6.1: Model for testing in Ladertanken. Model scale of 1:36. The horizontal blue line marks the mean water level.

Table 6.1: Pontoon dimensions and weight.

	Full scale	Model scale
H_p	7.00 m	194 mm
B_p	5.00 m	139 mm
L_p	-	590 mm
f_p	0.30 m	9 mm
f_p	-	15.2 kg

The model was fixed to a connection rig with two L-shaped steel braces as shown in Figure 6.2a and 6.2b. The braces were designed to have a low projected area in the wave direction to influence the flow as little as possible. The grid at the braces has an increment of 2.0 cm. The leftmost vertical grid line is 2.0 cm from the leading edge of the pontoon, while the lowest horizontal grid line is 2.0 cm from the pontoon deck. The grid spacing on the pontoon model is 3.0 cm with zero-reference at the mean free surface.

A removable top extension (TE) was mounted on top of the pontoon to avoid wave overtopping and deck flooding. Figure 6.2b and Figure 6.2d shows the pontoon with the top extension. The height of the top extension is 10.0 cm. The top extension was sealed off with tape to avoid water filling. The grid spacings on the top extension are 2.0 cm, starting at the pontoon deck.

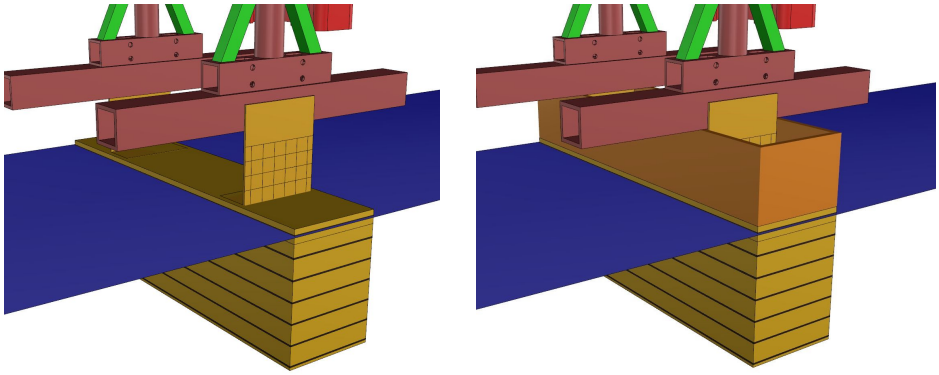

(a) 3D model, without top extension.

(b) 3D model, with top extension.

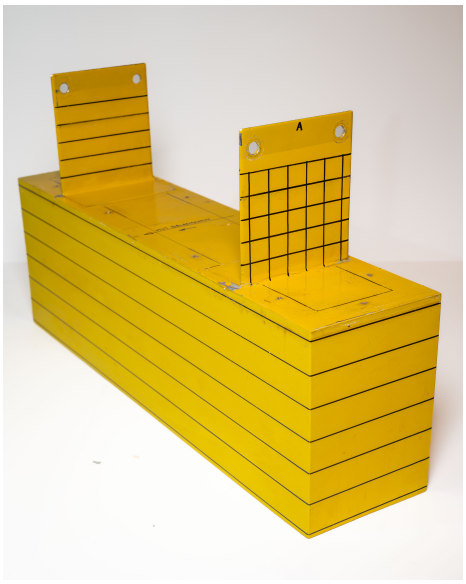

(c) Physical model, without top extension.

(d) Physical model, with top extension.

Figure 6.2: The pontoon model with and without top extension (TE). The top extension was attached to avoid flooding and wave overtopping effects. Both the 3D- and physical models were made by Trond Innset. The grid increment on the pontoon is 3.0 cm, while they are 2.0 cm at the connection brace and top extension.

6.1.2 Connection Rig

The connection braces were mounted to an aluminium framework connecting it to the rig as shown in Figure 6.3 and 6.4. The rig was again connected to the trolley via a motor to move the rig and model vertically. This motor was used for the heave oscillation tests.

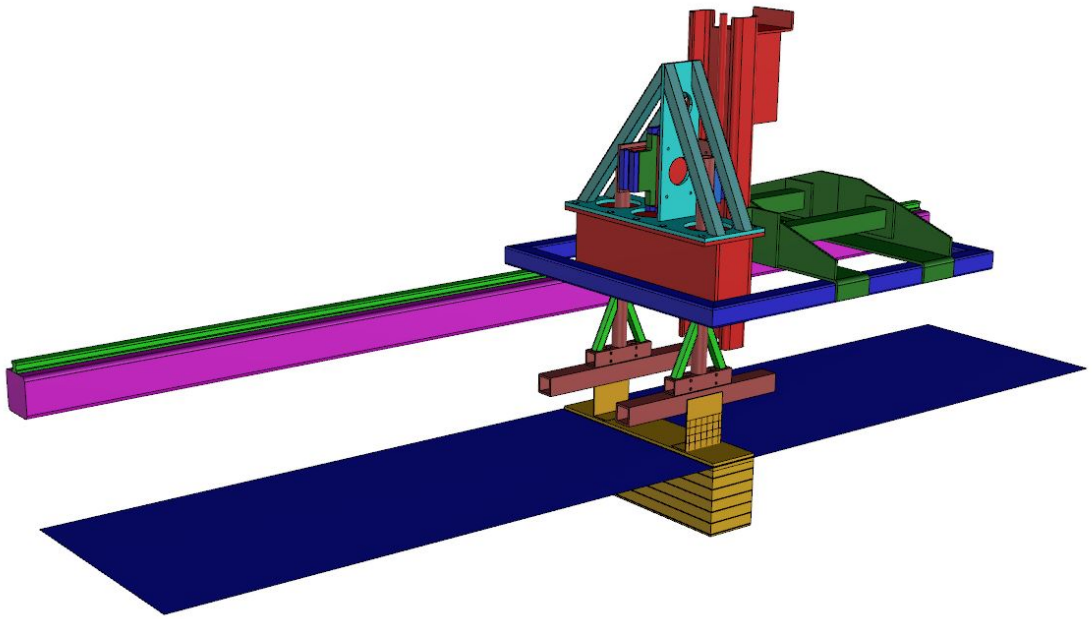

Figure 6.3: 3D model of test rig for the experiment made by Trond Innset.

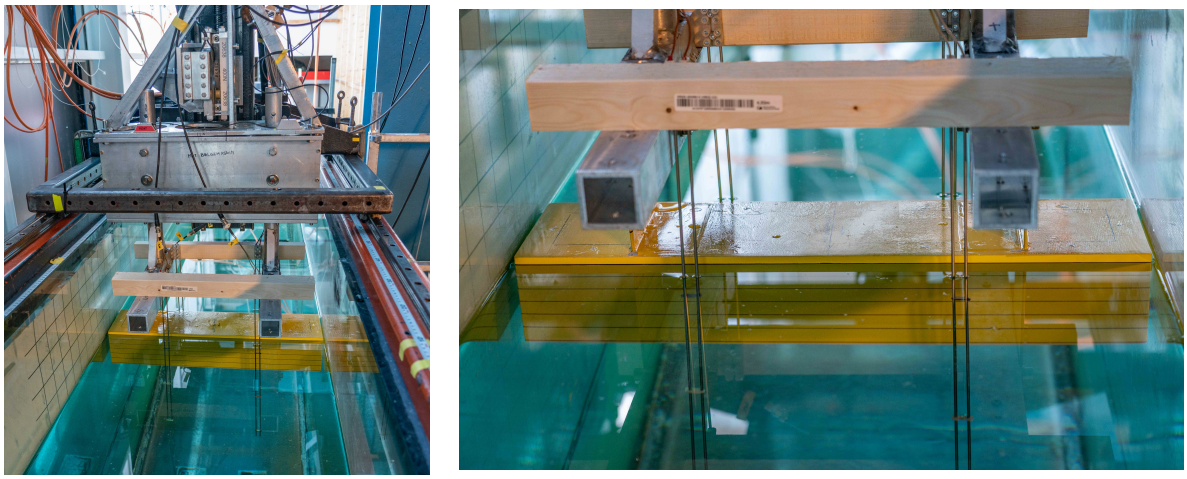

(a) (b)

Figure 6.4: Front view of the pontoon model and connection in Ladertanken.

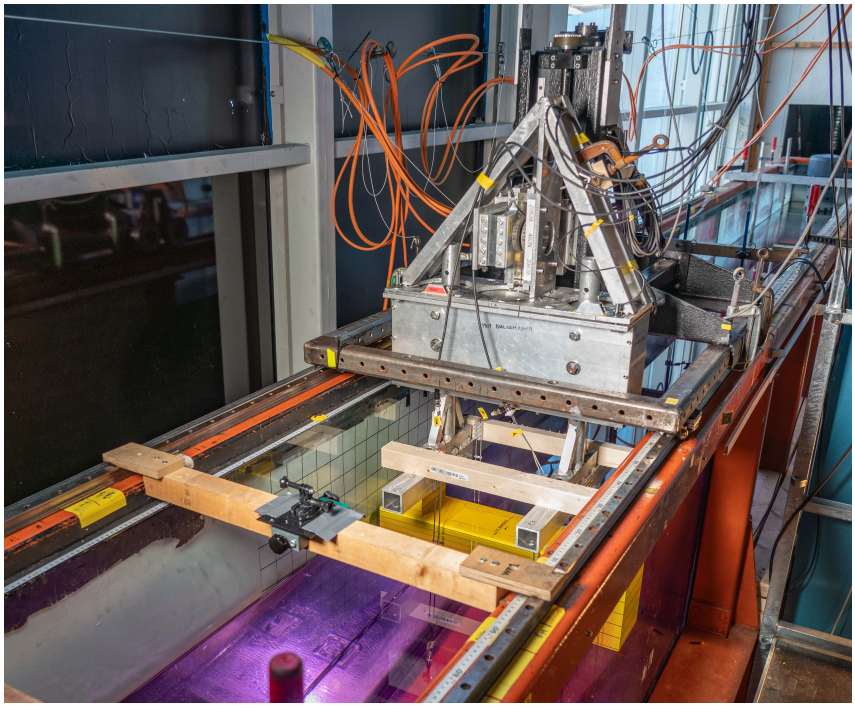

Figure 6.5: Perspective view of the pontoon model and connection rig in Ladertanken with colored water for better visualization of the waves and free surface.

6.1.3 Parabolic Beach

A parabolic beach was installed at the opposite end of the wave flume during tests with incident waves. For the tests with forced heave oscillations was another beach installed next to the wavemaker to damp out the waves generated by the oscillatory motions of the pontoon. The beaches damp out waves and reduce wave reflection by triggering wave breaking.

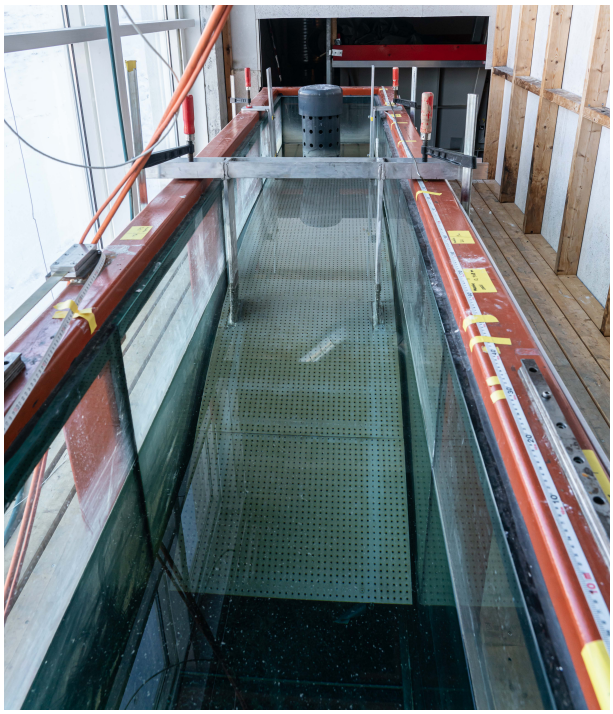

Figure 6.6: Parabolic beach installed on the opposite side of the wavemaker. The beach is made of a perforated plate which was about 0.5 cm below the free surface at the top point.

6.2 Fixed Model in Regular Waves

This section describes the setup of the incident waves test on the fixed pontoon. These tests aim to measure the horizontal and vertical forces on the pontoon, and the transmitted waves behind the model.

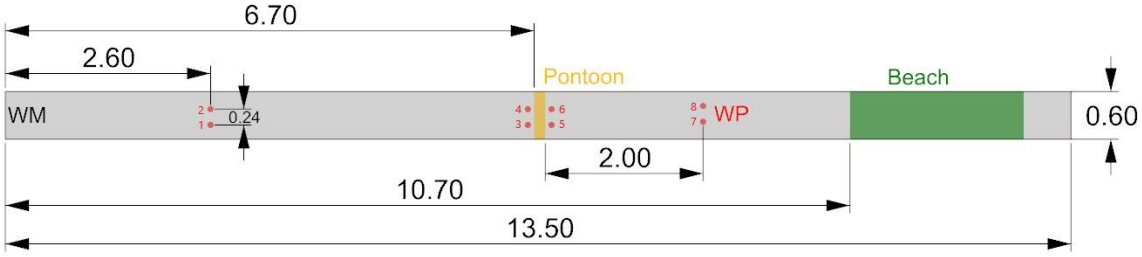

Figure 6.7: Ladertanken with the location of the pontoon model and wave probes during the tests with incident waves. The wave probes are marked with red circles. The distance between the pontoon model and the closest wave probes is 3.0 cm.

Ladertanken produces waves of high quality for periods of 0.6 s to 1.3 s. Therefore, waves with periods of 0.6 s to 1.3 s are used with a wave period increment of 0.01 s between each run. Numerous wave steepnesses, as listed in Table 6.2, are chosen to be tested to get a wide range of steepnesses to be able to compare the effect of steepness.

Table 6.2: Overview of incident waves as a function of wave periods to be tested. The last wave test with steepnesses of 1/60 to 1/30 was run with and without top extension on the pontoon model.

ϵ	T_{min} [s]	T_{max} [s]	ΔT [s]	H_{min} [m]	H_{max} [m]
1/100	0.60	1.30	0.01	0.006	0.026
1/60	0.60	1.30	0.01	0.009	0.043
1/45	0.60	1.30	0.01	0.012	0.058
1/30	0.60	1.30	0.01	0.019	0.087
1/25	0.60	1.30	0.01	0.022	0.104
1/20	0.60	1.20	0.01	0.028	0.112
1/60 - 1/30	0.60	1.30	0.35	0.009	0.087

Each run consisted of 3 ramp up periods in order gradually build up the wave height, thereafter 34 regular periods and lastly 3 ramp down periods.

Figure 6.8 shows the perspective view of a wave causing significant wave overtopping during the incident wave tests.

Figure 6.8: Perspective view of incident wave with significant wave overtopping of the pontoon.

6.3 Forced Oscillations in Heave

This section describes the setup of the forced heave tests. The aim is to determine the frequency- and motion amplitude-dependent added mass and damping coefficients, $A_{33}(\omega)$ and $B_{33}(\omega)$. Figure 6.9 shows the layout of the wave probes, pontoon model and beaches for the forced heave tests.

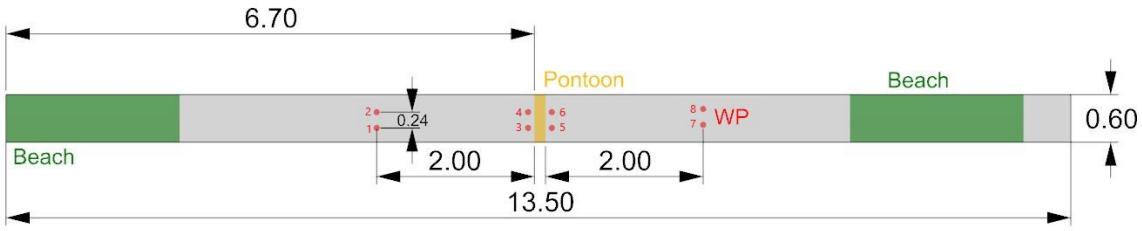

Figure 6.9: Ladertanken with the location of the pontoon model and wave probes. The wave probes are marked with red circles. The distance between the pontoon model and the closest wave probes is 3.0 cm.

The oscillation periods to be tested have been chosen to be equal to the incident wave periods, i.e. 0.6 s to 1.3 s. An oscillating period increment of 0.01 s between each test gives a total of 71 tests for each motion amplitude. In addition, tests with three oscillation periods were also run as a function of the motion amplitude, η_{3a}. All cases were run with and without the top extension.

Table 6.3: Forced oscillation periods and angular frequencies in heave tested. The change in oscillation period, ΔT, is chosen to be 0.01 s, which gives 71 oscillation periods to be tested per oscillation amplitude. All cases were performed with and without the top extension.

$T_{osc.}$ [s]	ΔT [s]	η_{3a} [cm]
0.6 - 1.3	0.01	0.5, 1.0, 2.0, 3.0
0.6 - 1.3	0.35	0.5, 0.51, 0.52, ..., 3.0

Due to the low freeboard of 9 mm will flooding of the pontoon deck occur for most of the heave amplitudes listed in Table 6.3. In order to study the forces with and without this effect will the tests be run with and without an extension wall prohibiting flooding. This doubles the required number of tests to 420. Each test will consist of 3 ramp-up, 34 regular and 3 ramp-down periods.

Figure 6.10 shows an example of the forced heave test without the top extension attached. The motion amplitude shown is 3.0 cm with an oscillation period of 0.6 s.

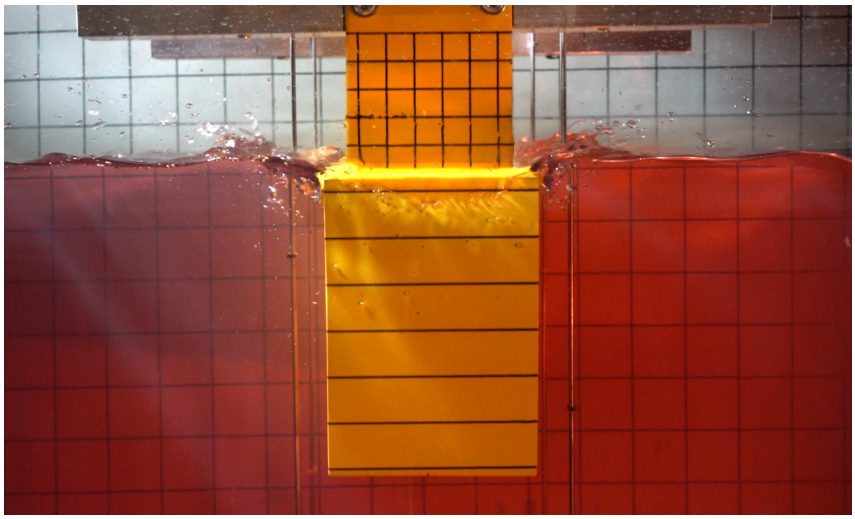

Figure 6.10: Side view of the pontoon without the top extension during forced heave tests with η_{3a}=3.0 cm and T=0.6 s. The pontoon is moving downwards at the shown moment.

6.4 Instrumentation

The sensors to be used during the experiment are listed below:

- Wave probes
- Force transducers
- Accelerometers
- Cable extension position sensors

In addition, a camera is used to capture slow-motion video up to 100 fps of a selection of wave cases to be tested and the forced heave test.

6.4.1 Wave Probes

A total of 8 wave probes were used. 2 in front, 2 behind and 4 fixed to the pontoon model. The wave probes were placed in parallel to provide redundancy if one failed. Having two sensors measuring the same values also provides additional confidence in the results. Figure 6.11 shows the arrangement used for the wave probes in front and behind the pontoon model, i.e. wave probes 1, 2, 7 and 8. The probes fixed to the pontoon model are shown in Figure 6.4b.

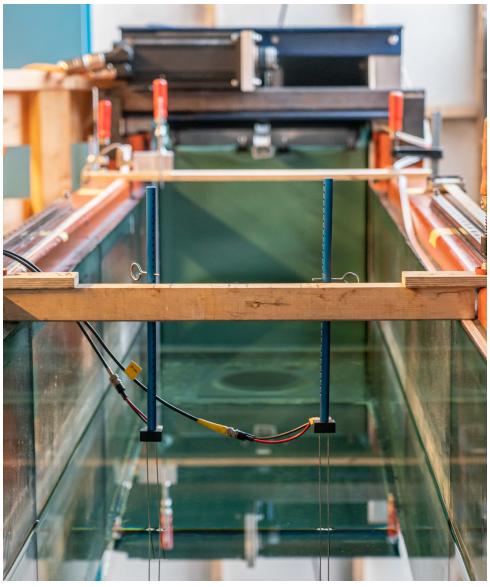

Figure 6.11: Wave probe 1 and 2. All wave probes were in parallel. Similar setup was used on wave probe 7 and 8.

A voltage is applied to two parallel rods. The current through the wave probe depends linearly on the depth of the probe, which is converted to an output voltage. The relation between the output voltage and surface elevation can be defined as shown in Equation 6.1, where E is the output voltage, ζ is the surface elevation, a the calibration factor and b the intersection point. The aim of the calibration is to determine the calibration factor, a.

$$\zeta(E) = aE + b \tag{6.1}$$

In order to calibrate the wave probes, the submergence of the rods is changed by a known distance while measuring the output voltage. The relation between voltage and submerged depth is plotted, as shown in Figure 6.12, and the calibration factor, a, is found by linear regression.

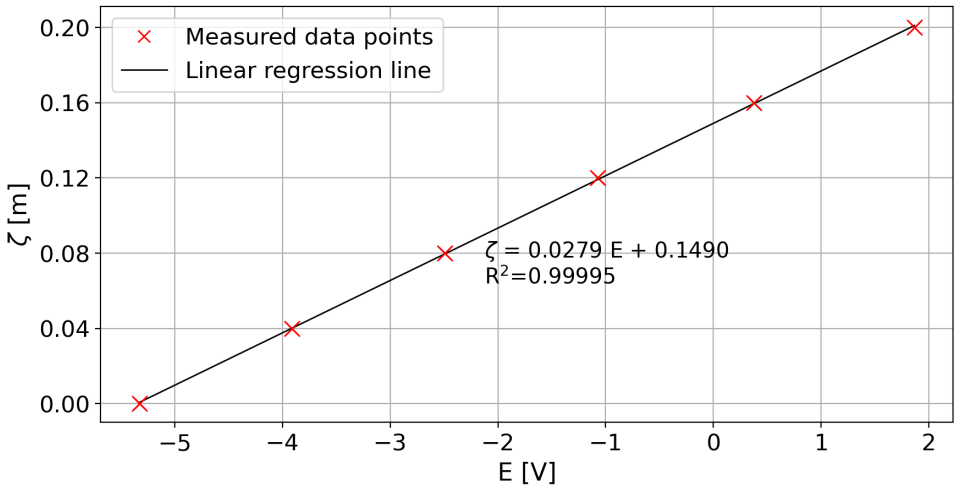

Figure 6.12: Wave calibration slope for wave probe 8. The R^2 value of 0.99995 means excellent linearity in the measurements. A similar level of linearity was also found for the other wave probes.

6.4.2 Force Transducer

Two shear force transducers connected 90°relative to each other, as shown in Figure 6.13b, were installed to measure vertical and horizontal forces on the pontoon model. The capacity of both force transducers was 400 N. The force transducers were mounted on top of a connection rig, as shown in Figure 6.13a.

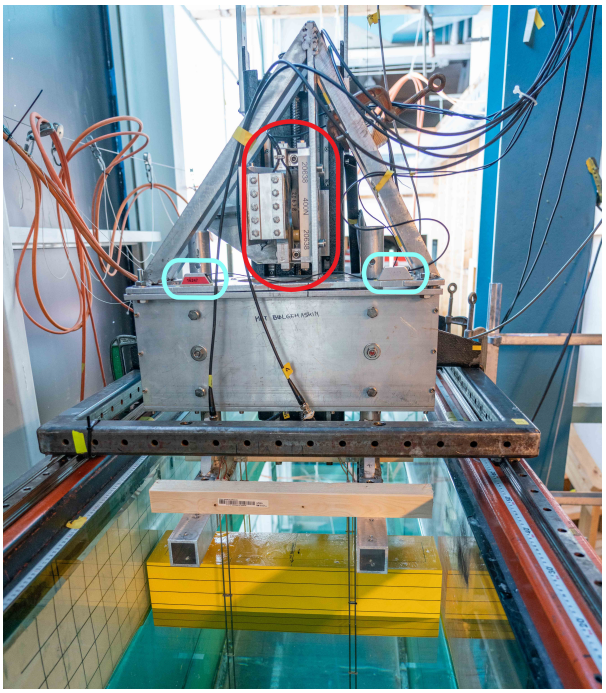

(a) Red circles shows the location of the force transducers and the cyan circles shows the accelerometers.

(b) Close up of the force transducers.

Figure 6.13: Force transducer measuring horizontal and vertical forces.

6.4.3 Accelerometer

Two accelerometers for measuring vertical acceleration were placed on top of the connection rig, as shown in Figure 6.13a. Figure 6.14 shows a close-up picture of the accelerometer on the

left-hand side. As for the wave probes, using two sensors ensures redundancy if one sensor fails and provides the opportunity to check the sensor data against each other.

The sensors did not need calibration. However, the values corresponded well to the theoretical values expected for oscillations with given amplitudes and frequencies.

Even though the accelerometers were not mounted directly on the pontoon model, the vertical stiffness of the connection rig is assumed to be so high that the difference is negligible.

The acceleration, together with the measured vertical force, was used for calculating added mass and damping.

Figure 6.14: Accelerometer installed on top of the rig.

6.4.4 Cable Extension Position Sensor

Cable extension position sensors were used to measure the vertical displacement of the pontoon model in forced heave, and horizontal displacement of the wave maker flap. The sensor was a WS10 cable extension position sensor made by ASM [24].

The calibration factor of such sensors are typically very stable and provide high accuracy. It was therefore expected to provide accurate measurement without further calibration. However, the sensor was checked against the displacement measured by the actuator rig, which corresponded very well.

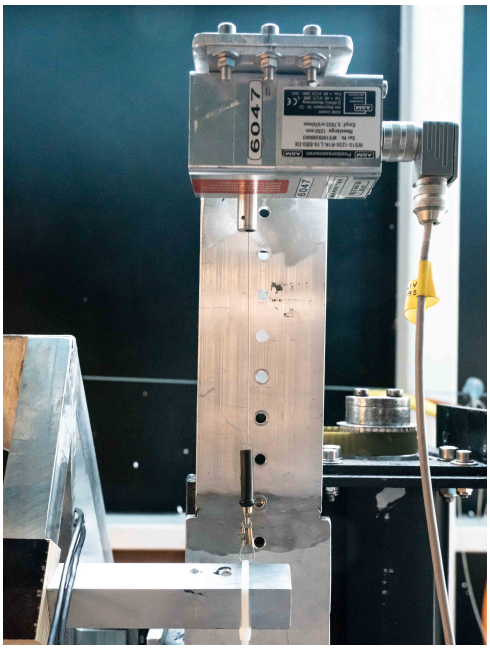

Figure 6.15: Cable extension position sensor for measuring the vertical position of the pontoon during forced heave oscillations. The same type of sensor was also used for measuring the position of the wave maker flap.

6.5 Wave Maker Calibration

The wave maker was calibrated prior to the incident wave tests. Periods and steepnesses planned for the experiments were run with no model present in the tank. Wave probes were placed at the location where the pontoon model would be located, i.e. 6.7 m from the wave maker. Thus making the wave maker calibrated for the exact pontoon model location.

Two transfer functions were established and combined into a total transfer function. The goal is for the wave maker to produce the specified waves at the location where the pontoon model is later placed.

The mechanical transfer function is correcting the theoretical flap amplitude defined in Equation 2.20. The wave maker flap amplitude is measured and compared to the specified amplitude, and the differences between those make the mechanical transfer function. This was an iterative process.

The hydrodynamic transfer function compares the wave amplitude measured by the wave probes with the specified wave amplitude. This was done after the mechanical transfer function was found. Then the difference between measured and specified wave amplitude is used to establish the hydrodynamic transfer function. This was an iterative process.

Finally, the mechanical and hydrodynamic transfer functions are multiplied together to the total transfer function, which is shown in Figure 6.16. The total transfer function depends on both wave steepness and period. Linear interpolation is used between steepnesses.

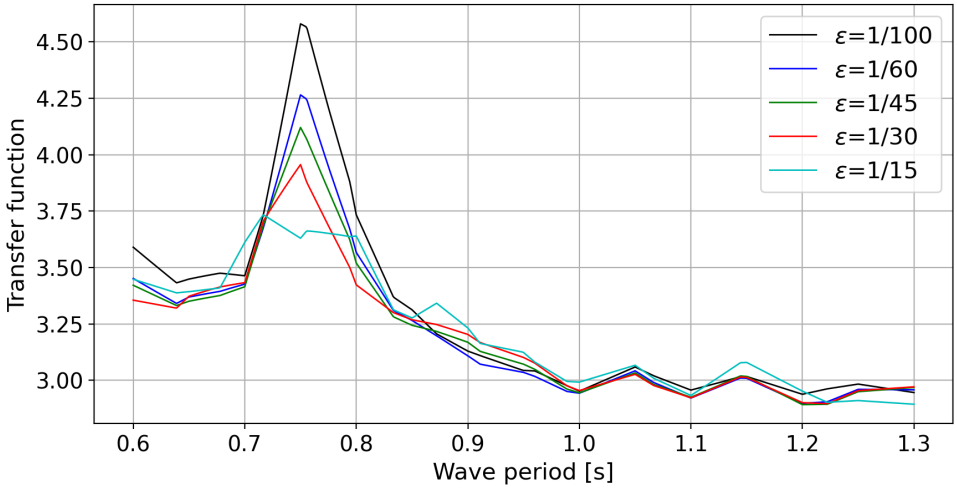

Figure 6.16: The total transfer function for the wave maker.

A test of the performance of the total transfer function was performed to check the accuracy. A wide range of steepnesses, from 1/100 to 1/15, was tested to see if the linear interpolation approach between steepnesses was appropriate. The measured wave amplitudes, together with a curve marking the specified wave amplitudes, are shown in Figure 6.17. The coloured areas mark the range ±5 % of the specified amplitude and follow the same colour code.

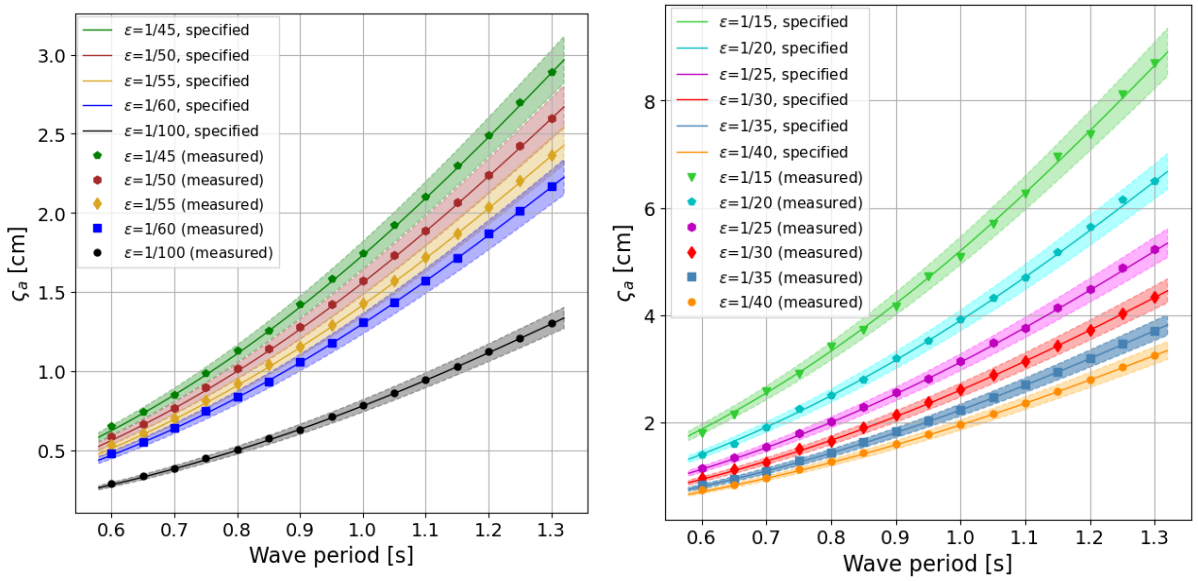

(a) Steepness 1/100 to 1/45.

(b) Steepness 1/40 to 1/15.

Figure 6.17: Measured and specified wave amplitude for different steepnesses. The colored areas ranges ± 5 % of the specified wave amplitude. All measured waves are within this interval.

The wave amplitude deviation from the specified values is shown in Figure 6.18 in both millimetres and per cent. All measured wave amplitudes are within ± 5 % and ± 3 mm, which is assumed to be acceptable.

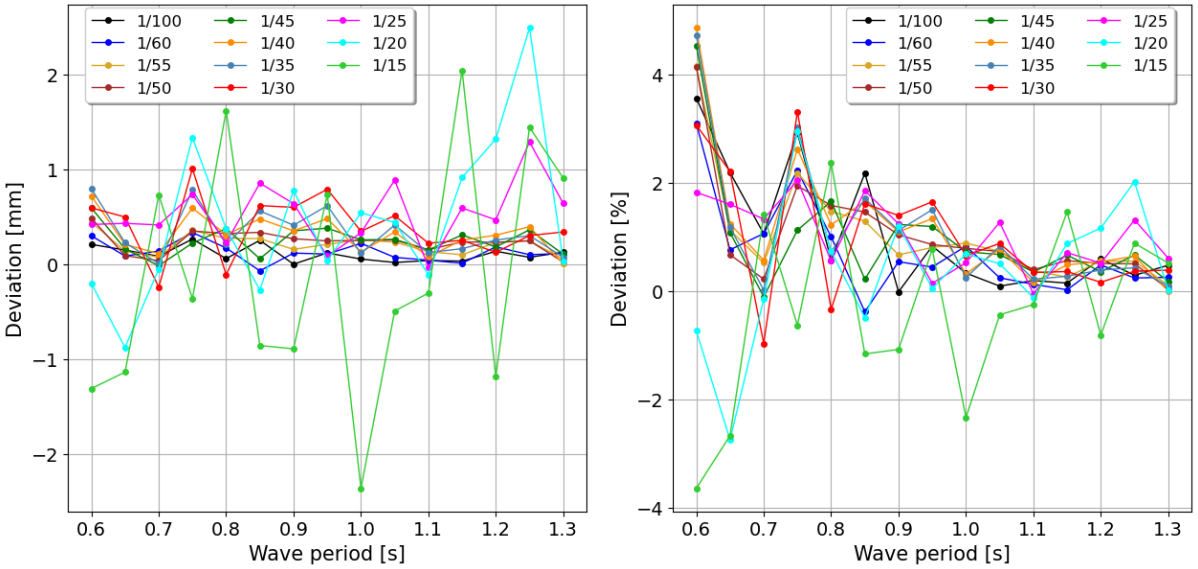

(a) Deviation in mm.

(b) Deviation in percent.

Figure 6.18: Accuracy of the wave maker with the total transfer function.

6.6 Post-Processing

6.6.1 Filtering

All sensors used were sampled at 200 Hz with a 20 Hz Butterworth filter. This filter is designed to give a frequency response as flat as possible. The filter is rejecting unwanted frequencies while affecting the wanted frequencies as little as possible [25].

6.6.2 Harmonic Forces

The harmonic force components from the experiments have been post-processed following the same procedure as for CFD, as described in section 5.7.

6.6.3 Added Mass and Damping

The vertical force transducer measures the total force during the forced heave oscillations, F_z. Then we subtract the restoring force and mass forces to obtain the hydrodynamic forces, F_h, acting on the pontoon model as defined in Equation 6.2.

$$F_h(t) = F_z(t) - M_{dry}\ddot{\eta}_3(t) - C_{33}\eta_3(t) \tag{6.2}$$

The hydrodynamic force comes from added mass and damping, which are 90° out of phase with each other. Then by assuming harmonically varying forces, velocity and accelerations, we can obtain the added mass and damping by applying Fourier averaging as shown in Equation 6.3 and 6.4.

$$A_{33} = \frac{\int_{nT} F_h \ddot{\eta}_3 dt}{\int_{nT} \ddot{\eta}_3 \ddot{\eta}_3 dt} \tag{6.3}$$

$$B_{33} = \frac{\int_{nT} F_h \dot{\eta}_3 \ dt}{\int_{nT} \dot{\eta}_3 \dot{\eta}_3 \ dt} \tag{6.4}$$

The linear damping from radiated waves is found with Equation 2.26. The wave amplitudes were measured with the wave probes 2.0 m from the pontoon. Before finding the wave amplitudes, a band-pass filter from 0.7 to 1.3 times the oscillation period was applied to the radiated wave time series.

6.6.4 Transmitted Waves

During incident wave tests, the transmitted waves were measured 2.0 m behind the pontoon model. The time series of the waves was filtered by a band-pass filter from 0.7 to 1.3 times the incident wave period.

6.7 Error Sources

The following section will discuss possible error sources connected with the experiment. In addition, the repetition tests also give an understanding of the precision of the tests.

6.7.1 Assuming 2D Flow

The incident waves and flow around the pontoon are assumed to have negligible variations across the breadth of the wave flume. Figure 6.19 shows how a wave with ϵ=1/45, T=1.30 and H=0.058 m flow over the pontoon deck. The image shows relatively small variations across the wave flume breadth. However, small wiggles on the free surface can be observed, which vary locally. In addition, the flow may have more 3D variations than the ones which can be observed visually. Especially close to the wave flume walls may the flow deviate from this assumption and thus affecting the pattern of the flow.

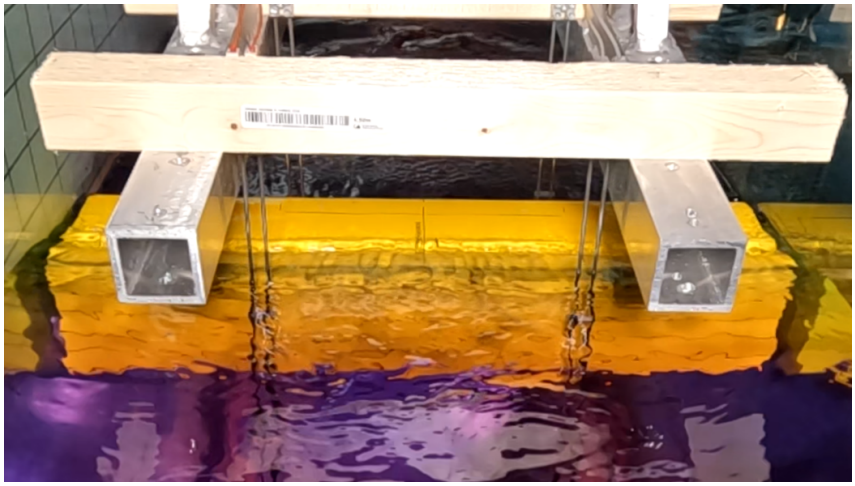

Figure 6.19: Top view of incident wave with significant wave overtopping of the pontoon. The wavefront flow over the pontoon deck with relatively low variation across the breadth. The wave has ϵ=1/45, T=1.30 s and H=0.058 m.

6.7.2 Water Depth

The water level in the wave flume was controlled before each test and adjusted when needed. The water level was controlled visually against a mark at the plexiglass wall. The precision of the water level is assumed to be around ± 1 mm. Over time, the amount of water in the flume would decrease due to vaporization and leakage. For long tests, this effect might affect the water level. Most of the tests took around 13 h. However, the repetition test for incident waves lasted for 22 hours. The wave probes measured 0.6 mm lower water level at the end of the 22 h test.

6.7.3 Initial Disturbance of the Free Surface

It is essential that the free surface is completely undisturbed at the beginning of each test. However, since the experiment is performed in a closed tank, the waves will reflect when hitting the walls in addition to the pontoon. The pause between each test was chosen to ensure enough time for the free surface to settle down completely. This was controlled visually. On the other hand, the pause makes up most of the time spent during the experiments, so too long pauses will decrease the number of tests. The parabolic beach reduces the reflections at the end significantly.

6.7.4 Wave Reflection

The waves will reflect when hitting the pontoon model and walls during the tests. This may influence the wave train and the forces on the pontoon model. Therefore, the steady-state interval has been chosen to end before the reflected waves reach the pontoon model.

6.7.5 Incident Wave Height and Steepness

Based on the results from the wave calibration, which showed good agreement between the specified and measured wave height, has the wavemaker been trusted to produce the accurate waves. Therefore, the specified wave height has been used to normalize the results during post-processing. The wave calibration showed that most wave heights deviate with less than 2 %, while some deviate up to around 4 %. However, this precision was tested prior to the experiment with the pontoon model. It is possible that the precision limit drifted during the 3 weeks of testing, and can therefore be a source of error.

6.7.6 Weight of Connection Rig

The pontoon model was weighed to be 15.2 kg without the top extension. The force transducers were connected to the connection rig, which again was connected to the pontoon model. This means that forces from accelerating the weight of the connection rig would be part of the force measured by the force transducer. Heave oscillations were performed without water in the tank to estimate the total weight of the pontoon model and connection rig. The same approach for finding added mass, as described in section 6.6.3, was used to find the dry mass of the setup. Due to the absence of buoyancy was the vertical transducer close to its capacity of 400 N from holding the static weight of the setup. This affected the oscillation amplitude and frequency, which could be run without exceeding the limit of the transducer. Oscillation amplitude of 1.0 cm and frequency of 0.7 Hz and 1.0 Hz resulted in average weight of the connection rig of 19.5 kg with a standard deviation of 0.7 kg. Ideally, more tests and higher amplitudes and frequencies should be performed to get an estimate with higher precision. This was, however, not possible due to the capacity of the force transducer.

6.8 Experimental Precision

Twelve test cases were repeated ten times for both the incident waves and forced heave to estimate the experimental precision. The experimental precision is presented as scatter plots with the results from all 10 repetitions in addition to a figure showing the coefficient of variance.

6.8.1 Incident Waves

Four steepnesses of 1/100, 1/60, 1/45 and 1/30 were tested with periods of 0.60 s, 0.95 s and 1.30 s. Both the steepnesses and periods were chosen to cover the whole range of waves used in the experiments.

The horizontal wave-induced forces are shown in Figure 6.20, while the coefficient of variance is presented in Figure 6.21. The first harmonic forces show little variations with a coefficient of variance below 0.3 % for all cases. The second and third harmonics show more considerable variations, especially for the steepness of 1/100.

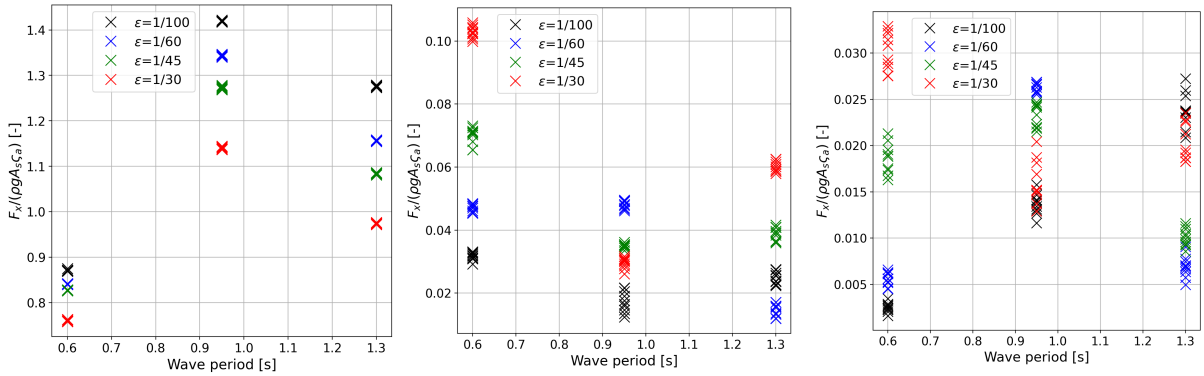

(a) 1st harmonic **(b)** 2nd harmonic **(c)** 3rd harmonic

Figure 6.20: Repetition test of horizontal force with 10 repetitions of each case.

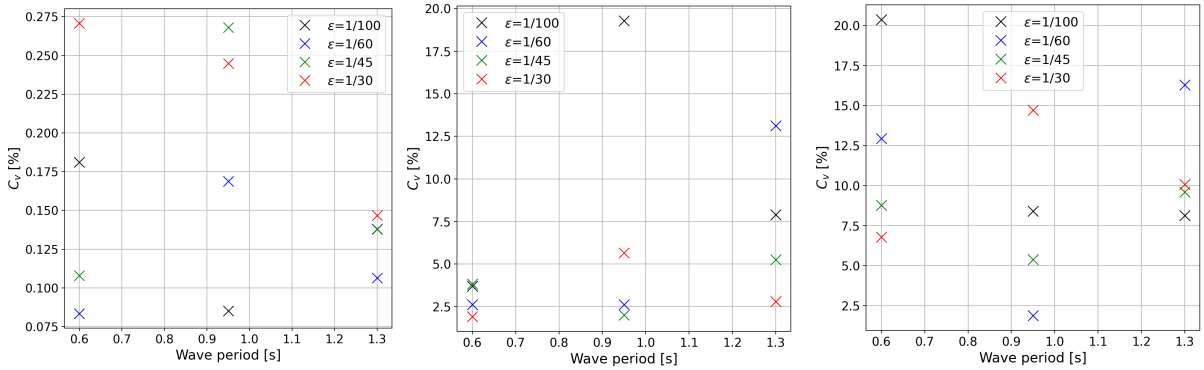

(a) 1st harmonic **(b)** 2nd harmonic **(c)** 3rd harmonic

Figure 6.21: Coefficient of variance for the horizontal forces.

The vertical wave-induced forces are shown in Figure 6.22, while the coefficient of variance is presented in Figure 6.23. The first-order harmonic has a higher coefficient of variance than the horizontal forces, but is still within an acceptable limit. On the other hand, the second-order harmonics are lower than for horizontal forces.

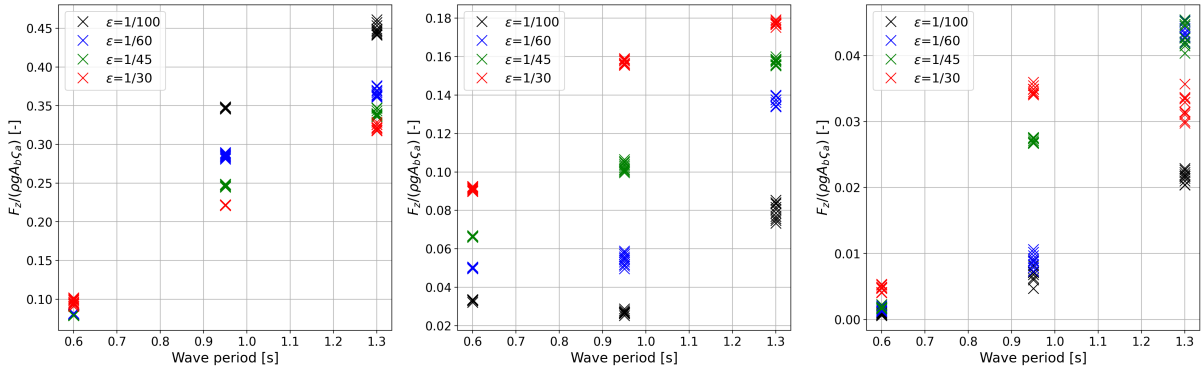

(a) 1st harmonic **(b)** 2nd harmonic **(c)** 3rd harmonic

Figure 6.22: Repetition test of vertical force with 10 repetitions of each case.

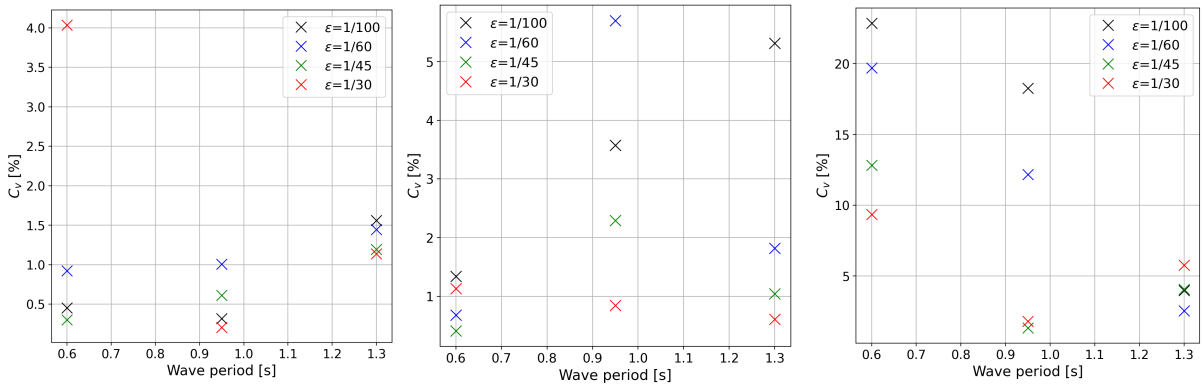

(a) 1st harmonic **(b)** 2nd harmonic **(c)** 3rd harmonic

Figure 6.23: Coefficient of variance for the vertical forces.

6.8.2 Forced Heave

Four heave amplitudes of 0.5 cm, 1.0 cm, 2.0 cm and 3.0 cm were tested with three periods of 0.60 s, 0.95 s and 1.30 s. All cases have been run both with and without the top extension. As for the repetition tests for the incident waves do the motion amplitudes and periods cover the range of forced heave cases performed during the experiment.

Figure 6.24 shows the results from the forced heave repetition test, which indicates good repeatability. The coefficients of variance are presented in Figure 6.25 and show that the added mass and damping have coefficients of variance below 1.0 % and 2.2 %, respectively.

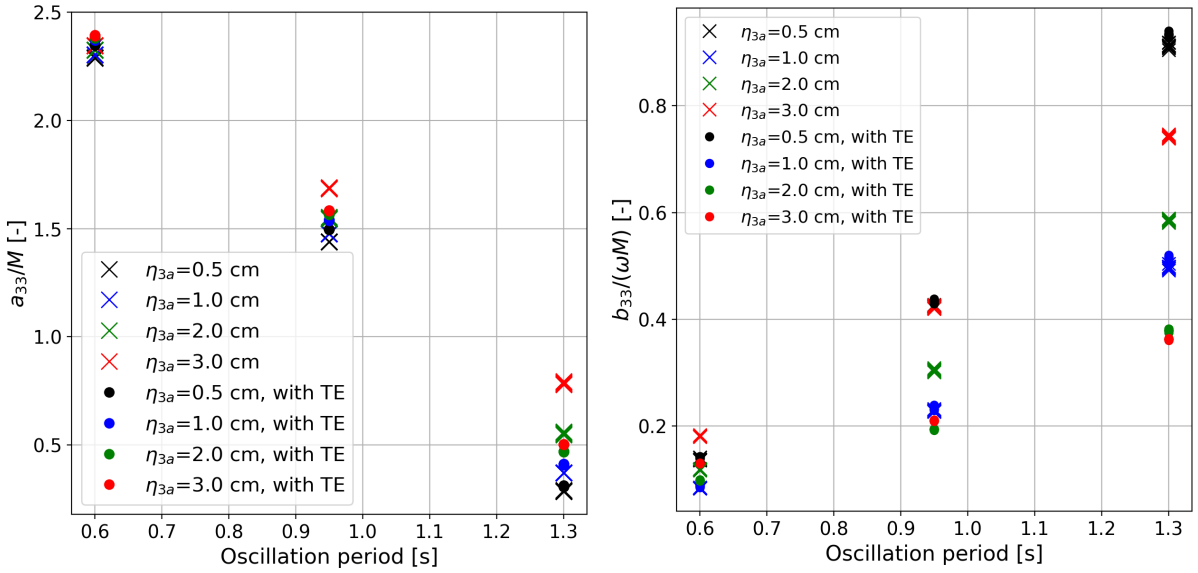

(a) a_{33} **(b)** b_{33}

Figure 6.24: Repetition test of added mass and damping with 10 repetitions of each case.

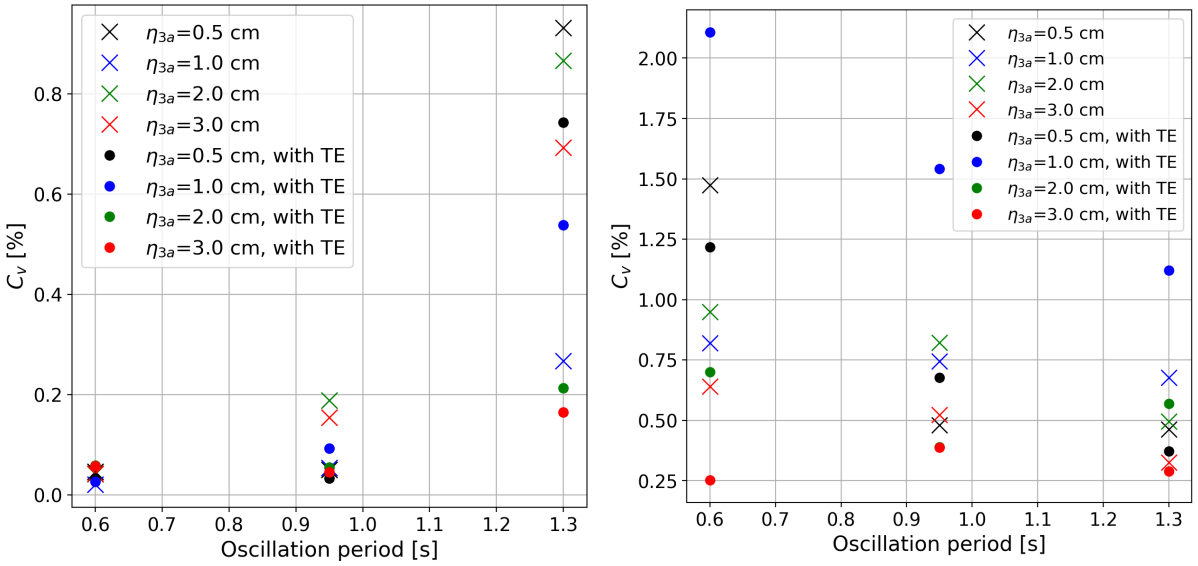

(a) a_{33} **(b)** b_{33}

Figure 6.25: Coefficient of variance for added mass and damping.

Chapter 7

Time-Domain Simulator

This chapter describes the simulator used for simulating the motions, including non-linear effects from the experiments. The non-linearity is included as correction factors for excitation, added mass and damping. The factors depend on the incident wave period or oscillation period and motion amplitude. In addition, the simulator changes the hydrostatic stiffness when the structure is submerged below the freeboard due to a significant difference in the water plane area.

The motions of interest are surge, heave and pitch since the structure is symmetrical and we only look at regular head waves. Heave motions are uncoupled and can be analysed separately from surge and pitch. On the other hand, surge and pitch are coupled motions that influence one another.

7.1 Methodology for Building the Simulator

The simulator solves the equation of motion using the fourth-order Runge-Kutta method described in section 2.5. The solver needs added mass, damping and restoring coefficients, in addition to excitation forces and the mass properties of the structure, to solve for the motions. It also assumes the structure to initially be at rest, with position, velocity and acceleration set to zero. The linear solution from WAMIT assumes added mass and damping coefficients only vary with the incident wave frequency, ω, while the restoring is constant. Then the motion amplitude can be solved efficiently in the frequency domain. However, the frequency domain is not suitable for adding non-linear effects.

The first step was then to get the time domain simulator to solve for the motions using the linear coefficients from WAMIT. The solution should then be identical to the one from the frequency domain and is a way of checking that the simulator solves the problem correctly before adding non-linear effects.

When the simulator calculates the linear motions correctly, non-linear factors will be added. Strip theory is used for integrating the pressures from WAMIT combined with local correction factors accounting for local wave height and heave motion relative to the freeboard.

7.2 Numerical Challenge for Surge and Pitch Motion

The surge and pitch motions, for unknown reasons, explode for specific incident wave periods in the simulator. Figure 7.1 and 7.2 shows the surge and pitch RAO, respectively, with the results from the simulator against the WAMIT RAO. The periods in which the simulator fails to calculate the motions are marked with red dots. However, the motions are simulated quite accurately for periods that do not cause exploding motions. The only exception is for T=6.40

s and 6.45 s, which deviates noticeably from the WAMIT solution. They are next to a set of periods the simulator fails to simulate, so the same effects causing them to fail likely make the results for T=6.40 s and T=6.45 s inaccurate.

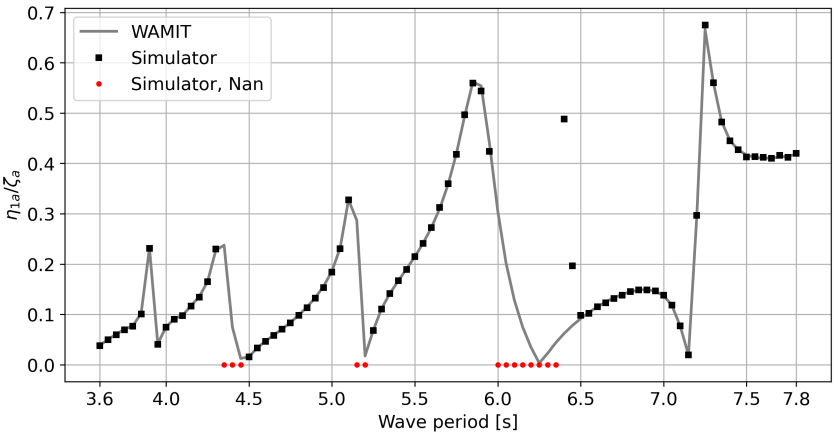

Figure 7.1: Surge RAO from WAMIT and time domain simulator with linear coefficients.

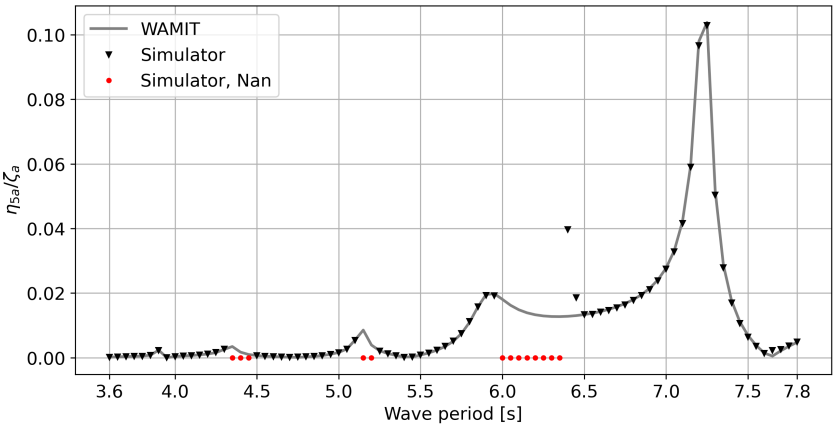

Figure 7.2: Pitch RAO from WAMIT and time domain simulator with linear coefficients.

A significant amount of time, in the order of well over a month, has been used trying to solve this problem without success. The excitation forces and added mass, damping and restoring coefficients imported from WAMIT have been plotted against each other and verified to be correct. Furthermore, since the results that do not explode match well with the WAMIT RAO, is it good reason to believe that the simulator calculates the motions correctly.

A fictive mass was added to both sides of the equation of motion to stabilize the solver. The motions increased continuously without oscillations before this measure was tried. The fictive mass helped to get oscillating motions, but the amplitudes quickly increased to infinity. Nevertheless, to get the motions to at least oscillate was a step in the right direction.

Many other measures have been tried without luck. One is decreasing the time step significantly, down to 0.0001 s. Increased damping and added mass in the transient phase have also been tried to control the motions initially. None of the measures improved the result.

The main hypothesis for the exploding motions is connected to the added mass. The added mass in surge, A_{11}, is negative for the same periods on which the simulator fails. The added mass plots can be found in section A.2. Moreover, the motions do not explode when all added mass values are set to zero. This will not give the correct motions, but it shows that the motions do not explode when changing the added mass values. This may indicate that the added mass values cause the numerical problem. However, this is just a hypothesis.

7.2.1 Coupled Equation of Motion for Surge and Pitch

The method and equations for solving the surge and pitch motions will in this section be briefly described, even though they caused problems for some wave periods. In that way, the reader can detect a potential error or reach another explanation for the challenges.

The coupled equation of motion for surge and pitch can be written as follows:

$$\begin{bmatrix} M_{11} & M_{15} \\ M_{51} & M_{55} \end{bmatrix} \begin{bmatrix} \ddot{\eta_1} \\ \ddot{\eta_5} \end{bmatrix} + \begin{bmatrix} B_{11} & B_{15} \\ B_{51} & B_{55} \end{bmatrix} \begin{bmatrix} \dot{\eta_1} \\ \dot{\eta_5} \end{bmatrix} + \begin{bmatrix} 0 & C_{15} \\ 0 & C_{55} \end{bmatrix} \begin{bmatrix} \eta_1 \\ \eta_5 \end{bmatrix} = \begin{bmatrix} F_1 \\ F_5 \end{bmatrix} \tag{7.1}$$

Where:

$$\begin{aligned} M_{11} &= M + A_{11} \\ M_{15} &= Mz_g + A_{15} \\ M_{51} &= Mz_g + A_{51} \\ M_{55} &= I_{55} + A_{55} \end{aligned} \tag{7.2}$$

The problem can be rewritten to a system of first-order differential equations using two auxiliary functions: $u = \dot{\eta}_1$ and $v = \dot{\eta}_5$. The system of equations for the coupled motions of surge and pitch are shown in Equation 7.3. A fictive mass, $M_{ij,f}$, is added to both sides of the equation to try to stabilize it, as mentioned above.

$$\begin{bmatrix} 1 & 0 & 0 & 0 \\ 0 & 1 & 0 & 0 \\ B_{11} & B_{15} & M_{11} + M_{11,f} & M_{15} + M_{15,f} \\ B_{51} & B_{55} & M_{51} + M_{51,f} & M_{55} + M_{55,f} \end{bmatrix} \begin{bmatrix} \dot{\eta_1} \\ \dot{\eta_5} \\ \dot{u} \\ \dot{v} \end{bmatrix} = \begin{bmatrix} u \\ v \\ F_1 + M_{11,f}\ddot{\eta_1} + M_{15,f}\ddot{\eta_5} - C_{11}\eta_1 \\ F_5 + M_{55,f}\ddot{\eta_5} + M_{51,f}\ddot{\eta_1} - C_{55}\eta_1 \end{bmatrix} \tag{7.3}$$

The fourth-order Runge-Kutta method is used to solve for the motions, where the surge and pitch positions are obtained from $\dot{\eta}_1$ and $\dot{\eta}_5$, respectively.

7.3 Heave

7.3.1 Equation of Motion

This section describes the equation of motion for heave used in the simulator. Heave is not coupled with any other motions, unlike surge and pitch, and can therefore be solved independently. The heave equation of motion can be written as:

$$[M + A_{33}(\omega)]\ddot{\eta_3}(t) + B_{33}(\omega)\dot{\eta_3}(t) + C_{33}\eta_3(t) = F_3(t) \tag{7.4}$$

This is a second-order differential equation and will be solved by the fourth-order Runge-Kutta method, which is described in section 2.5. Then the problem has to be rewritten as a system of first-order differential equations.

The acceleration is calculated as shown in Equation 7.5:

$$\ddot{\eta}_3(t) = \frac{F_3(t) - B_{33}\eta_3(t) - \dot{C}_{33}\eta_3(t)}{M + A_{33}} \tag{7.5}$$

Then the heave velocity and position is found by:

$$\dot{\eta}_3(t) = \ddot{\eta}_3(t) \cdot dt \tag{7.6}$$

$$\eta_3(t) = \dot{\eta}_3(t) \cdot dt \tag{7.7}$$

Each simulations begin with a five ramp-up periods to gradually build up the excitation forces and motions. The total simulation length was set to conservative value of 1000 s, ensuring all cases reaching steady state. The steady-state interval was chosen to be from 900 s to 1000 s. Figure 7.3 shows an example of a time series of the heave motion with a wave steepness of 1/60. Correction set 1 was used for this example. It can be observed that the motion reach a steady state after approximately 300 s. A time series of the heave motion for a wave with T=4.0 s and ϵ=1/60 can be found in Appendix G, which shows that the motions reaches a steady state at later instance than what is the case in Figure 7.3.

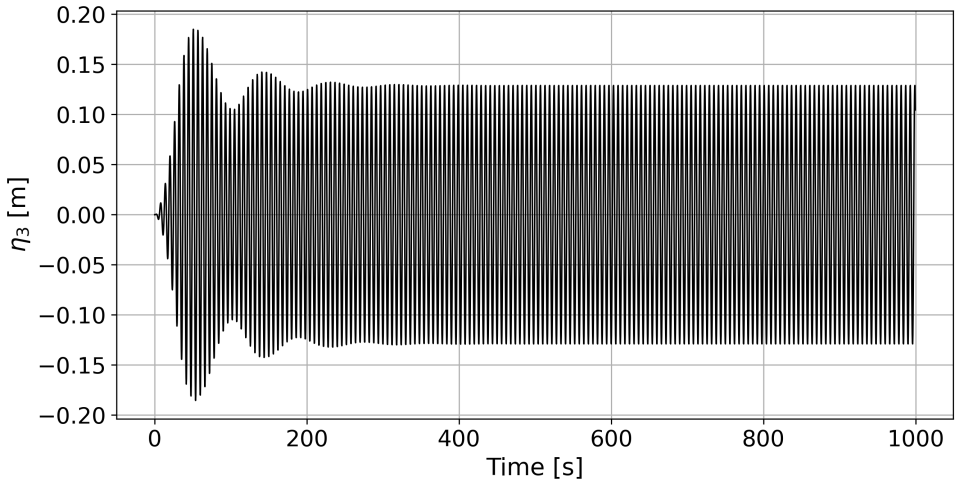

Figure 7.3: Heave motion time series for a wave with ϵ=1/60, T=6.0 s and H=0.94 m, and correction set 1.

7.3.2 Linear Motions

Figure 7.4 shows the motions from the simulator without any non-linear corrections, i.e. with unchanged values from WAMIT, plotted against the WAMIT RAO. Since the values for excitation, added mass, damping and restoring are the same, the result should also match each other. Two different wave steepnesses have been simulated to check that the linear result is independent of wave steepness. The motions for both steepnesses match the WAMIT RAO well and indicate that the heave motions are calculated correctly.

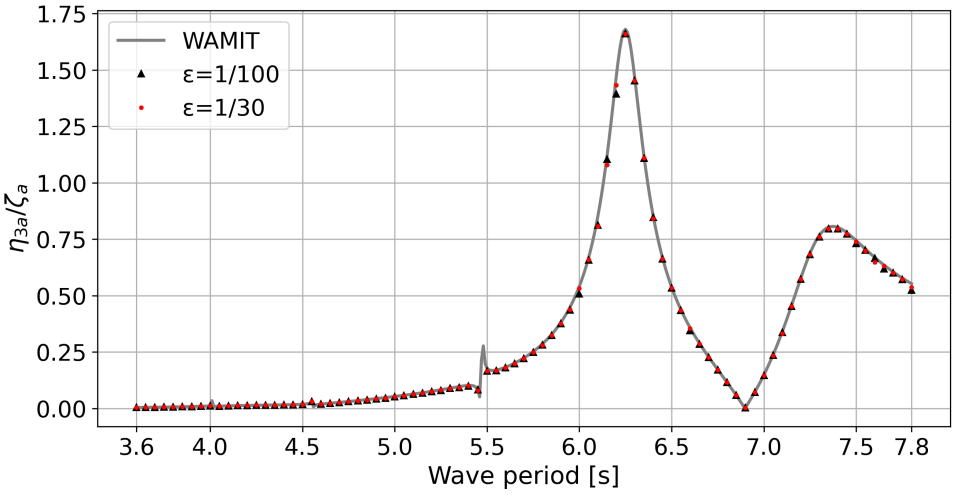

Figure 7.4: Time-domain simulation with wave steepness of 1/100 and 1/30 with no non-linear corrections. The results match WAMIT almost identically, which indicates that the simulator solves the equation of motion for heave correctly.

7.4 Diffraction and Radiation Pressure from WAMIT

WAMIT can calculate the complex pressure from the diffraction and radiation problem. The output is seven different pressure values for each panel, one diffraction pressure, p_D, and six radiation pressures, one for each of the rigid body modes, p_j, where j denotes the mode. The pressures from WAMIT are normalized as follows [18]:

$$\bar{p}_D = \frac{p_D}{\rho g \zeta_a} \tag{7.8}$$

$$\bar{p}_j = \frac{p_j}{\rho g \eta_j} \tag{7.9}$$

Excitation forces can be calculated by integrating the diffraction pressure over the body, while added mass and damping are found by integrating the radiation pressure. The real part of the complex radiation pressure gives added mass, and the imaginary part gives damping. For heave are F_3, A_{33} and B_{33} found with the following equations:

$$F_3(t) = \sum_{k=1}^{n_{pan}} \Re\{p_{D,k} e^{i\omega t}\} A_i n_{z,k} \zeta_a \alpha_E(x,t) \tag{7.10}$$

$$A_{33}(t) = \sum_{k=1}^{n_{pan}} \Re\{p_{3,k}\} A_i n_{z,k} \alpha_A(x,t) \tag{7.11}$$

$$B_{33}(t) = \sum_{k=1}^{n_{pan}} \Im\{p_{3,k}\} A_i n_{z,k} \alpha_B(x,t) \tag{7.12}$$

Where p_D and p_j is the complex diffraction and radiation pressure from the j^{th} mode, respectively. A_k is the panel area and $n_{z,k}$ the vertical component of the normal vector. n_{pan} is the number of panels.

The non-linear correction factors, α_E, α_A and α_B, are applied to each panel pressure. They depend on the largest value of x_E and x_{AB} measured during the previous wave period. The correction factors are therefore updated once every wave period.

7.5 Non-linear Correction Factors

Effects from wave overtopping and deck flooding are not included in WAMIT. The simulator aims to model these effects by applying correction factors found from experiments and CFD. Vertical forces, added mass and damping on the pontoon model with and without top extension (TE) are compared. No overtopping or flooding occurred during the tests with the top extension and are assumed to correspond to the WAMIT values. Then the correction factors are found as follows:

$$\alpha_F = \frac{F_{\text{no TE}}}{F_{\text{TE}}} \tag{7.13}$$

$$\alpha_A = \frac{A_{\text{no TE}}}{B_{\text{TE}}} \tag{7.14}$$

$$\alpha_B = \frac{B_{\text{no TE}}}{B_{\text{TE}}} \tag{7.15}$$

7.5.1 Restoring

The restoring coefficient is drastically reduced when OFM2 is submerged below the freeboard. Then only the 12 legs contribute to the water plane area, which is significantly lower than the pontoons area. The non-linear restoring force can be formulated as shown below in Equation 7.16.

$$C_{33}\eta_3 = \begin{cases} \rho g A_p \eta_3 & \text{for } \eta_3 > \text{-0.3 m} \\ \rho g((A_p \cdot (-f_p)) - 12A_l(\eta_3 + f_p)) & \text{for } \eta_3 < \text{-0.3 m} \end{cases} \tag{7.16}$$

Where A_p=1863 m^2 is the pontoon area, and A_l=12.5 m^2 is the cross-section area of one leg. The radius of each leg is assumed to be 2.0 m.

7.5.2 Excitation Correction Factors

The incident wave tests for three wave periods and steepnesses between 1/60 and 1/30 were performed with and without the top extension. The results are shown in Figure 8.12a and the factors according to Equation 7.13 are shown in Figure 7.5a. Further, to get the factors related to a more usable x-axis, they were plotted against the incident wave amplitude, ζ_a, divided on the freeboard, f_p, as shown in Figure 7.5b.

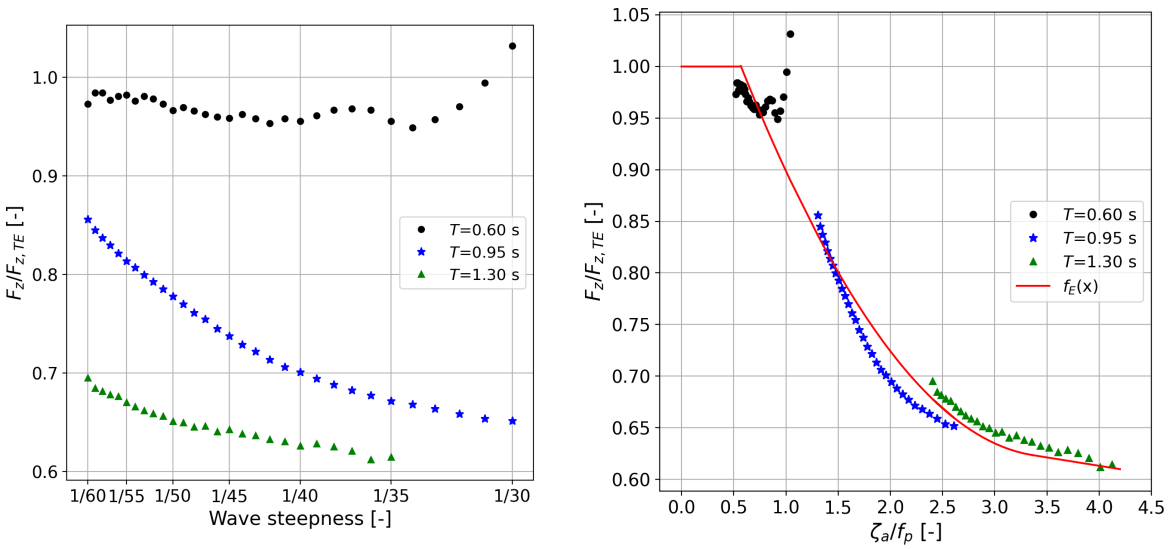

(a) **(b)**

Figure 7.5: 1st order vertical force without top extension relative to with top extension.

Then a polynomial curve fitting was used to find a suitable expression for the excitation factors. The fitted curve are shown in Figure 7.5b and the function is given below:

$$f_E(x_E) = \begin{cases} 1 & \text{for } 0.00 \leq x_E \leq 0.57 \\ 0.04x_E^2 - 0.30x_E + 1.16 & \text{for } 0.57 < x_E \leq 3.30 \\ -0.01x_E + 0.67 & \text{for } 3.30 < x_E \leq 4.20 \\ 0.63 & \text{for } 4.20 < x_E \end{cases} \tag{7.17}$$

Ideally, tests with more wave periods with the top extension attached should be performed. However, this was discovered after the experiment was completed. On the other hand, the result shows a consistent trend of decreasing vertical excitation forces when the incident wave increases.

The non-linear excitation factor depend on the local wave elevation, $\zeta(x,t)$, relative to the elevation of the pontoon deck above the mean free surface, $f_p + \eta_3(t)$. The largest value of x_E during a whole wave period is used to compute the non-linear correction factor for each panel.

$$x_E = \frac{\zeta(x,t)}{f_p + \eta_3(t)} \tag{7.18}$$

7.5.3 Added Mass and Damping Correction Factors

Forced heave tests were run with both oscillation period and amplitude as the main variable. The purpose of having two sets of correction factors is to compare the results to see how they match each other. This can provide a better understanding of the quality and validity of the correction sets. Furthermore, increased confidence in the results can be gained if they provide matching results.

First, oscillation amplitudes of 0.5 cm, 1.0 cm, 2.0 cm and 3.0 cm were run with oscillation periods ranging from 0.60 s to 1.3 s with 0.01 s increment with and without the top extension. This gives the first set of correction factors for added mass and damping. Thereafter, three oscillation periods, 0.60 s, 0.95 s and 1.30 s, were run with oscillation amplitudes ranging from 0.5 cm to 3.0 cm with 0.1 cm increment. This gives the second set of added mass and damping factors.

Since the factors are calculated from the experiments, all periods are given in model-scale. However, the time-domain simulator is in full-scale. Thus the periods are scaled by a factor of 6.0 due to Froude scaling. The Froude scaling is described in section 2.8.

The non-linear correction factors for added mass and damping depends on the incident wave period and the amount of wave overtopping and pontoon deck flooding, which is calculated by Equation 7.19. The variable x_{AB} computes the vertical position of each panel relative to the undisturbed wave and is normalized with respect to the freeboard. The largest value of x_{AB} during a whole wave period is used as input for the local non-linear correction factor. The correction factors are therefore updated once every wave period.

$$x_{AB} = \frac{\eta(t) - \zeta(x,t)}{f_p} \tag{7.19}$$

Correction Set 1

The first correction set for added mass and damping is based on tests with four heave amplitudes run as a function of the oscillation period. The factors, plotted in Figure 7.6, is calculated from the results which can be found in Figure 8.15.

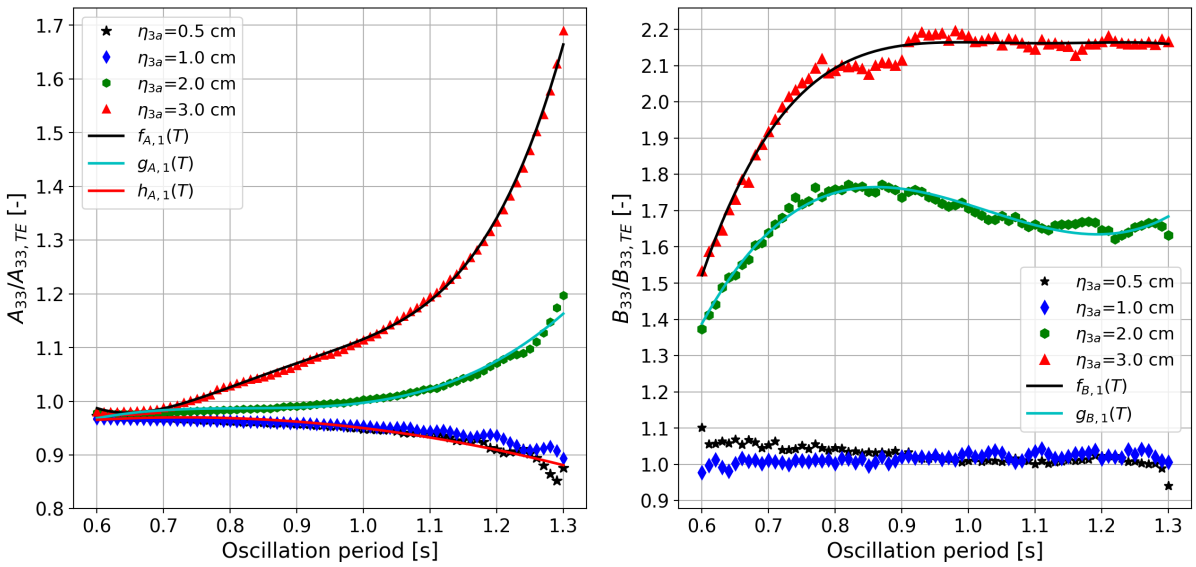

(a) Added mass. **(b)** Damping.

Figure 7.6: Added mass and damping without top extension (TE) relative to with top extension (TE) as a function of oscillation period.

Trend lines for the factors were found by poly-fitting, and the functions are shown below. For added mass is $h_A(T)$ representing the trend for both oscillation amplitude of 0.5 cm and 1.0 cm. Moreover, the damping factors are set to 1.0 for the same amplitudes.

$$f_{A,1}(T) = 12.65T^4 - 43.77T^3 + 56.59T^2 - 31.96T + 7.61 \tag{7.20}$$

$$g_{A,1}(T) = 1.57T^3 - 3.88T^2 + 3.19T + 0.11 \tag{7.21}$$

$$h_{A,1}(T) = -0.17T^2 + 0.40T + 0.82 \tag{7.22}$$

$$f_{B,1}(T) = -10.55T^4 + 46.94T^3 - 77.97T^2 + 57.32T - 13.57 \tag{7.23}$$

$$g_{B,1}(T) = 7.19T^3 - 22.18T^2 + 22.21T - 5.51 \tag{7.24}$$

Correction Set 2

Correction set 2 is based on tests with three oscillation periods as a function of the forced heave amplitude. The results have been normalized with respect to the freeboard. The correction factors, shown in Figure 7.7, are calculated from the results shown in Figure 8.16.

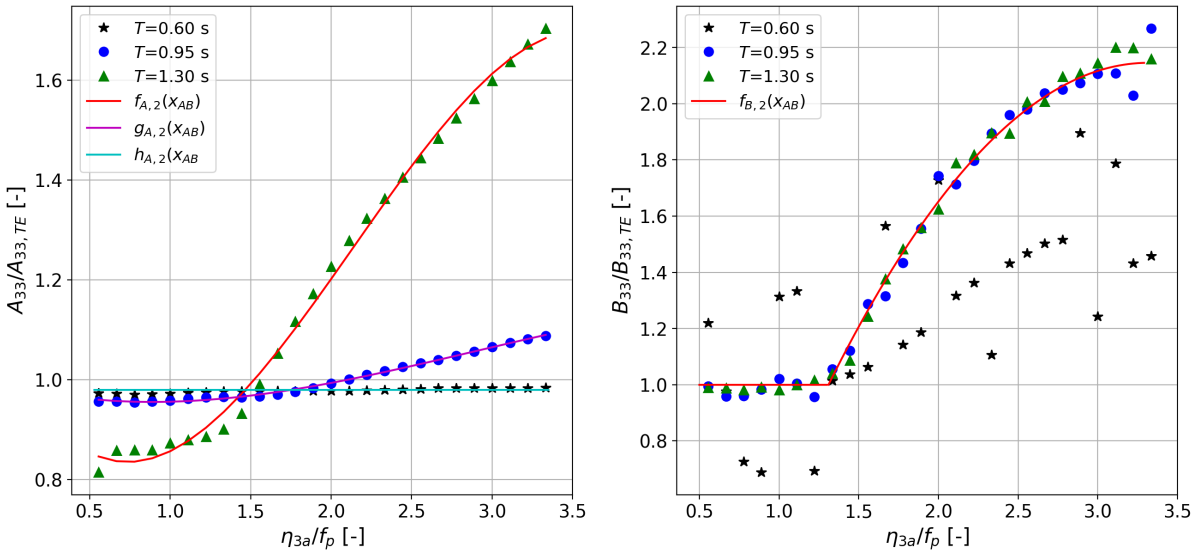

(a) Added mass **(b)** Damping

Figure 7.7: Added mass and damping without top extension (TE) relative to with top extension (TE) as a function of the oscillation period.

A new set of functions describing the trend of the correction factors were again found by poly-fitting. For damping, no clear trend was observed for T=0.60 s. Therefore, the damping is not corrected for periods lower than 0.95 s in model-scale and 5.7 s in full-scale, i.e. a factor of 1.0 is used for lower periods. T=0.60 s and T=1.30 s show a similar trend, and the same function is therefore used for those periods. The functions plotted in Figure 7.7 is written below:

$$f_{A,2}(x_{AB}) = -0.08x_{AB}^3 + 0.50x_{AB}^2 - 0.61x_{AB} + 1.04 \tag{7.25}$$

$$g_{A,2}(x_{AB}) = -0.01x_{AB}^3 + 0.05x_{AB}^2 - 0.08x_{AB} + 0.99 \tag{7.26}$$

$$h_{A,2}(x_{AB}) = 0.98 \tag{7.27}$$

$$f_{B,2}(x_{AB}) = \begin{cases} 1.0 & \text{for } x_{AB} \leq 1.3 \\ -0.28x_{AB}^2 + 1.89x_{AB} - 0.98 & \text{for } 1.3 < x_{AB} < 3.3 \\ 2.2 & \text{for } 3.3 \leq x_{AB} \end{cases} \tag{7.28}$$

7.6 Time-Step Convergence

A time-step convergence study was performed to determine the necessary value and ensure that the solution is independent of the time-step. The steepness of 1/100 was chosen for the

refinement study and performed with both correction sets. As shown in Figure 7.8 and 7.9 has the results converged for a time-step of 0.25 s which are used for the further simulations.

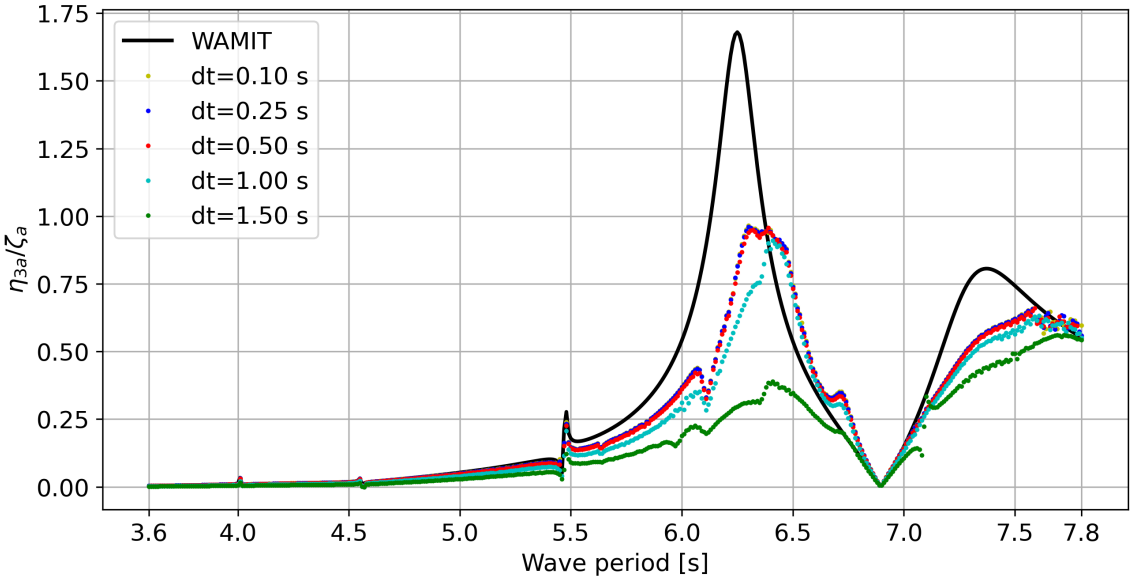

Figure 7.8: Time-step refinement with added mass and damping from correction set 1 and ϵ=1/100.

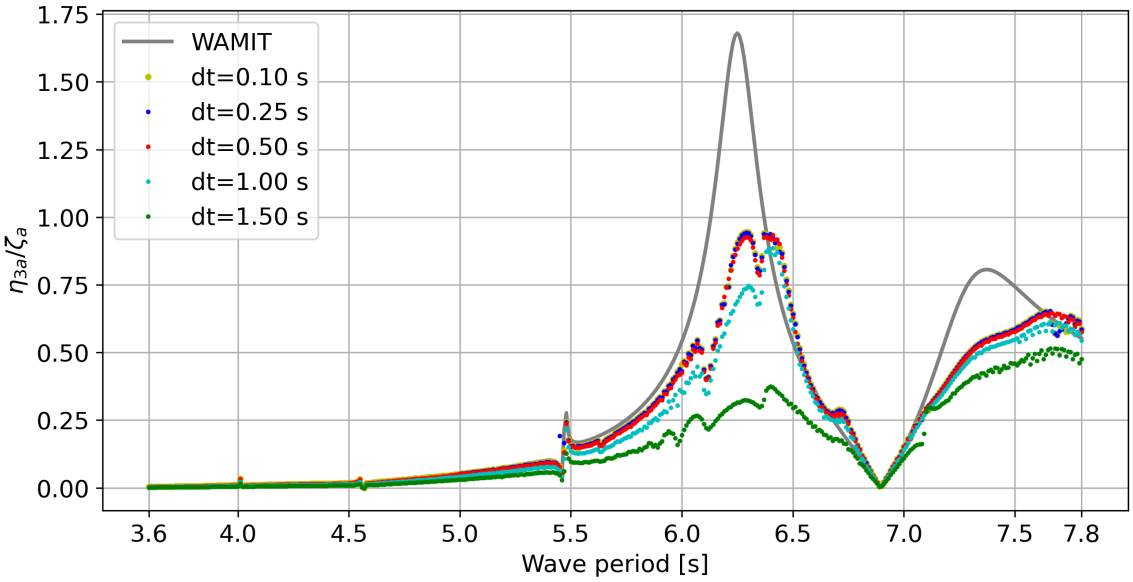

Figure 7.9: Time-step refinement with added mass and damping from correction set 2 and ϵ=1/100.

7.7 Test with Steepness of 1/1000

A final test to test the simulator was done by simulating waves with a steepness of 1/1000 while turning on all the non-linear corrections. Such a flat wave should not cause any significant non-linear effects, and the motions should be equal to the linear solution from WAMIT.

Figure 7.10 shows the results for both correction sets together with the linear solution from WAMIT. Both correction sets result in approximately the same motions as the linear WAMIT solution. However, correction set 1 deviate slightly by having a higher peak resonance period and larger resonance motions. Correction set 2, on the other hand, does not show any notice-

able differences compared to the WAMIT RAO. Even though correction set 1 showed a slight deviation, are the results still assumed to be acceptable.

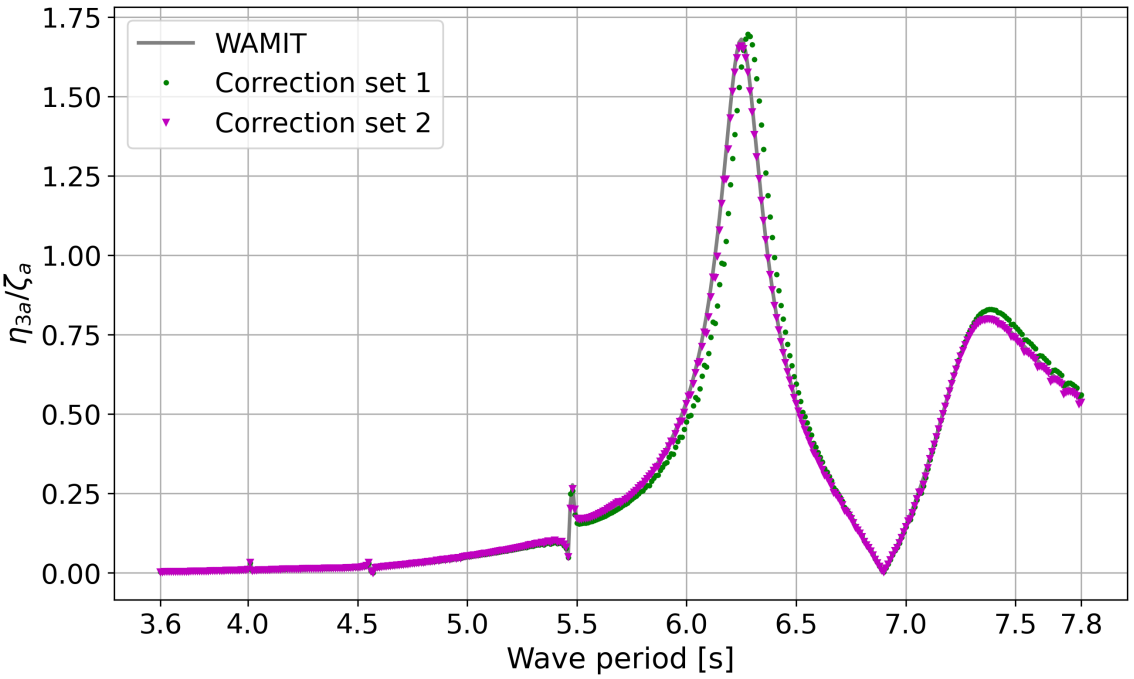

Figure 7.10: Heave RAO for incident waves with ϵ=1/1000 with non-linear corrections.

Chapter 8

Results and Discussion

This chapter presents the results and findings of this study. First, the linear motions from WAMIT are presented. Then, the forces, added mass and damping found from the experiments and CFD simulations follow. Last, the non-linear heave motions from the time domain are presented.

8.1 WAMIT

The most relevant results from WAMIT are presented in this section. These include the motion RAOs and an example of pressure distribution for one period. Plots of added mass, damping and excitation can be found in Appendix A.

8.1.1 Motion RAO

The Response Amplitude Operators (RAOs) in surge, heave and pitch are shown below in Figure 8.1, 8.2 and 8.3, respectively. Due to the symmetric geometry and wave heading, sway, roll, and yaw are not motions of interest.

Figure 8.1 shows the RAO in surge. The response converges towards 1.0 when the wave period goes to infinite as expected.

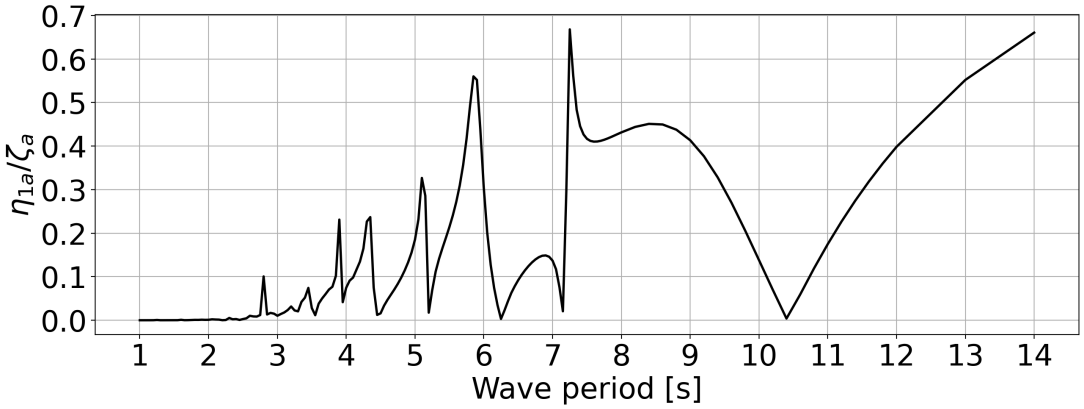

Figure 8.1: Surge

Figure 8.2 shows the RAO in heave. Here, two main response peaks can be observed for periods of 6.25 s and 7.35 s. The heave motion is close to zero for the wave period of 6.90 s between the two peaks. It is believed that the low heave motion at T=6.90 s is caused by

cancellation effects of the heave force. The force in heave can be found in Appendix A.4 together with the excitation forces in surge and pitch. It can be observed that the heave force is close to zero for wave periods of 6.90 s, which results in low heave motion. The cancellation in heave excitation is believed to split up the heave resonance motion into the two peaks shown in Figure 8.2. So without the heave cancellation effect, the heave motion would most likely have only one peak period between 6.25 s and 7.35 s. It is further believed that this single heave resonance motion would be greater than the motion with heave cancellation. This is a positive effect of the design and reduces heave motion. The heave motions converge towards 1.0 when the wave periods go to infinite, as expected.

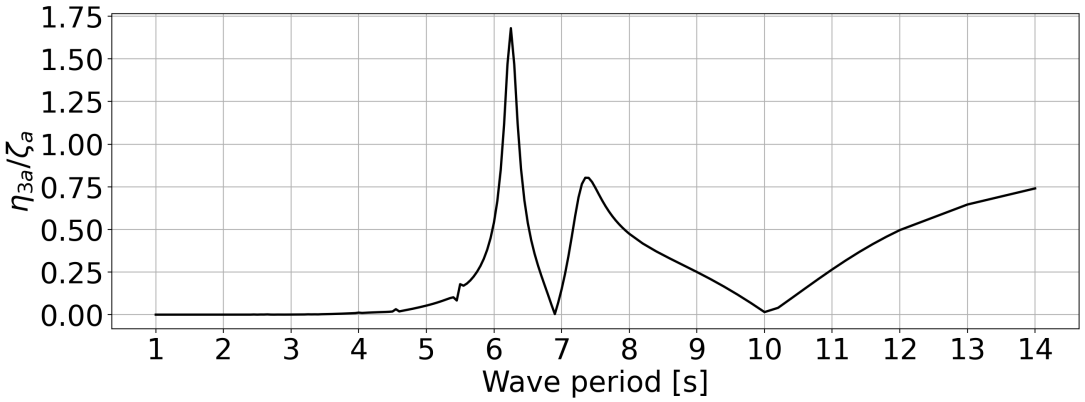

Figure 8.2: Heave

Figure 8.3 shows the pitch RAO. Low pitch motions are found for wave periods below around 7 s. The pitch resonance period is found to be 7.25 s.

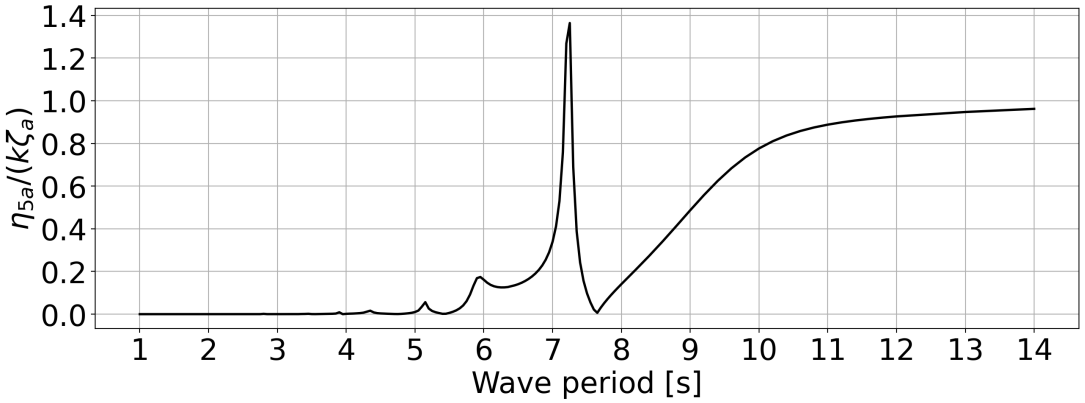

Figure 8.3: Pitch

8.1.2 Pressure Distribution

The panel pressures from the diffraction and heave radiation problem for T=6.0 s are visualized in Figure 8.4 and 8.5, respectively. It shows a top view of the pressures at the bottom panels of the pontoon and centre tank. With bottom panels, it is meant the horizontal panels underneath the pontoons, ie. 6.7 m below the mean free surface. The period of 6.0 s is shown as an example of what the pressure distribution looks like. These pressures are modified in the time domain simulator when accounting for the overtopping and pontoon deck flooding.

The incident wave direction is indicated with an arrow in Figure 8.4. It can be observed that, in general, the pressures are higher at the left side of the structure, i.e. the part of the structure pointing towards the incoming waves. It is intuitive that the part which first gets struck by the

waves experiences the highest forces, while the rear part, which is somewhat sheltered by the front, experiences lower forces.

Additional plots of the diffraction and radiation pressures for the wave periods causing the two maximum and the minimum heave motions, i.e. T=6.25 s, T=6.90 s and T=7.35 s can be found in Appendix A.5.

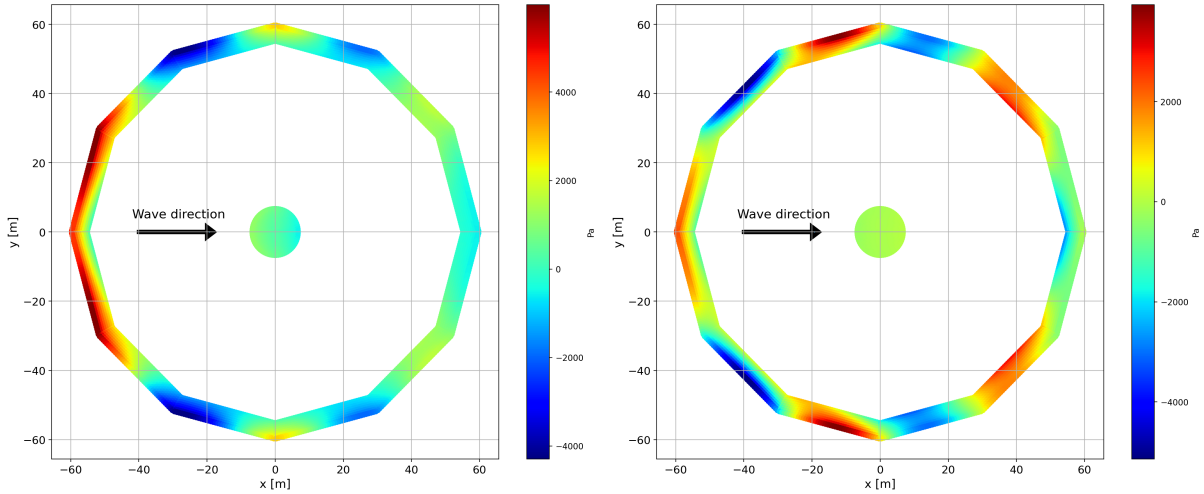

(a) Real part **(b)** Imaginary part

Figure 8.4: Pressure distribution on the bottom panels from the diffraction potential for a incident wave with T=6.0 s.

The radiation pressure from heave motion is shown in Figure 8.5. The real part corresponds to added mass, while the imaginary part corresponds to damping.

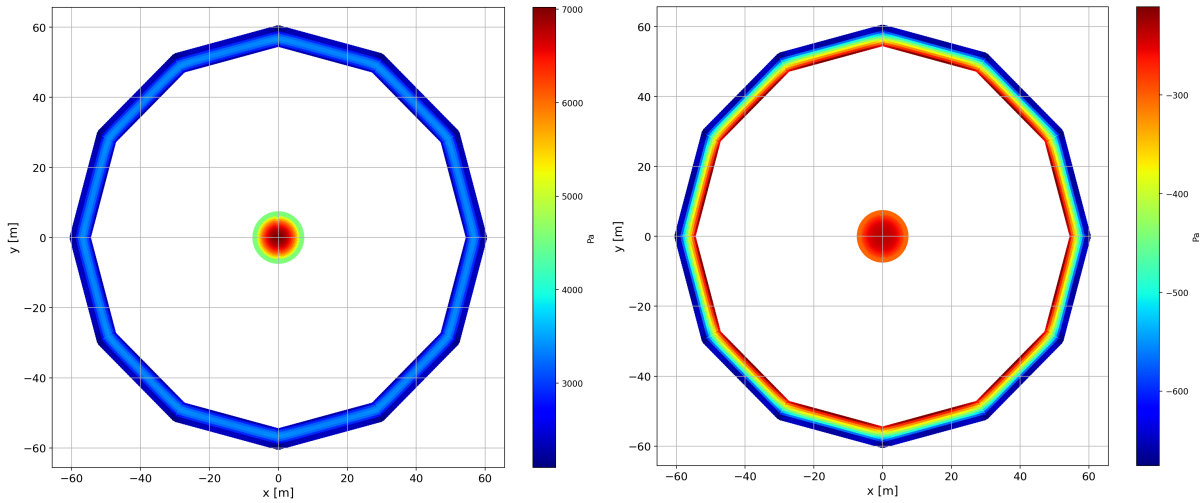

(a) Real part **(b)** Imaginary part

Figure 8.5: Pressure distribution from the radiation potential from heave motion with oscillation period of 6.0 s.

8.2 2D Experimental and CFD Results

This section presents mainly the experimental results. In addition, the wave-induced forces found from the CFD simulations are plotted together with the experimental results. First, wave-induced forces on the fixed pontoon are presented both as functions of wave period and

steepness. Thereafter follows the added mass and damping results from the forced heave test. Lastly, the wave transmission over the pontoon is presented.

Images showing a comparison between the wave overtopping from the CFD simulations and experiments can be foun in Appendix E, which generally shows good correspondence by visually inspecting the images.

Appendix F shows images of the maximum experimental overtopping with wave steepness of 1/30 for periods ranging from 0.6 s to 1.3 s with 0.1 s increment.

8.2.1 Wave-Induced Forces

Figure 8.6 and 8.7 shows the pontoon without and with top extension, respectively, in incident waves with ϵ=1/60, T=1.3 s and H=0.043 m. It can be observed that the pontoon without top extension experience significant wave overtopping. A comparison of the wave profile between the experiments and CFD simulations for a wave with ϵ=1/45, T=1.3, and H=0.058 m can be found in Appendix E, which show relatively well correspondence between the two methods.

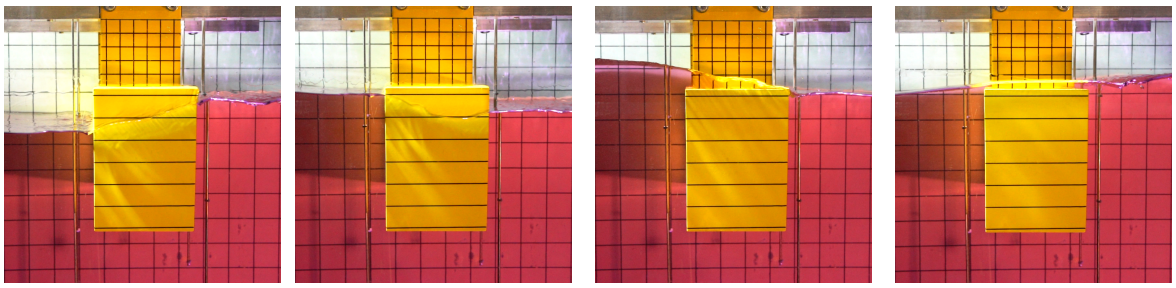

(a) **(b)** **(c)** **(d)**

Figure 8.6: Incident waves on the pontoon without top extension. The wave steepness i 1/60, the wave period is 1.3 s, and the wave height is 0.043 m.

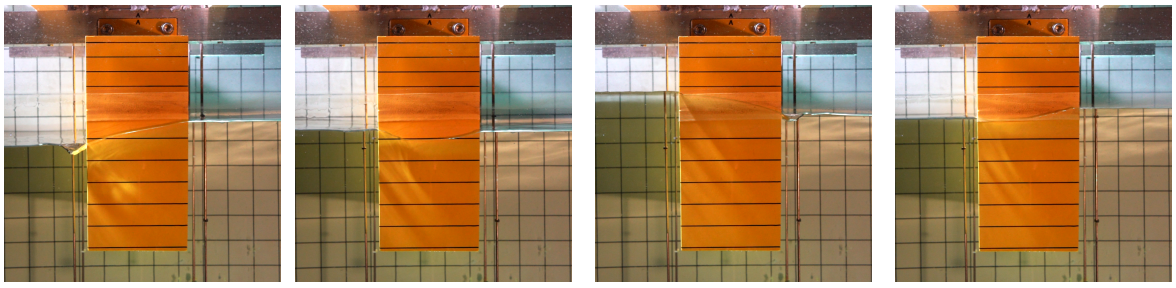

(a) **(b)** **(c)** **(d)**

Figure 8.7: Incident waves on the pontoon with top extension. The wave steepness i 1/60, the wave period is 1.3 s, and the wave height is 0.043 m.

The harmonic wave-induced horizontal and vertical forces are shown in Figure 8.8 and 8.10, respectively. For both the horizontal and vertical forces, the normalized first harmonic forces increase for decreasing steepnesses, i.e. ϵ=1/100 gives larger forces than ϵ=1/60, and so on. The only exception is the normalized vertical forces with the steepness of 1/30, 1/25 and 1/20, which results in approximately the same forces. This is elaborated further below.

This can be explained by steeper and higher waves causing an increased level of overtopping, which seems to reduce the forces in both directions. The horizontal forces are reduced because an increasing level of overtopping means that an increasing amount of water flows over the pontoon instead of getting stopped by the pontoon.

The trend for the second and third-order forces is opposite of the first order. Here is the general trend that steeper waves result in greater normalized forces.

The results from the CFD simulations, plotted with square dots, show increasingly agreement with the experimental results for increasing wave periods. This is most likely a result of the simulated waves corresponding better to the specified wave heights for higher periods. It is not expected that the CFD simulations and experiments return the same forces. However, they should be of approximately the same magnitude.

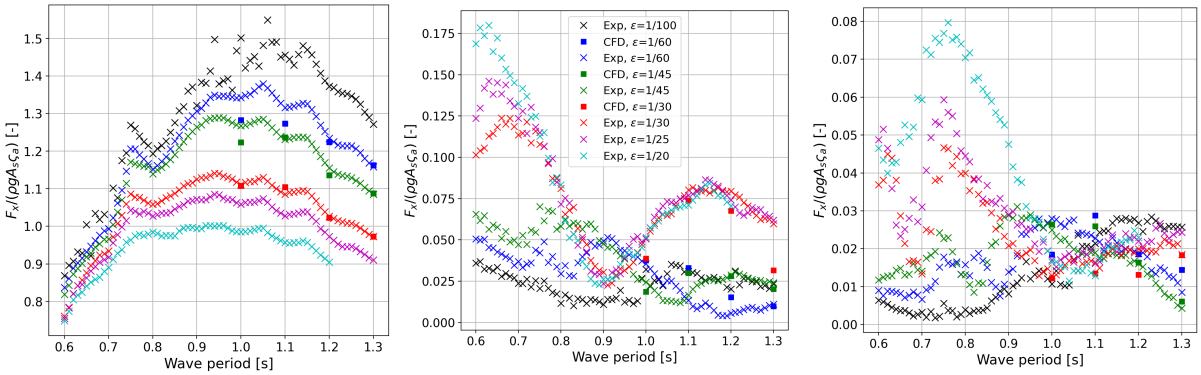

(a) 1st harmonic **(b)** 2nd harmonic **(c)** 3rd harmonic

Figure 8.8: Horizontal harmonic forces from experiments and CFD simulations as function of wave period.

The vertical first harmonic force is reduced because the water flowing over the pontoon pushes the pontoon down. The overtopping occurs when the wave crest hits the pontoon. Furthermore, since the dynamic pressure from the wave is in phase with the wave elevation, will the dynamic pressure from the wave mainly be positive during the overtopping. The positive dynamic pressure will result in a vertical force which pushes upwards. And since the water flowing over the pontoon gives a force downwards, does the overtopping result in vertical forces upwards.

Figure 8.9 shows the raw signal of the vertical force on the pontoon from a wave causing significant overtopping from the experiments. The positive force amplitudes reach just over 10 N, while the negative force amplitudes are three times greater. This shows how the water on top of the pontoon reduces the positive force amplitudes on the pontoon.

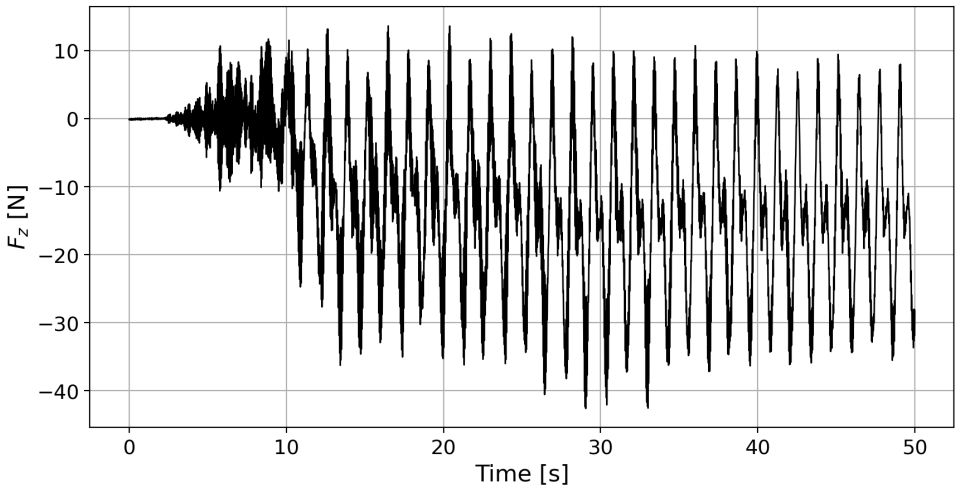

Figure 8.9: Raw signal of the vertical force from waves with ϵ=1/30, T=1.3 s and H=0.087 m from the experiment. No other filter than the Butterworth has been applied.

The normalized first-order vertical forces, Figure 8.10a, converge for the steepness of 1/30,

1/25 and 1/20, as mentioned above. A hypothesis for these results is that the difference in wave amplitude, ζ_a, for the mentioned steepnesses gives a similar increase in the amount of water flowing over the pontoon. In that way, the increased force from the higher and steeper wave will be balanced out by the overtopped water. However, this hypothesis has not been verified and should be investigated further.

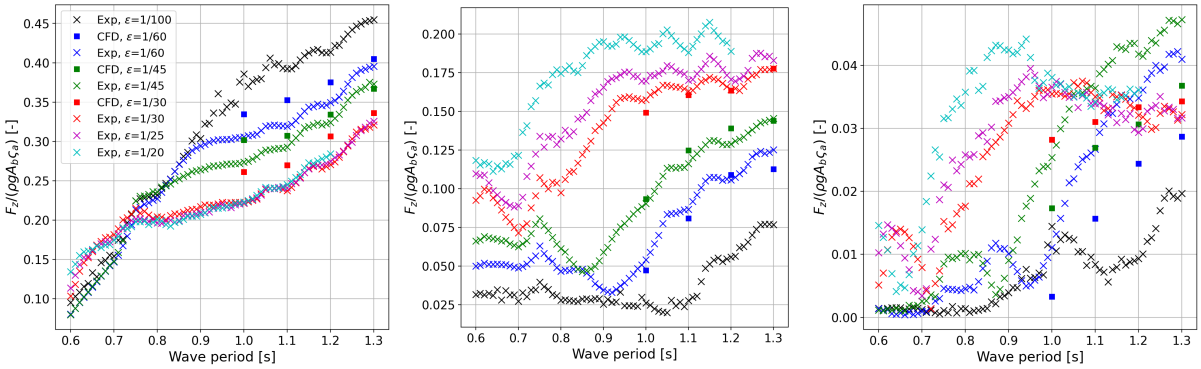

(a) 1st harmonic **(b)** 2nd harmonic **(c)** 3rd harmonic

Figure 8.10: Vertical harmonic forces from experiments and CFD simulations as function of wave period.

Figure 8.11 and 8.12 shows the harmonic horizontal and vertical experimental forces both with and without the top extension (TE). These results are also used to find the excitation correction factors.

The horizontal forces for T=0.60 s show little difference regarding the top extension compared to T=0.95 s and 1.30 s. The purpose of the top extension is to prevent wave overtopping. However, significant overtopping does not occur for periods of 0.60 s.

For the pontoon with top extension, does periods of 0.95 s and 1.30 s result in larger forces than the pontoon without the top extension. This can mainly be explained because the top extension prevents the water from flowing over the pontoon and instead absorbs the energy by stopping it.

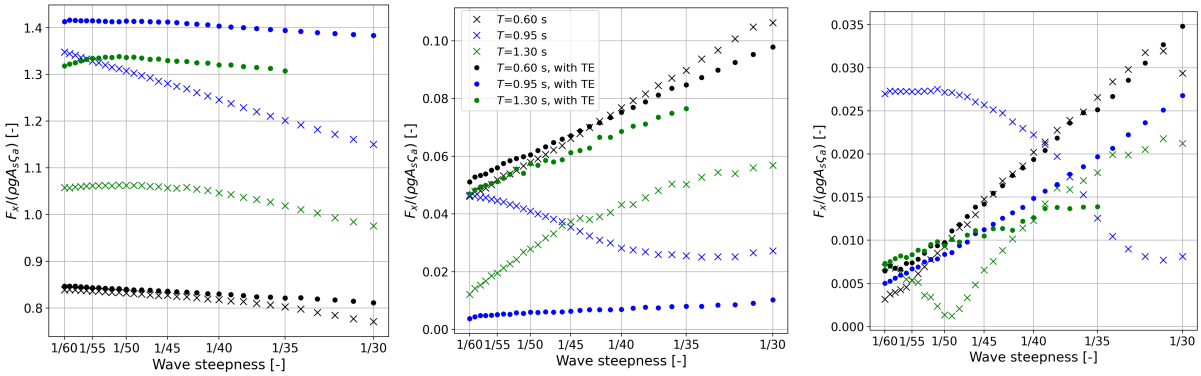

(a) 1st harmonic **(b)** 2nd harmonic **(c)** 3rd harmonic

Figure 8.11: Horizontal harmonic forces from experiments as a function of wave steepness. The crosses mark the results without the top extension, while the dots mark the results with the top extension (TE). Waves steeper than 1/35 were not performed with T=1.30 s because it caused the water to climb above the top extension filling it with water.

The vertical harmonic forces with and without the top extension are more comparable than the horizontal forces because the top extension has no normal component in the vertical direction.

The normalized first harmonic vertical forces, as shown in Figure 8.12a, show little variation due to wave steepness for the case with top extension. Without the top extension, the forces decrease with steeper and thus also higher waves. This shows again that the overtopping effect reduces the vertical forces.

The magnitude of the second and third harmonic forces compared with the first harmonic is significantly greater for the vertical forces than for the horizontal. For example, for ϵ=1/30 and T=1.30 s, is the second harmonic vertical forces around 55 % of the first harmonic magnitude, while the third harmonic is 10 %. The same percentages for the horizontal forces is 6 % and 2 %, respectively. So the vertical forces are more dominated by higher-order forces than the horizontal.

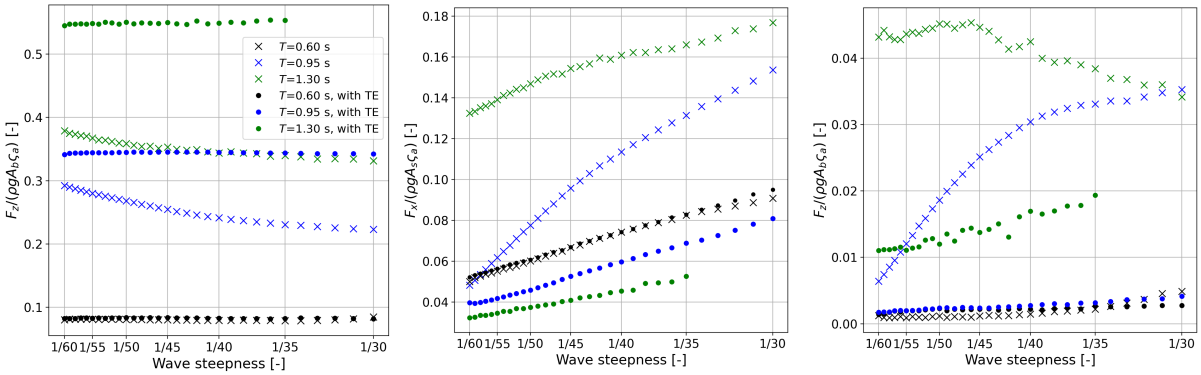

(a) 1st harmonic **(b)** 2nd harmonic **(c)** 3rd harmonic

Figure 8.12: Vertical harmonic forces from experiments as a function of wave steepness. The crosses mark the results without the top extension, while the dots mark the results with the top extension (TE). Waves steeper than ϵ=1/35 were not performed with T=1.30 s because it caused the water to climb above the top extension filling it with water.

8.2.2 Added Mass and Damping

Figure 8.13 and 8.14 is from the forced heave tests without and with the top extension, respectively, with motion amplitude of 3.0 cm and osciallltion period of 0.95 s. Significant amount of pontoon deck flooding can be observed for the model without top extension.

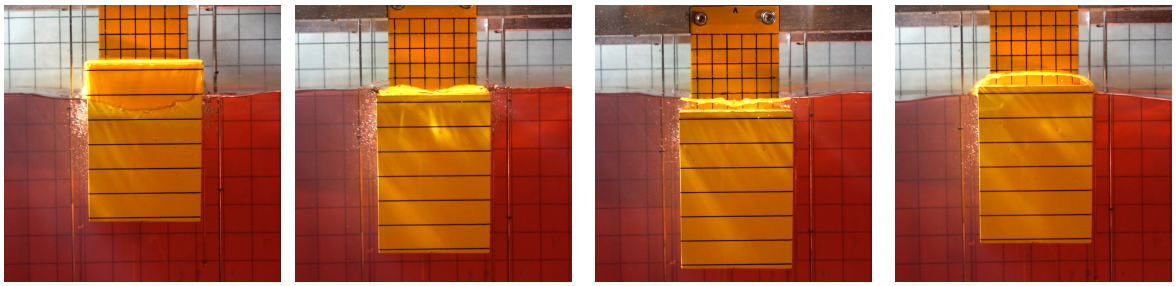

(a) **(b)** **(c)** **(d)**

Figure 8.13: Forced heave of pontoon without top extension. The heave amplitude is 3.0 cm and period of 0.95 s.

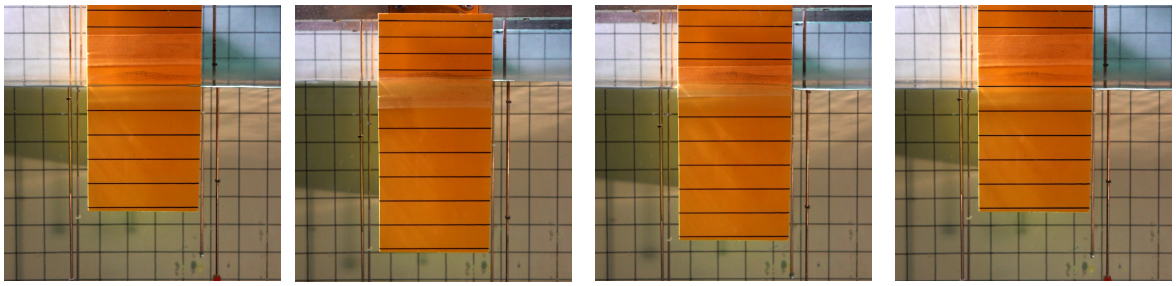

(a) (b) (c) (d)

Figure 8.14: Forced heave of pontoon with top extension. The heave amplitude is 3.0 cm and period of 0.95 s.

The resulting 2D added mass and damping from the forced heave test in Ladertanken is presented as a function of oscillation period in Figure 8.15 and as a function of the normalized oscillation amplitude in Figure 8.16.

The added mass decreases with increasing oscillation period as shown in Figure 8.15a. The cases without the top extension (TE) gives, in general, higher added mass than with the top extension for oscillation amplitudes above 1.0 cm. These oscillation amplitudes caused pontoon deck flooding and indicate that the flooding contribute to increased added mass in heave.

The normalized 2D damping is shown in Figure 8.15b. Oscillation amplitude of 0.5 cm and 1.0 cm result in little differences between the pontoon with and without top extension. This is, again, because no significant flooding occurs for these motion amplitudes. For the oscillation amplitudes of 2.0 cm and 3.0 cm, the result is the same as the added mass. Pontoon deck flooding gives increased damping.

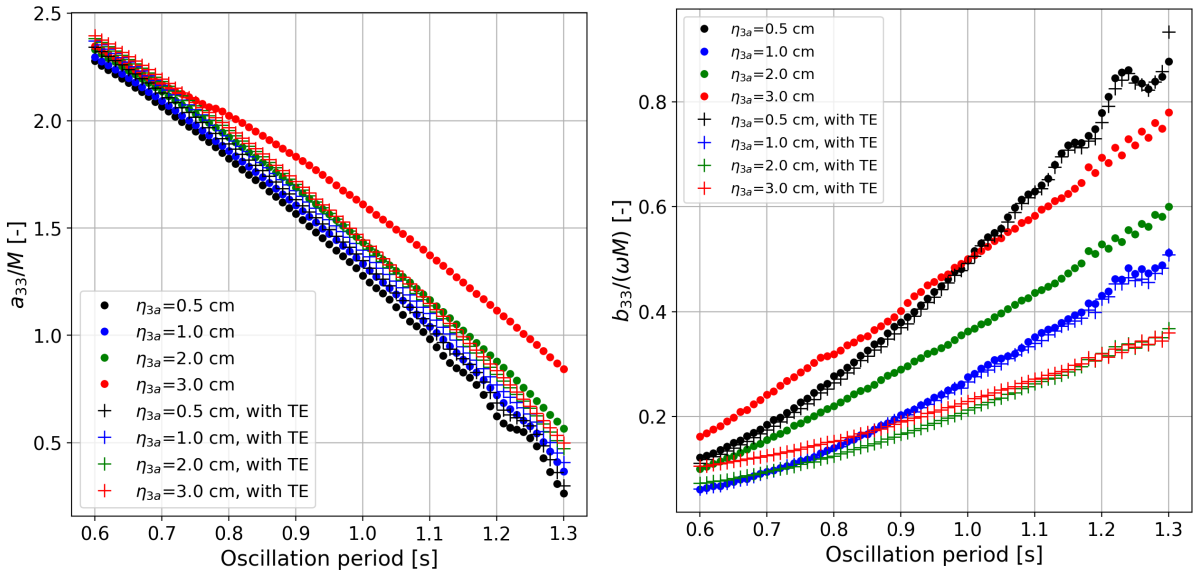

(a) Added mass **(b)** Damping

Figure 8.15: Experimental 2D added mass and damping for the pontoon model with and without top extension (TE) as a function of the oscillation period. The crosses mark the results with the top extension, while the dots mark the results without the top extension (TE).

The forced heave tests were also run as a function of the motion amplitude, with the results shown in Figure 8.16.

The added mass for the pontoon without the top extension surpasses the pontoon with top extension for η_{3a}/f_p equal to around 2.1 and 1.6 for T=0.95 s and T=1.30 s, respectively. For

damping, on the other hand, does the same happen for the same normalized motion amplitude of around 1.4.

When comparing the trends for added mass and damping in Figure 8.16, it is clear that the damping increase due to flooding is significantly greater than the added mass increase. The added mass and damping ratio between the two cases can be found in Figure 7.7.

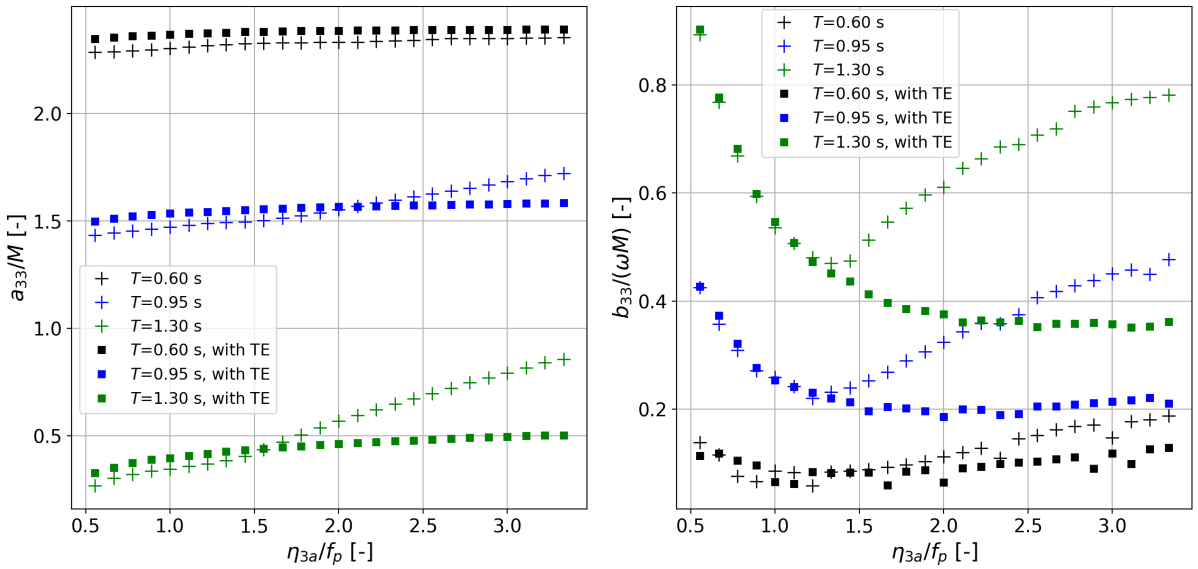

(a) Added mass

(b) Damping

Figure 8.16: Experimental 2D added mass and damping for the pontoon model with and without top extension (TE) as a function of heave amplitude relative to the freeboard. The crosses mark the results without the top extension, while the squares mark the results with the top extension (TE).

8.2.3 Wave Radiation Damping

The wave radiation damping, described in section 2.4.3, is shown in Figure 8.17 and 8.18 relative to the oscillation period and amplitude, respectively. The radiation damping depends on the far-field wave amplitude, angular oscillation frequency and motion amplitude.

For heave amplitudes, η_{3a}, of 0.5 cm and 1.0 cm, is the total damping approximately equal with and without the top extension. On the other hand, the total damping differs significantly from the wave radiated damping for motion amplitudes of 2.0 cm and 3.0 cm.

The results from the wave radiated damping has not been used for establishing damping corrections factors in this thesis. However, this could have been done to create a third correction set for the damping.

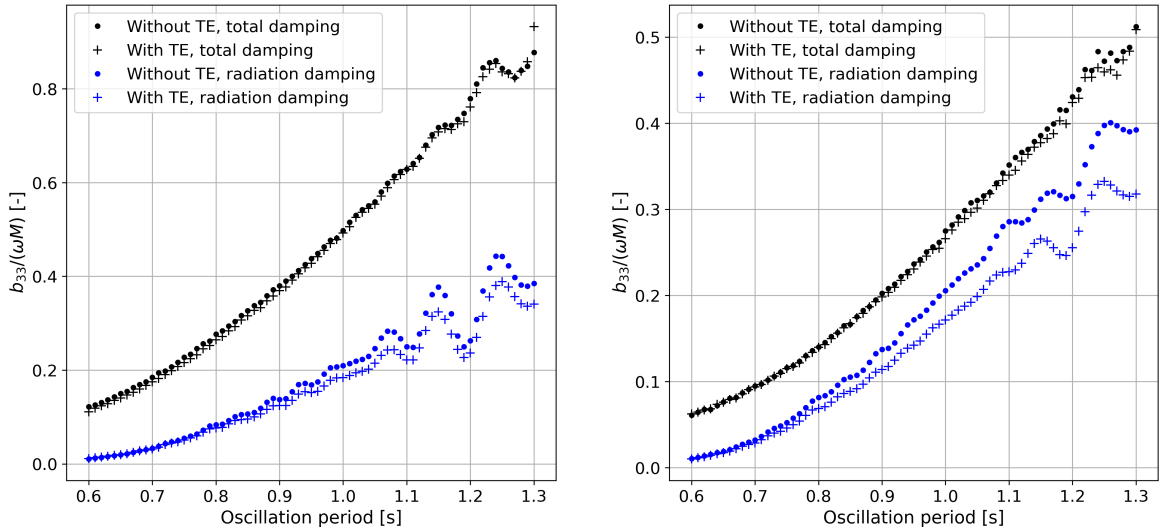

(a) η_{3a}=0.5 cm

(b) η_{3a}=1.0 cm

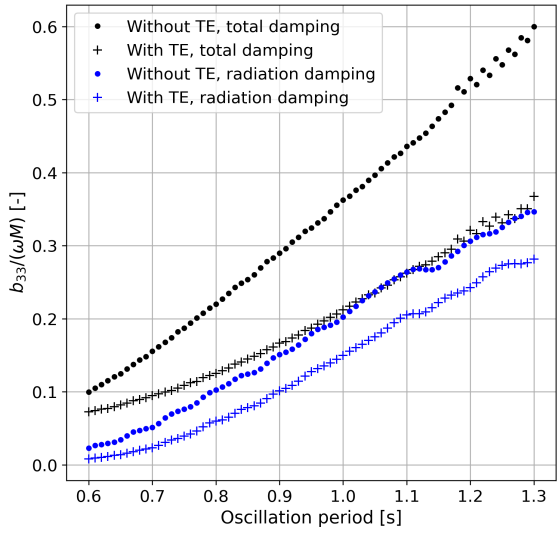

(c) η_{3a}=2.0 cm

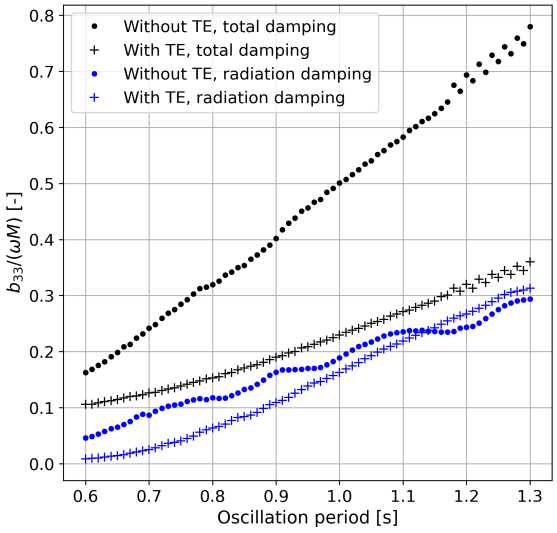

(d) η_{3a}=3.0 cm

Figure 8.17: Wave radiation damping compared with the total damping for oscillation amplitudes of 0.5 cm, 1.0 cm, 2.0 cm and 3.0 cm with and without top extension (TE).

Figure 8.18 shows the wave radiated damping plotted against the normalized heave motion amplitude. Higher wave radiation damping values are measured for the pontoon without the top extension compared to the pontoon with T=0.60 s and T=0.95 s. This means that the pontoon without the top extensions creates higher outgoing waves than for the contrary. However, the total damping also increases for the pontoon without the top extension for approximately the same normalized amplitudes.

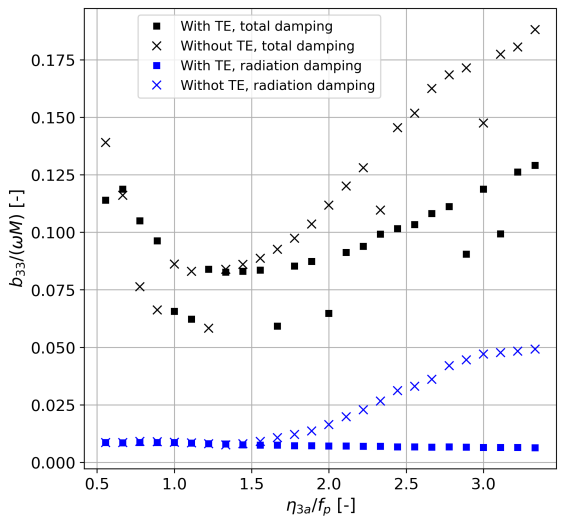

(a) T=0.60 s

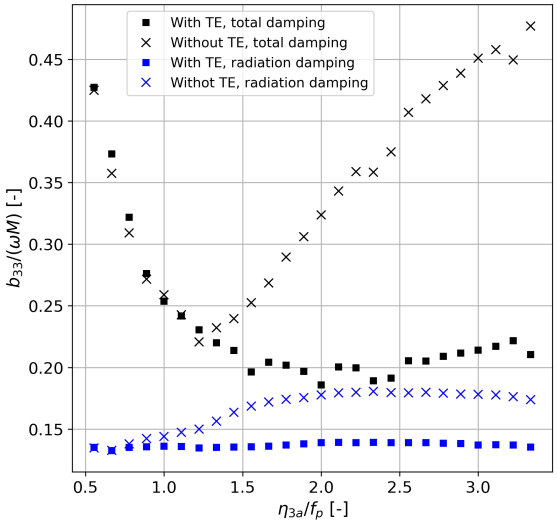

(b) T=0.95 s

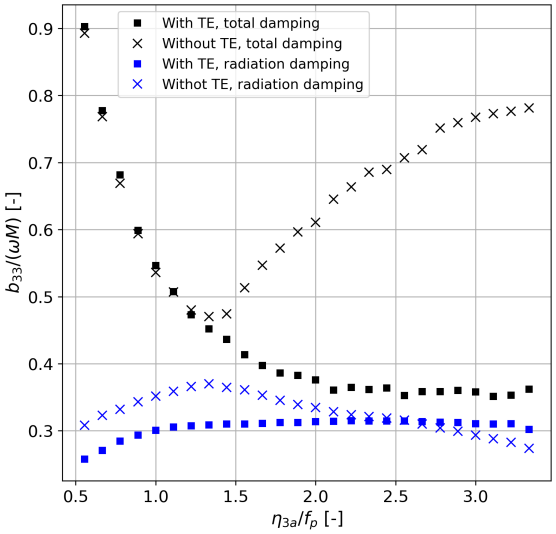

(c) T=1.30 s

Figure 8.18: Wave radiation damping compared with the total damping for oscillation periods of 0.60 s, 0.95 s and 1.30 s with and without top extension (TE).

8.2.4 Wave Transmission Over the Pontoon

The wave transmission over the pontoon is studied by looking at the measured wave height behind the model. Figure 8.19a shows the wave amplitude measured 2.0 m behind the pontoon model for four steepnesses as a function of the incident wave period, while Figure 8.19b shows the same results plotted against the normalized incident wave amplitude.

The results show that for the same wave period, steeper waves cause larger waves behind the model as well. This is expected because steeper waves give a higher incident wave amplitude in the first place. However, the trend is the opposite if the incident wave amplitude is considered, as shown in Figure 8.19b. Here, lower wave steepnesses give larger transmitted wave amplitudes for the same normalized incident wave amplitude because the wave periods are longer.

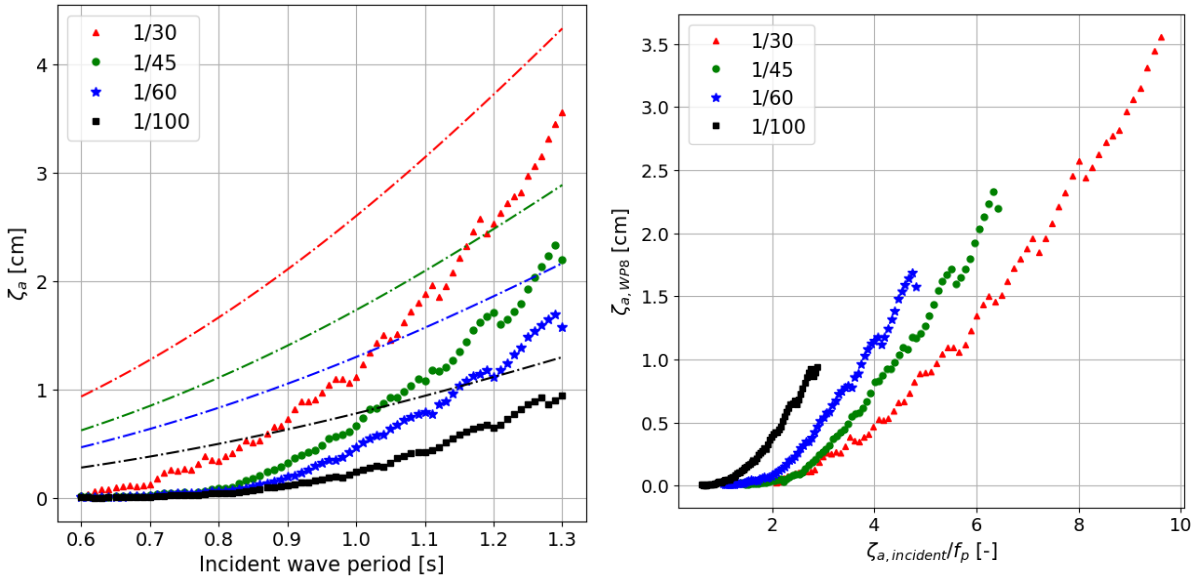

(a) (b)

Figure 8.19: 1st harmonic wave amplitude measured 2.0 m behind the pontoon model from experiments. The stippled line marks the theoretical incident wave amplitude. The two plots show the same result visualized with two different horizontal axes.

8.3 Non-linear Heave Motion from the Time-Domain Simulator

The non-linear motions in heave found with the time domain simulator are presented in this section. These results combine the linear motions from WAMIT with the non-linear effects found in the experiments and CFD simulations. The heave motions will be presented as RAOs, which are the main results of the thesis. First is the heave RAO with all non-linearities accounted for presented with steepness of 1/60, followed by non-linear motions where only one factor is modified. For example, only non-linear added mass, while damping, restoring and excitation are linear. In this way, each non-linear factor can be studied separately to see the effect they are causing.

All results are presented with both correction sets separately to show any differences. For completeness, this is done even if no significant difference is noticeable.

8.3.1 Non-Linear Heave Motion with Steepness of 1/60

Figure 8.2 shows the non-linear heave RAO for waves with the steepness of 1/60 and includes all non-linear the non-linear correction factors. Waves with a period of 6.5 s, for example, will have a wave height of 1.1 m. Some unexpectedly high motions are shown around T=5.5 s should be disregarded. They are most likely caused by the excitation correction factor and is described further below.

The maximum normalized heave response is reduced significantly from around 1.7 to 0.75 due to the non-linear effects. The peak period is also slightly shifted towards higher wave periods. Correction sets 1 and 2 result in relatively similar results, which increase the reliability of the results.

The sudden local motion troughs at periods around 6.1 s and 6.7 s are also assumed to be caused by the excitation correction factors. This is elaborated briefly in section 8.3.5.

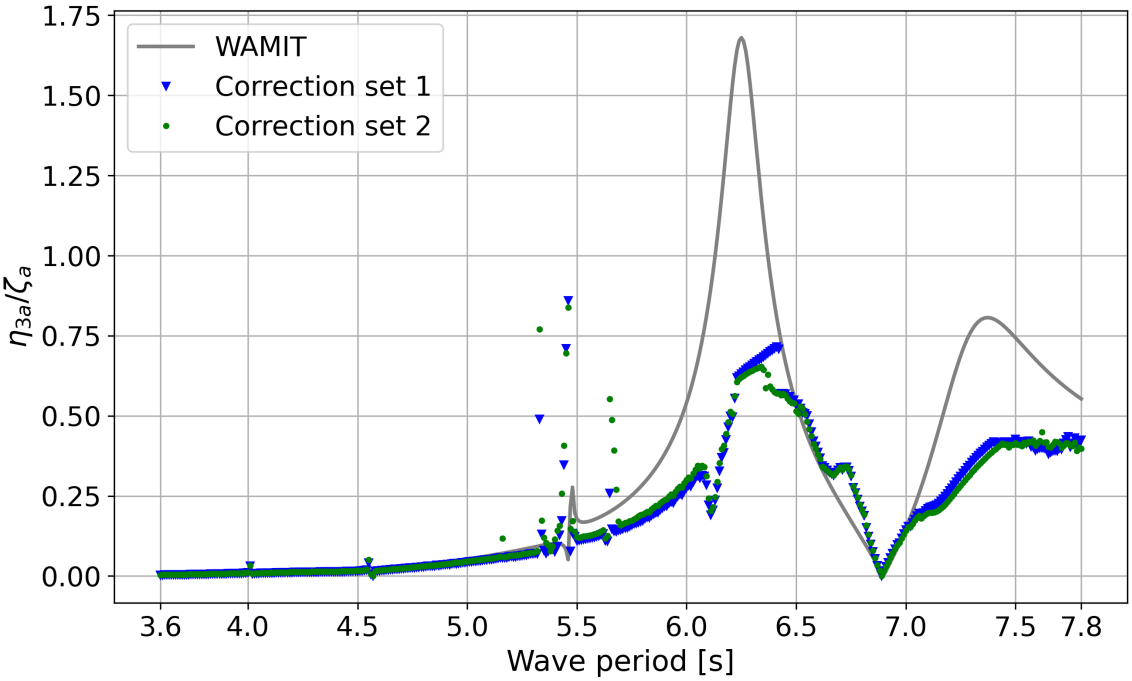

Figure 8.20: Heave RAO for waves with steepness of 1/60. Non-linear correction factors have been applied for the added mass, damping, and excitation. In addition is the non-linear restoring simulated.

8.3.2 Effect of Wave Steepness

Figure 8.21 shows the effect of wave steepness for both correction sets. The general trend is lower motions for increasing steepness. This can be explained by steeper waves causing more overtopping and flooding, increasing damping and reducing excitation forces.

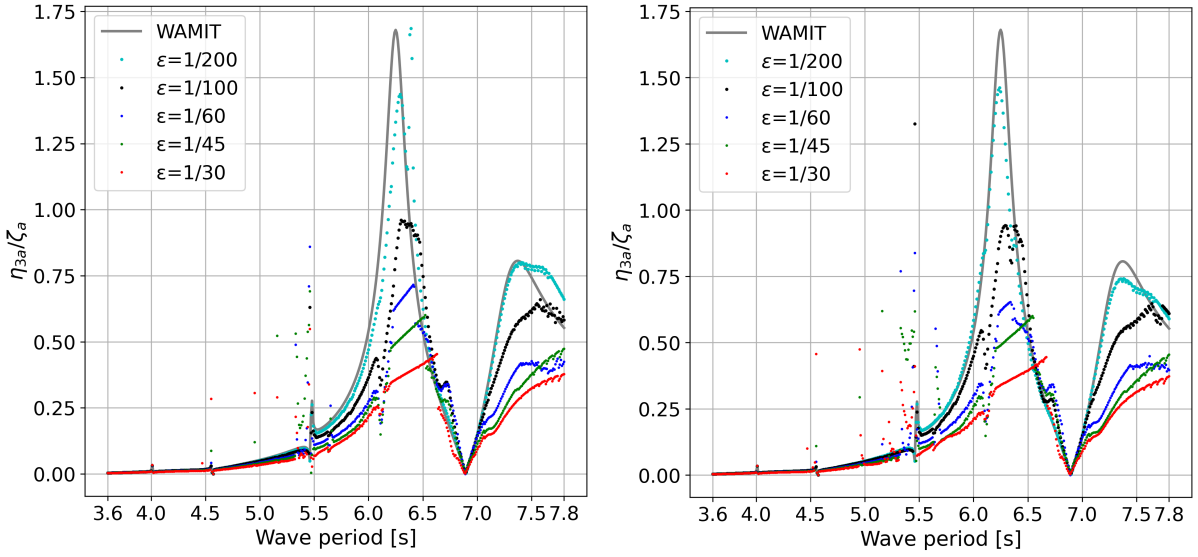

(a) Correction set 1

(b) Correction set 2

Figure 8.21: Heave RAO with modified radiation and diffraction pressure

8.3.3 Effect of Non-Linear Added Mass

For the results presented in Figure 8.22, only the added mass pressures are modified, while damping, restoring and excitation are unchanged. This causes mainly two effects.

The two heave resonance periods are both shifted slightly towards a higher period. This is expected according to the theory where the natural undamped heave period can be calculated by Equation 2.37 where $T_{n,3}$ increase when A_{33} increase.

The second effect is an increased resonance motion compared with the linear RAO from WAMIT. Cancellation effects in heave excitation force is assumed to cause the low response for wave periods around 6.8 s, which splits the heave resonance peak into two lower peaks. It is likely that the resonance motion without the cancellation effect would be larger than the peaks shown in Figure 8.22 and be located between the two peaks. This can explain why the motions increase when shifted towards higher wave periods.

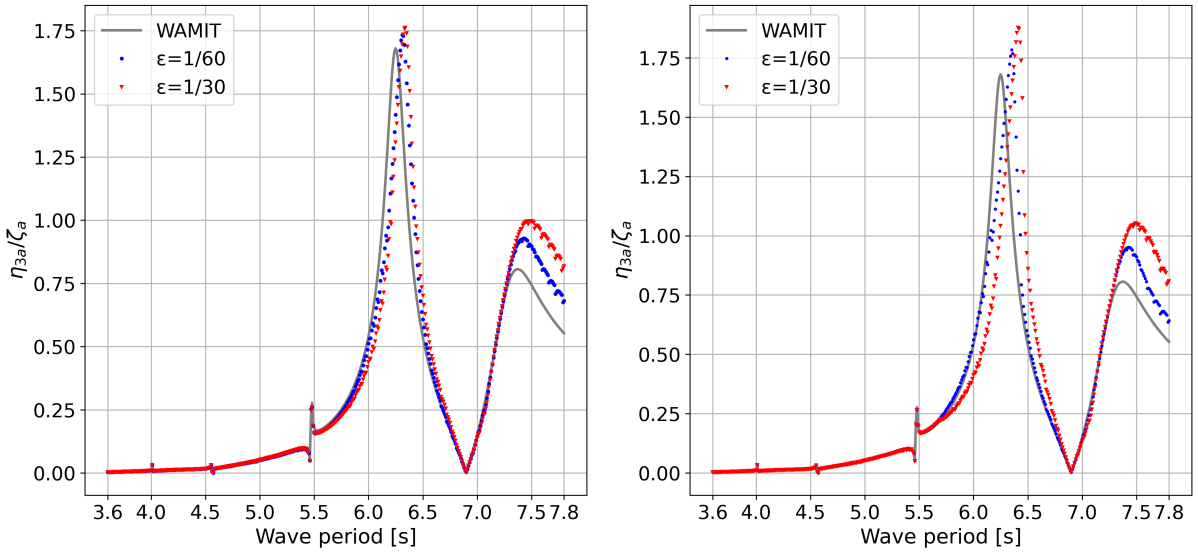

(a) Correction set 1

(b) Correction set 2

Figure 8.22: Heave RAO with only modified added mass.

8.3.4 Effect of Non-Linear Damping

As described in section 2.4.2, damping is related to energy leaving the system and thus reducing the motions. The damping is increasing for increasing levels of pontoon flooding. Furthermore, the simulator's damping correction factors are never less than 1.0. This leads to the reduced motions shown in Figure 8.23.

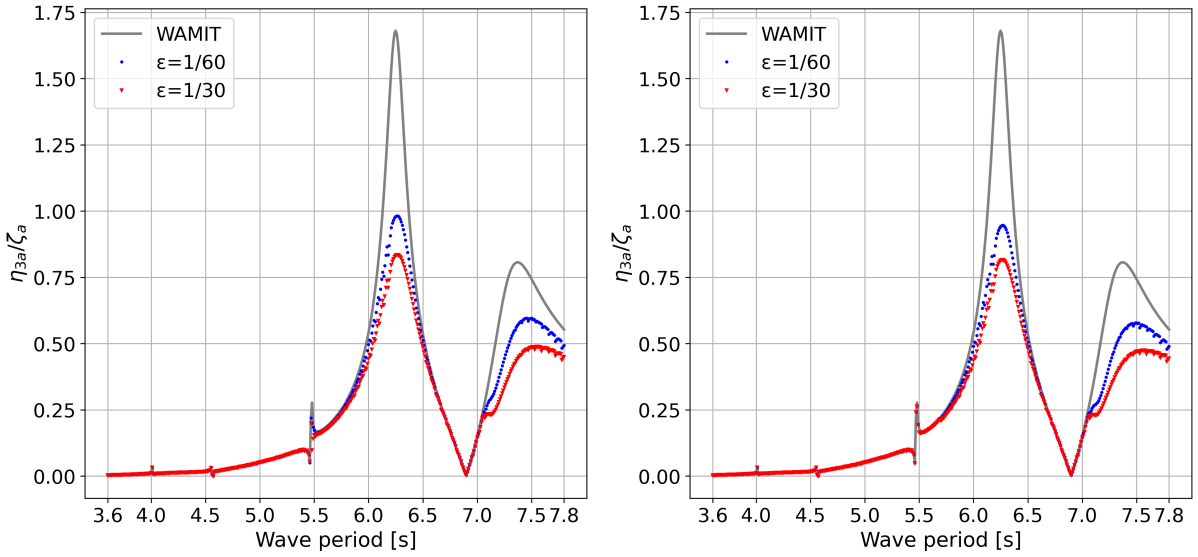

(a) Correction set 1

(b) Correction set 2

Figure 8.23: Heave RAO with only modified damping

8.3.5 Effect of Non-Linear Excitation

The wave overtopping causes reduced excitation forces which intuitively reduces the motions as shown in Figure 8.24. The excitation correction factor also causes unexpectedly high motions for some periods lower than 5.7 s. These values should be disregarded.

The results from simulations with a steepness of 1/60 show a trough in the RAO for periods around 6.1 s and a trend that deviates from both WAMIT and the simulation with ϵ=1/30. It is assumed that the mentioned observations are caused by how the intervals in the correction factors are designed and should be disregarded. Alternatively, they should be investigated further before being trusted.

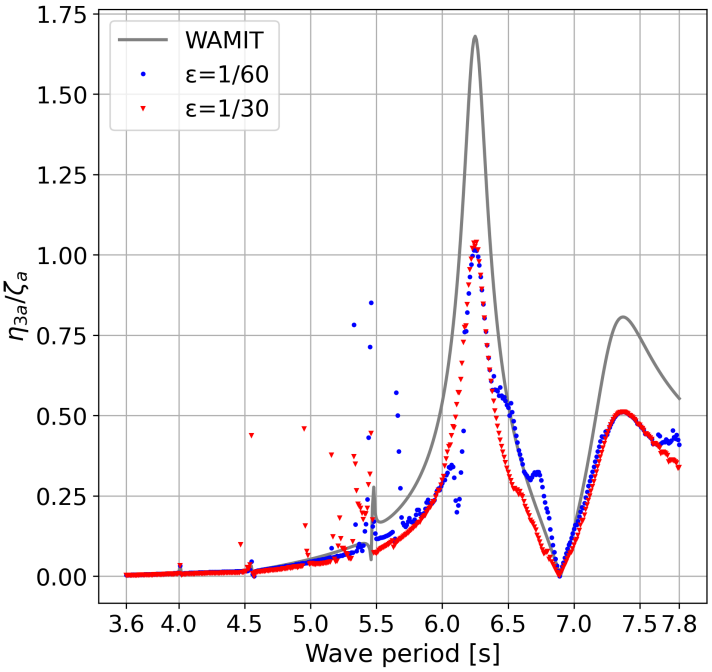

Figure 8.24: Heave RAO with only modified excitation

8.3.6 Effect of Non-Linear Added Mass and Damping

Figure 8.25 shows the results from simulations with only modified radiation pressure, i.e. added mass and damping. As expected, the motion is reduced because of the increased damping and the natural resonance period shifted slightly towards higher wave periods.

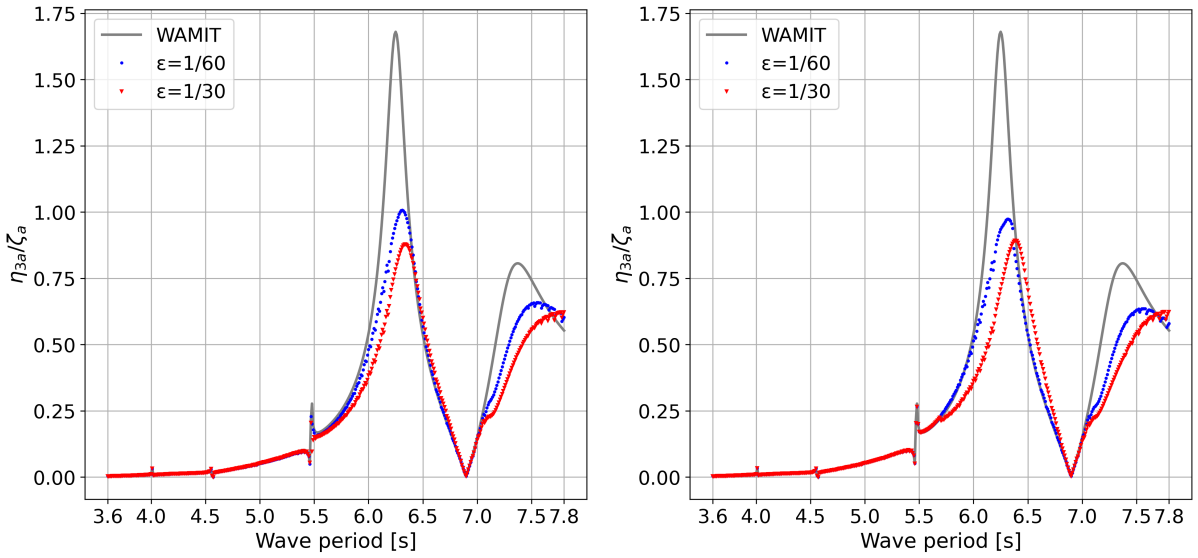

(a) Correction set 1 **(b)** Correction set 2

Figure 8.25: Heave RAO with only added mass and damping modified.

8.3.7 Effect of Non-Linear Added Mass, Damping and Restoring

Figure 8.26 shows the results of simulations when correcting for non-linear added mass, damping and restoring. Only the excitation correction is not applied. The RAO shows a linear increase of motion for wave periods between 6.0 s and 6.5 s for ϵ=1/60 and 6.7 s for ϵ=1/30. This is an effect of the non-linear restoring. The non-linear restoring affects the motions only when they become larger than the freeboard of 0.30 m.

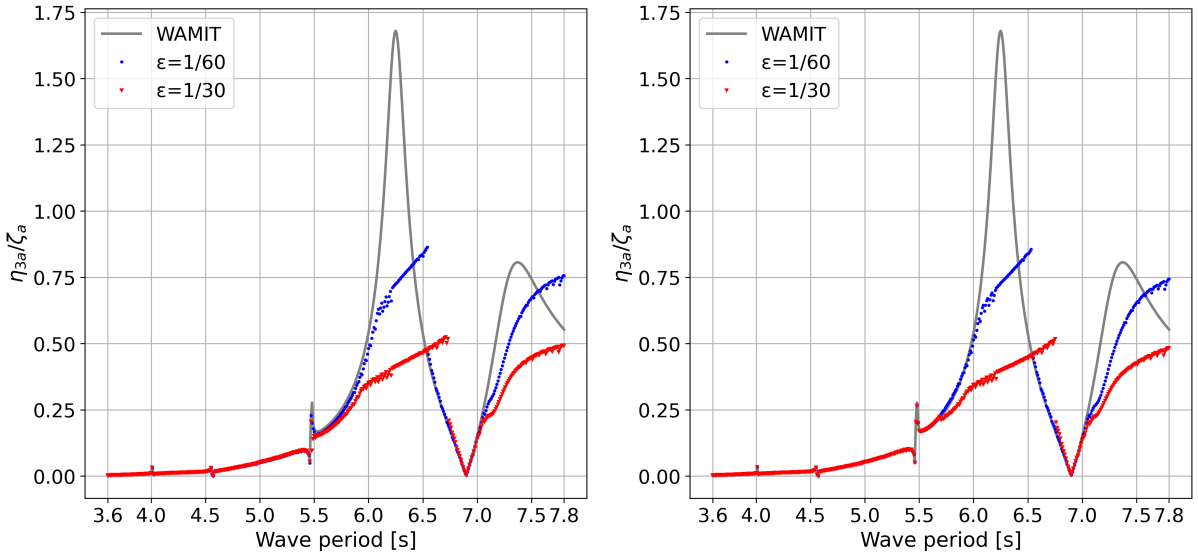

(a) Correction set 1 **(b)** Correction set 2

Figure 8.26: Heave RAO with only added mass, damping and restoring modified.

8.3.8 Effect of Non-Linear Restoring

The non-linear restoring effect is studied when added mass, damping, and excitation are corrected for non-linearities. Both correction sets result in approximately the same results.

The first observation noticeable is the unexpected large motions for low wave periods caused by the non-linear excitation correction. This is also discussed above in section 8.3.5.

Another interesting observation is that for ϵ=1/30 is the motions are lower with non-linear restoring for periods between 6.2 s and 6.5 s. Then from 6.5 s to 6.7 s is it opposite, with the non-linear restoring resulting in the largest motions.

The time-varying restoring coefficient shows similarities to the Duffing equation, which is briefly described in section 2.6.1. The frequency response from a Duffing oscillator also results in a sudden drop in response, as can be observed in Figure 8.27 and 8.28 for the cases with non-linear restoring. However, this needs to be studied further to understand the possible connection.

Correction Set 1

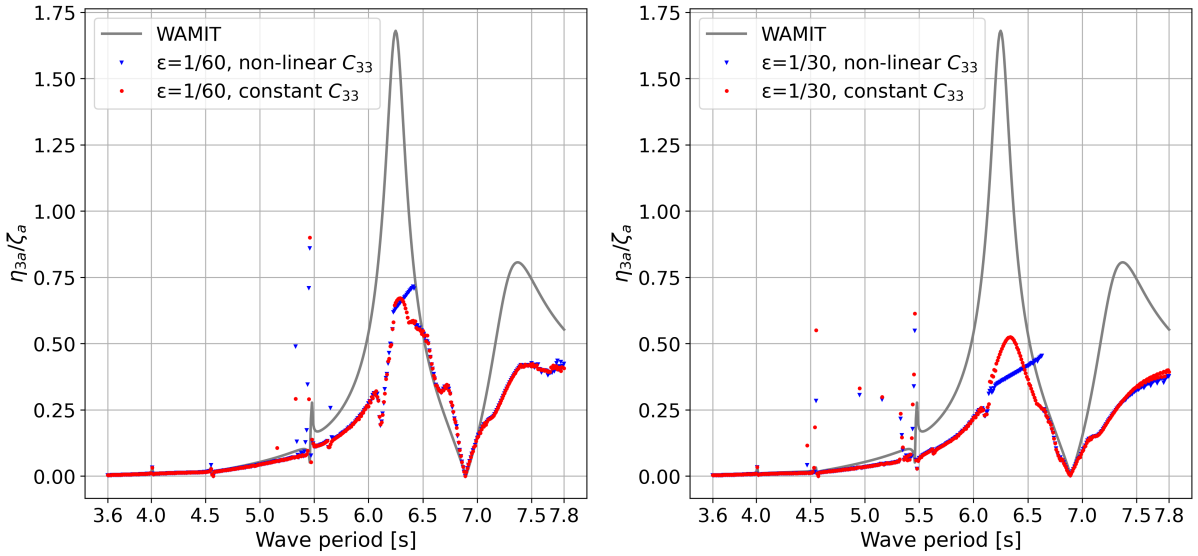

(a) $\epsilon = 1/60$ **(b)** $\epsilon = 1/30$

Figure 8.27: Effect of non-linear restoring, C_{33}, with correction set 1.

Correction Set 2

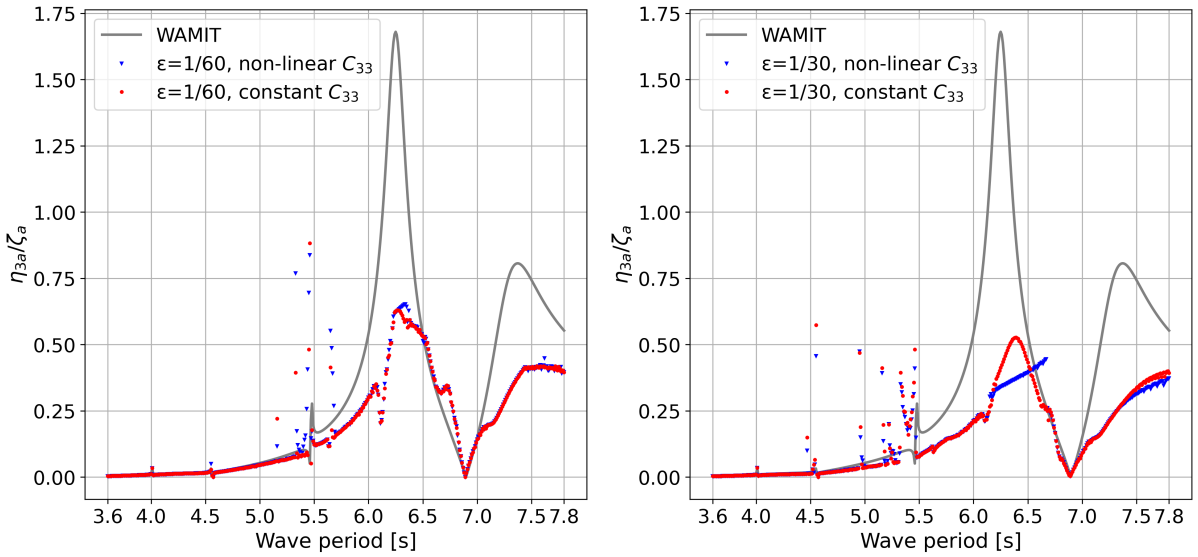

(a) $\epsilon = 1/60$ **(b)** $\epsilon = 1/30$

Figure 8.28: Effect of non-linear restoring, C_{33}, with correction set 2.

Chapter 9

Conclusion and Further Work

The non-linear motions of Ocean Farm 2 at inspection draught have been studied with a three-step approach:

1. The linear potential flow solver WAMIT was used for calculating the linear motions.
2. Non-linear effects from wave overtopping and deck flooding were found in experiments and CFD simulations. Both the experiments and CFD were performed on a box with dimensions corresponding to the cross-section of Ocean Farm 2's bottom pontoons. A top extension was attached on top of the pontoon to prohibit wave overtopping and flooding. The results were compared with pontoon without top extension to calculate non-linear correction factors.
3. The linear solution was combined with the non-linear correction factors, from the experiments and CFD by use of strip theory, in a time-domain simulator to estimate the motion RAOs including the non-linear effects.

In addition, the main theory behind the methods and the results has been outlined. The respective chapters have presented the methodology and setups behind the experiments, numerical CFD simulations and WAMIT calculations.

9.1 Conclusion

The linear surge, heave and pitch motion RAOs have been computed by WAMIT. The heave RAO shows two peak periods, with the largest at wave periods of 6.25 s. However, cancellation effects are believed to occur around the resonance period, thus causing reduced resonance heave motions and splitting the heave motion peak into two separate peaks.

The numerical CFD simulations and experiments correspond well to the wave-induced forces. The CFD resulted in slightly lower first harmonic horizontal forces and slightly higher first harmonic vertical forces compared with the experiments. However, difficulties in simulating small amplitude waves with CFD resulted in them not being run. The lowest wave simulated had a period of 1.0 s and steepness of 1/60.

Lower normalized wave-induced horizontal and vertical forces were found for increased wave steepness, which also caused increased wave overtopping. For the horizontal forces, this can be explained by the fact that a higher degree of wave overtopping means more of the water flow over the pontoon rather than being stopped and having much of its energy absorbed. For the vertical forces, the water flowing over the pontoon result in a vertical force pushing the pontoon down and thus reducing the positive vertical force.

The vertical forces were also compared to the pontoon model with a top extension attached, which prevented the wave overtopping effect. The results showed a significant reduction in excitation forces depending on the incident wave amplitude. The largest wave resulted in, for the pontoon with top extension, around 37 % lower forces compared to the pontoon with top extension.

Added mass and damping were found from forced heave oscillation both with and without the top extension. Significant pontoon deck flooding occurred for motion amplitude to freeboard ratios above 1.4, which caused increased added mass and damping.

The time-domain simulator combined the linear results from WAMIT with correction factors for added mass, damping and excitation. In addition, the restoring stiffness also took changing water plane areas into account. The non-linear heave motions were generally reduced, and the resonance period shifted slightly towards higher wave periods due to the non-linear effects.

The time-domain simulator showed difficulties solving the coupled surge and pitch motions for some wave periods. However, there is no reason to believe that the conclusion for surge and pitch would differ from the one reached for heave, i.e. lower motions. The reason is that the findings of increased added mass and damping while lower excitation forces from the wave overtopping and pontoon deck flooding should contribute to lower motions.

9.2 Further Work

The work done in this thesis has resulted in a better understanding of the non-linear motions of the Ocean Farm 2 at inspection draught. The non-linear heave motions have been estimated and presented as RAOs. However, there still remain unanswered questions which require further work.

Firstly, the time-domain simulator for surge and pitch should be investigated closer to make it work for all wave periods. Thereafter, non-linear correction factors should be applied to estimate the non-linear motions in the same manner as for heave.

The wave-induced forces on the pontoon model from irregular sea should be studied. The real-world sea-state does not consist of regular waves, so the experiment should also look into these effects.

The possible connection between the non-linear restoring effects and the Duffing equation needs to be studied further to better understand the phenomenon. It is also possible that no such connection exists.

A parametric study with different pontoon geometries should also be performed to understand better the effects of different draughts, freeboards and widths of the pontoon. This could also result in an optimal geometry to reduce the motions.

Lastly, model tests of the complete structure should be considered. The approach used in this thesis, using corrections found for the pontoon 2D cross-section on the 3D structure using strip-theory, is a simplification that should be verified. However, the model should have quite a large scale to correctly model the overtopping effects with the low freeboard of 0.30 m, in the order of around the same scale used in this thesis, 1:36. This will ultimately result in a large model.

Bibliography

[1] FAO. The state of world fisheries and aquaculture 2020. https://doi.org/10.4060/ca9231en, 2020.

[2] Norsk Industr. Veikart for havbruksnÆringen. https://www.norskindustri.no/siteassets/dokumenter/rapporter-og-brosjyrer/veikart-havbruksnaringen_f41_web.pdf, 2017.

[3] Theoharris Koftis and Panayotis Prinos. Experimental study on wave overtopping of floating breakwaters. 2006.

[4] Kwang-Leol Jeong and Young-Gill Lee. Numerical simulations of two-dimensional floating breakwaters in regular waves using fixed cartesian grid. *Int. J. Nav. Archit. Ocean Eng.*, 12(6):206–218, 2014.

[5] David Short. Investigation into the Capabilities of Linear Theory for Numerical Modelling of Wave-Body Interactions for a 2D Heaving Buoy. Master's thesis, NTNU, Trondheim, Norway, 2017.

[6] O. M. Faltinsen. *Sea loads on ships and offshore structures.* The Press Syndicate of the University of Cambridge, 1993.

[7] M. Rahman. Fundamentals concerning stokes waves. *Transactions on Engineering Sciences*, 9, 1996.

[8] OpenFOAM. Stokes ii. https://www.openfoam.com/documentation/guides/latest/doc/guide-wave-regular-stokesii.html. Accessed: 12.11.2021.

[9] Le Mehaute. *An introduction to hydrodynamics and water waves.* Springer Science and Business Media, 2013.

[10] Robert G. Dean and Rober A. Dalrymple. *Water Wave Mechanincs for Engineers and Scientists*, volume 2. World Scientific Publishing Co. Pte. Ltd., 1991.

[11] Steven A Hughes. *Physical Models and Laboratory Techniques In Coastal Engineering (Advanced series on ocean engineering, volume 7).* Singapore: World Scientific Publishing Co. Pte. Ltd, 1993.

[12] Carl M.Larsen, Erin P. Bachynski, Trygve Kristiansen, and Dag Myrhaug. *TMR4182 Marine Dynamics compendium.* Department of Marine Technology, NTNU, 2021.

[13] George Lindfield and John Penny. *Numerical Methods, Solution of Differential Equations.* Elsevier Inc., 2019.

[14] OpenFOAM. Openfoam®: Open source cfd : Documentation. https://www.openfoam.com/documentation/guides/latest/doc/index.html. Accessed: 03.12.2021.

[15] OpenFOAM. Interfoam. https://openfoamwiki.net/index.php/InterFoam. Accessed: 25.11.2021.

[16] Erin Polic Bachynski. Scaling and experimental methods for offshore wind turbines, 2021. Lecture Note: Integrated Dynamic Analysis of Wind Turbines.

[17] Odd M. Faltinsen and Alexander N. Timokha. *Sloshing*. Cambridge University Press, 2009.

[18] WAMIT Inc. Wamit user manual, version 7.4. https://www.wamit.com/manualupdate/v74_manual.pdf.

[19] OpenFOAM. Stokes ii tutorial case. https://develop.openfoam.com/Development/openfoam/-/tree/master/tutorials/multiphase/interFoam/laminar/waves/stokesII. Accessed: 31.05.2022.

[20] OpenFOAM. Openfoam®: Pressure-inlet outlet velocity. https://www.openfoam.com/documentation/guides/latest/doc/guide-bcs-outlet-pressure-inlet-outlet.html. Accessed: 31.05.2022.

[21] P. Schmitt, C. Windt, J. Davidson, J. V. Ringwood, and T. Whittaker. Beyond vof: alternative openfoam solvers for numerical wave tanks. *Journal of Ocean Engineering and Marine Energy*, 2020.

[22] SIMSCALE. K-omega and k-omega sst. https://www.simscale.com/docs/simulation-setup/global-settings/k-omega-sst/, 2022.

[23] B. Devolder, P. Troch, and P. Rauwoens. Performance of a buoyancy-modified k-ω and k-ω sst turbulence model for simulating wave breaking under regular waves using openfoam. *Coastal Engineering*, 2018.

[24] ASM. Ws10 cable extension position sensor. https://www.asm-sensor.com/en/produkt-detail-import-en.html?page=120&prod=14, 2022.

[25] WIKIPEDIA. Butterworth filter. https://en.wikipedia.org/wiki/Butterworth_filter, 2022. Accessed: 25.05.2022.

Appendix

Appendix A

WAMIT

A.1 RAO

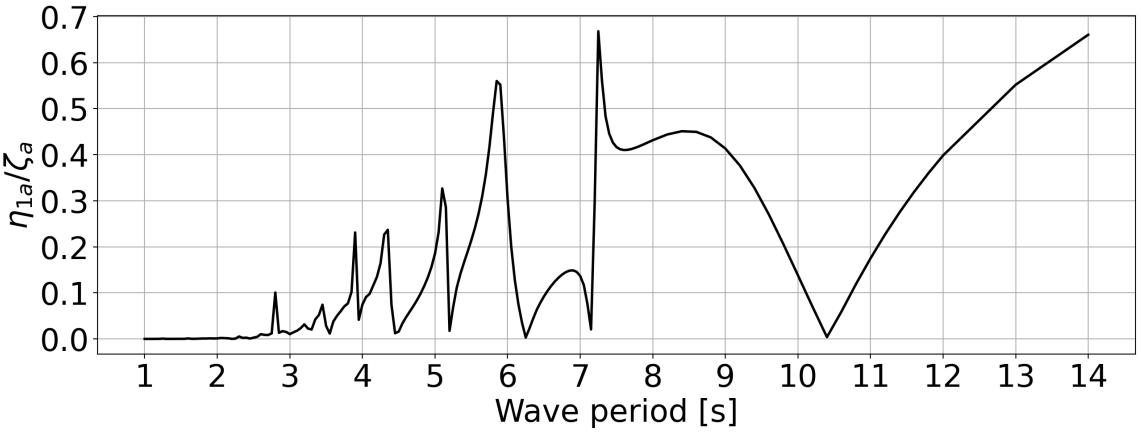

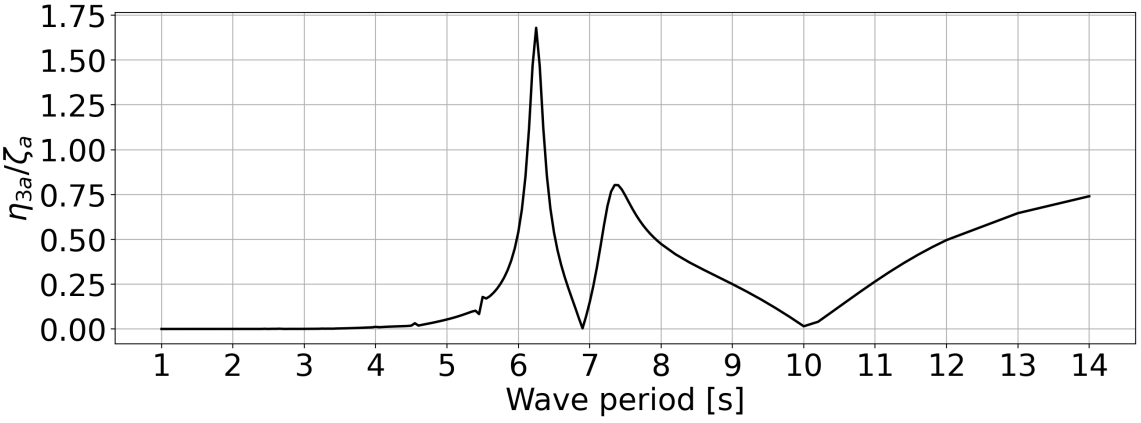

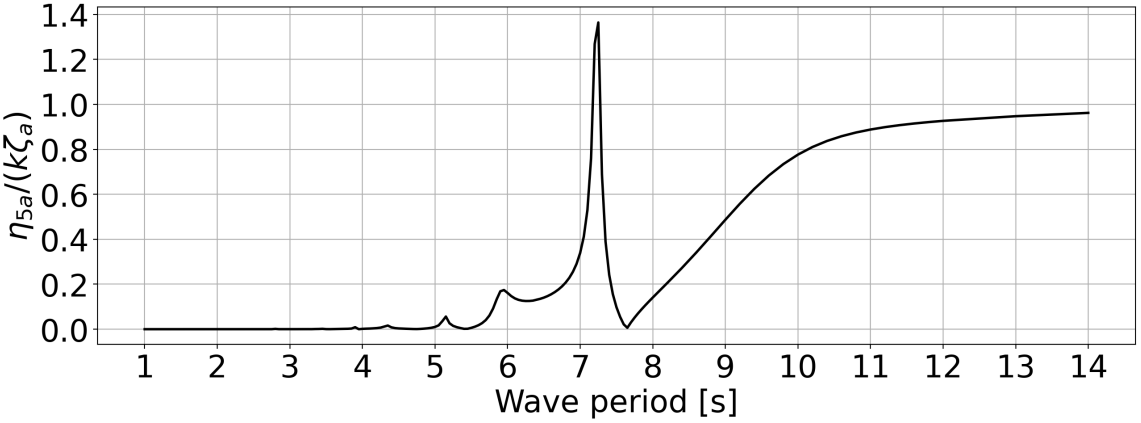

A.2 Added mass

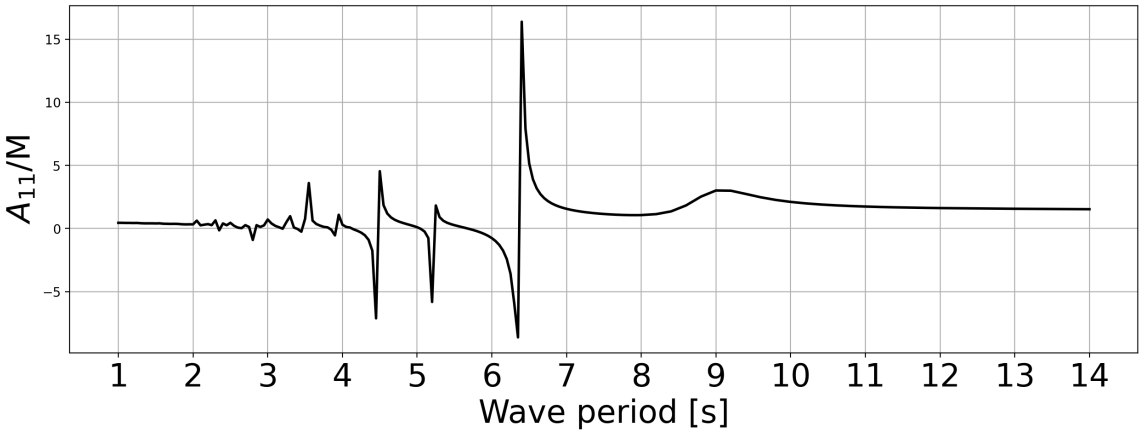

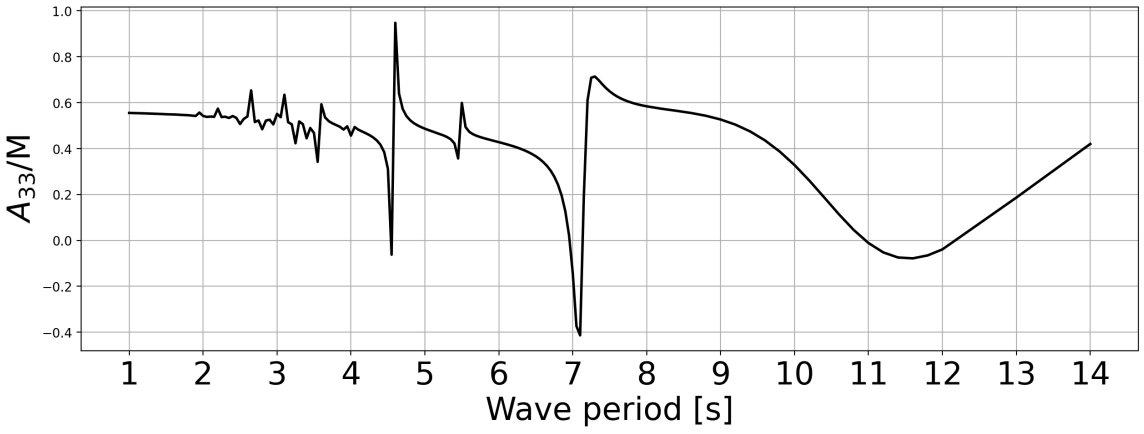

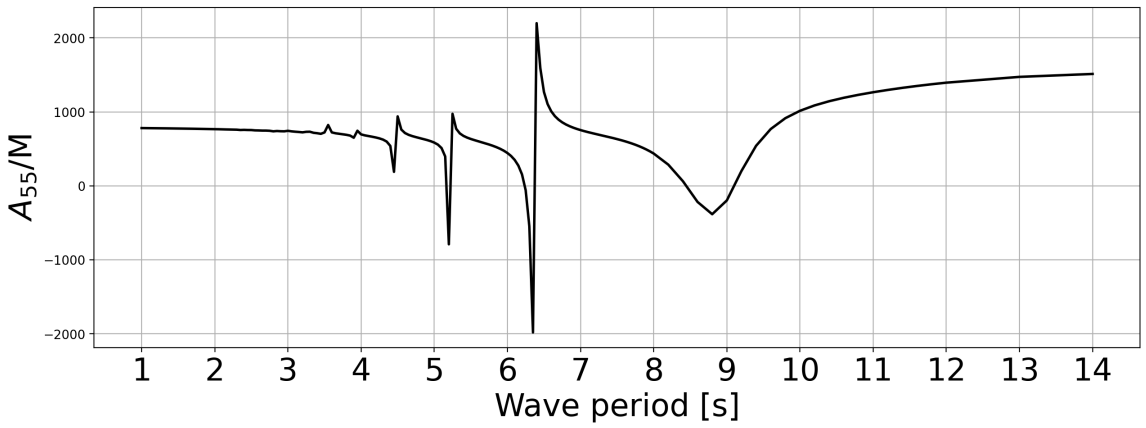
A_{55}/M
2000
1000
0
−1000
−2000
1 2 3 4 5 6 7 8 9 10 11 12 13 14
Wave period [s]

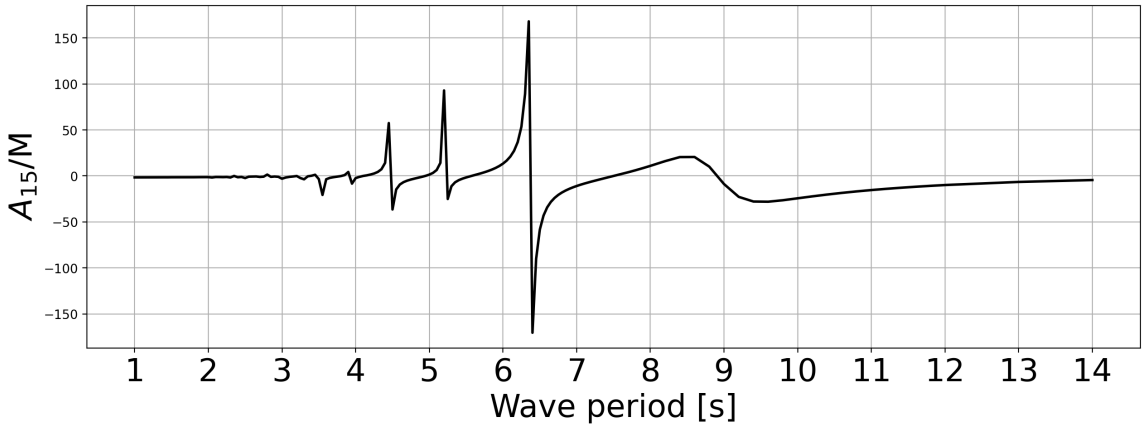
A_{15}/M
150
100
50
0
−50
−100
−150
1 2 3 4 5 6 7 8 9 10 11 12 13 14
Wave period [s]

A.3 Damping

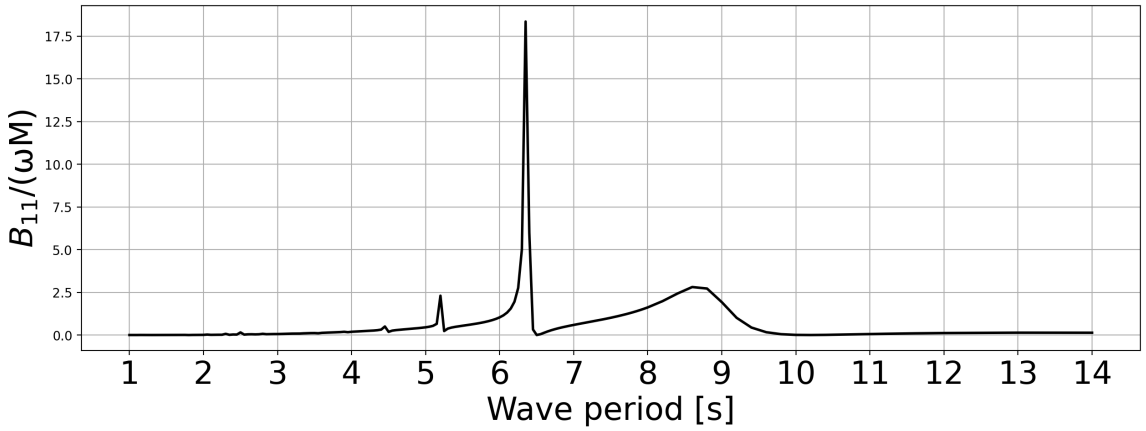
$B_{11}/(\omega M)$
17.5
15.0
12.5
10.0
7.5
5.0
2.5
0.0
1 2 3 4 5 6 7 8 9 10 11 12 13 14
Wave period [s]

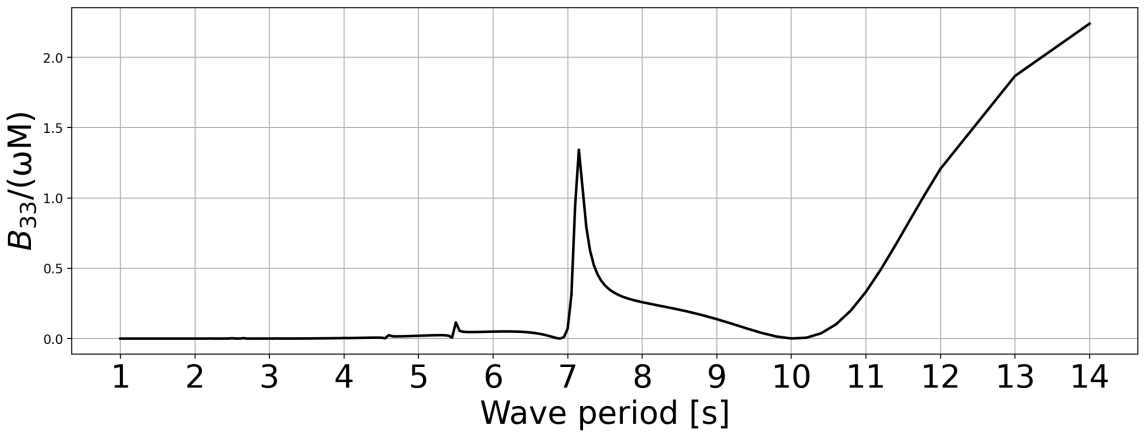
$B_{33}/(\omega M)$
2.0
1.5
1.0
0.5
0.0
1 2 3 4 5 6 7 8 9 10 11 12 13 14
Wave period [s]

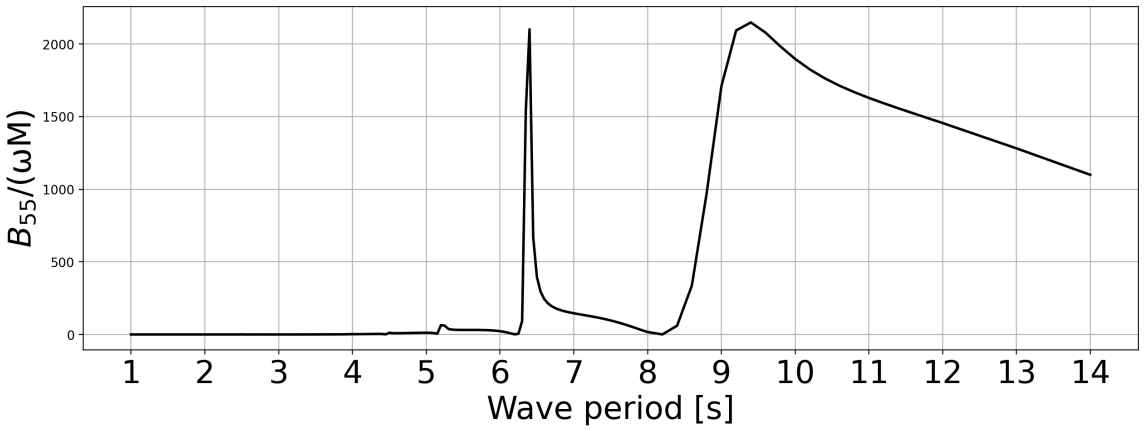
$B_{55}/(\omega M)$
2000
1500
1000
500
0
1 2 3 4 5 6 7 8 9 10 11 12 13 14
Wave period [s]

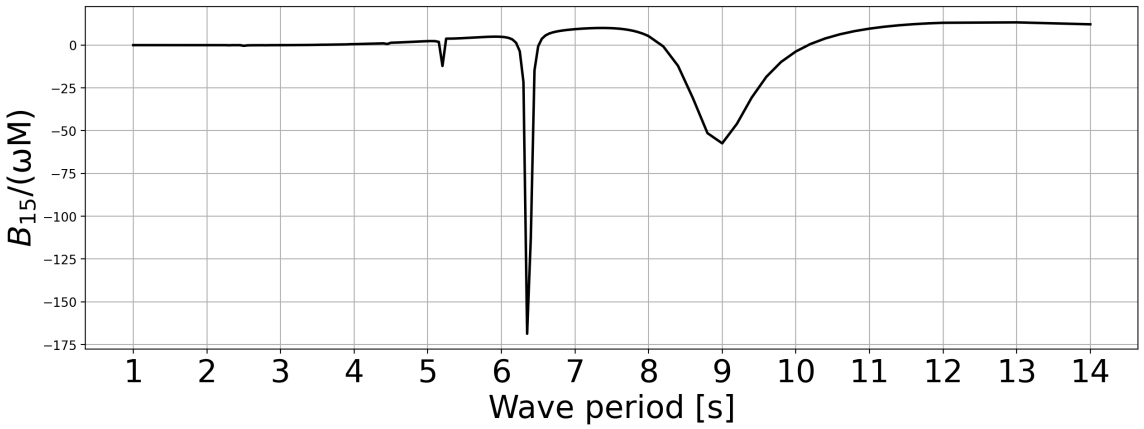
$B_{15}/(\omega M)$
0
−25
−50
−75
−100
−125
−150
−175
1 2 3 4 5 6 7 8 9 10 11 12 13 14
Wave period [s]

A.4 Excitation force

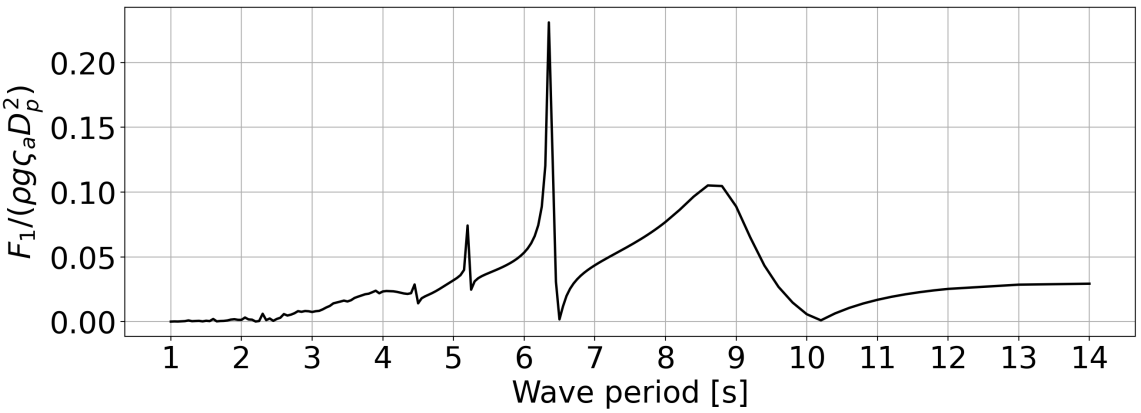

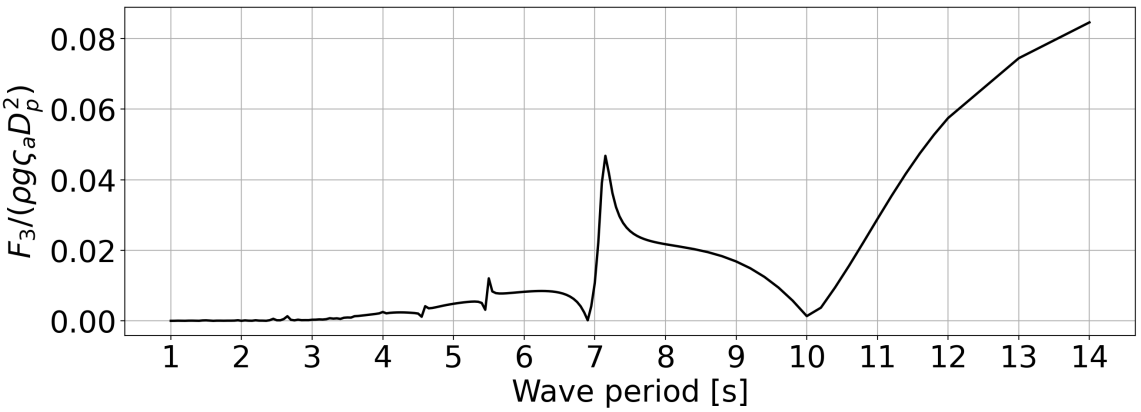

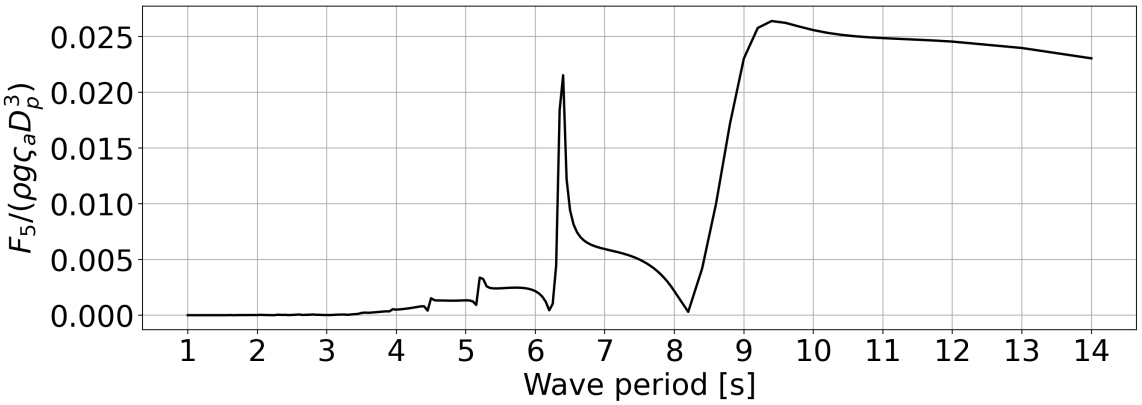

A.5 Pressure Distribution

A.5.1 T=6.25 s

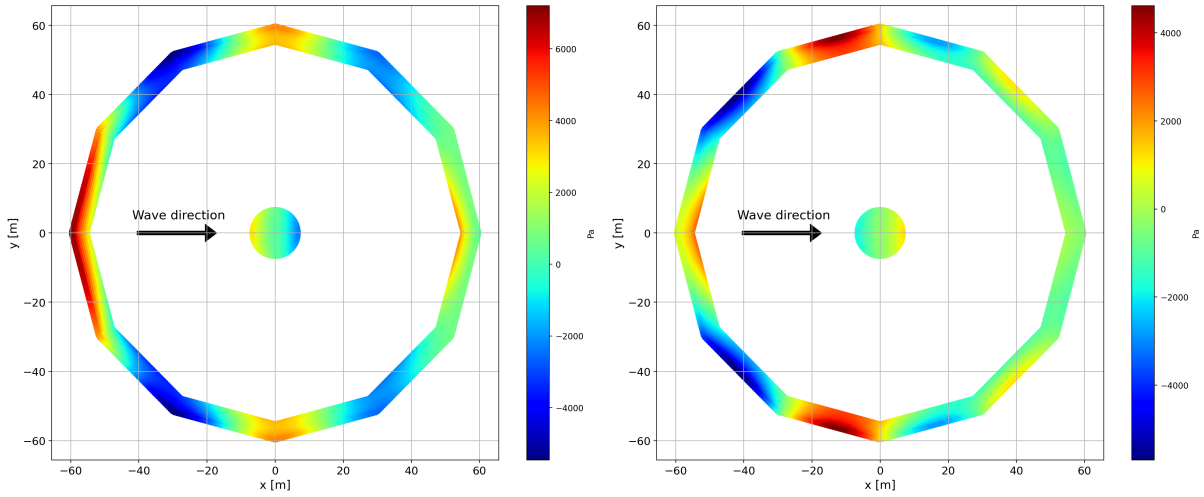

(a) Real part **(b)** Imaginary part

Figure A.1: Diffraction pressure

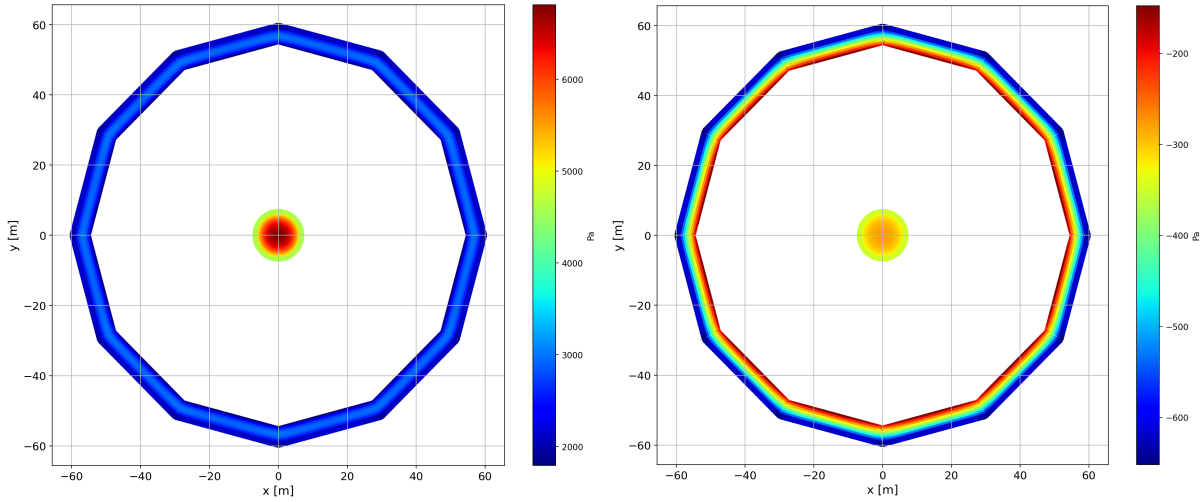

(a) Real part **(b)** Imaginary part

Figure A.2: Radiation pressure

A.5.2 T=6.90 s

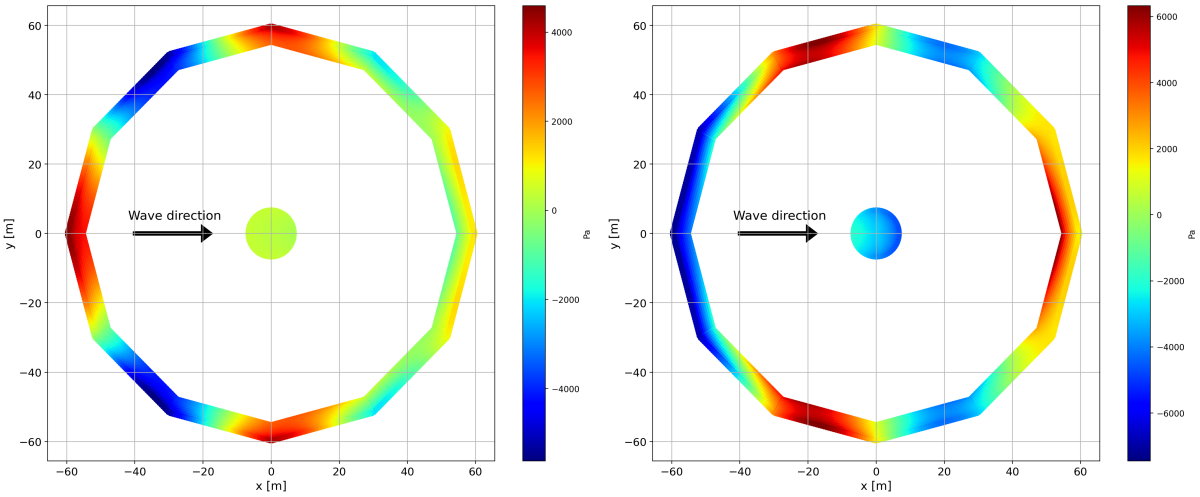

(a) Real part **(b)** Imaginary part

Figure A.3: Diffraction pressure

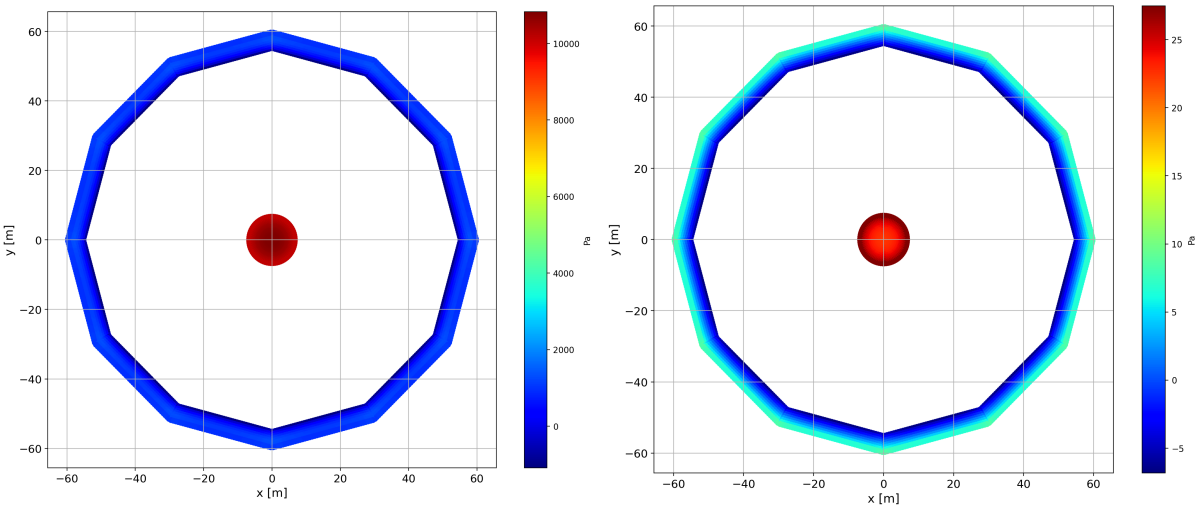

(a) Real part **(b)** Imaginary part

Figure A.4: Radiation pressure

A.5.3 T=7.35 s

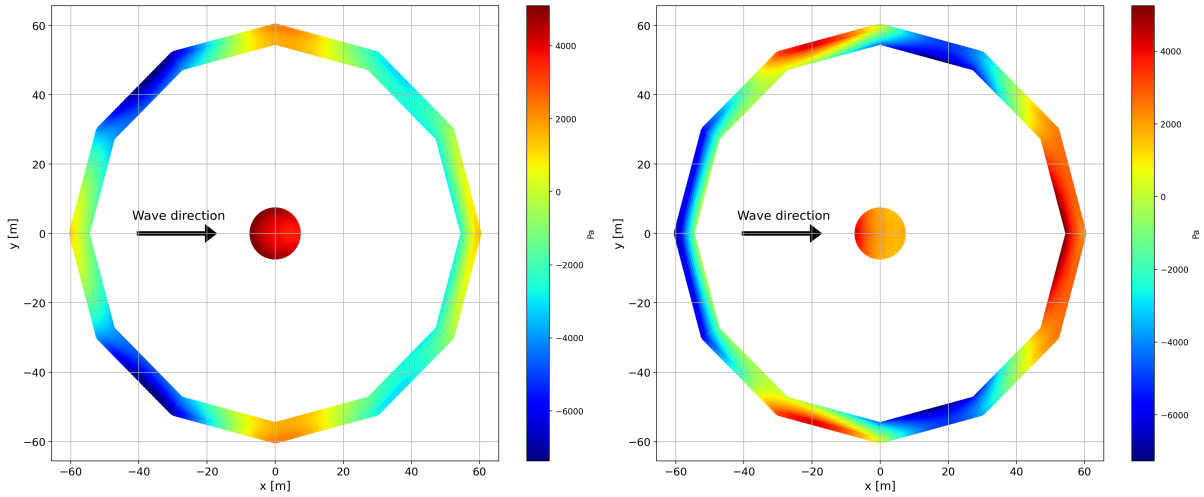

(a) Real part **(b)** Imaginary part

Figure A.5: Diffraction pressure

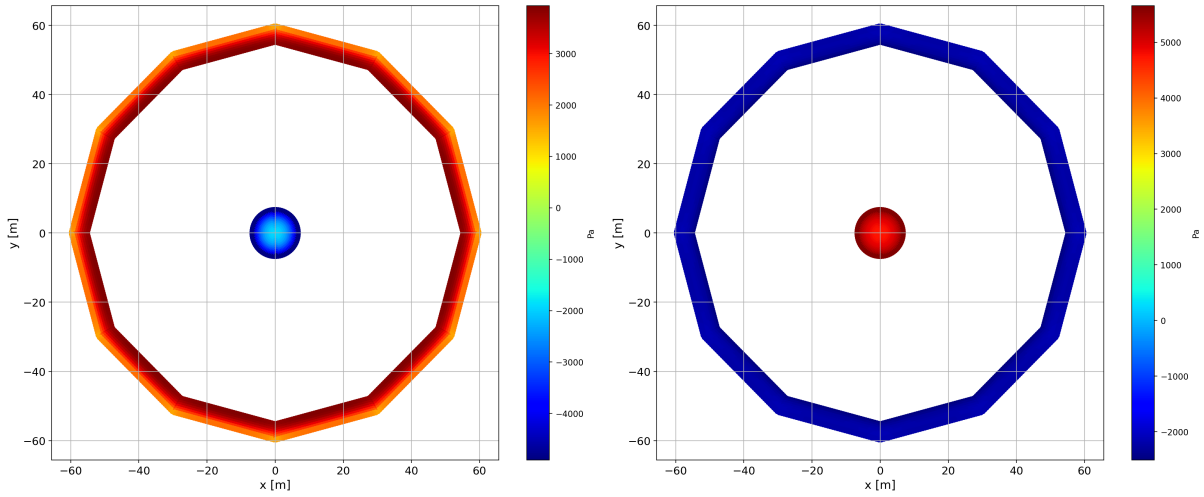

(a) Real part **(b)** Imaginary part

Figure A.6: Radiation pressure

Appendix B

Validity of potential wave theories

Taken from Le Mehaute, 2013 [9].

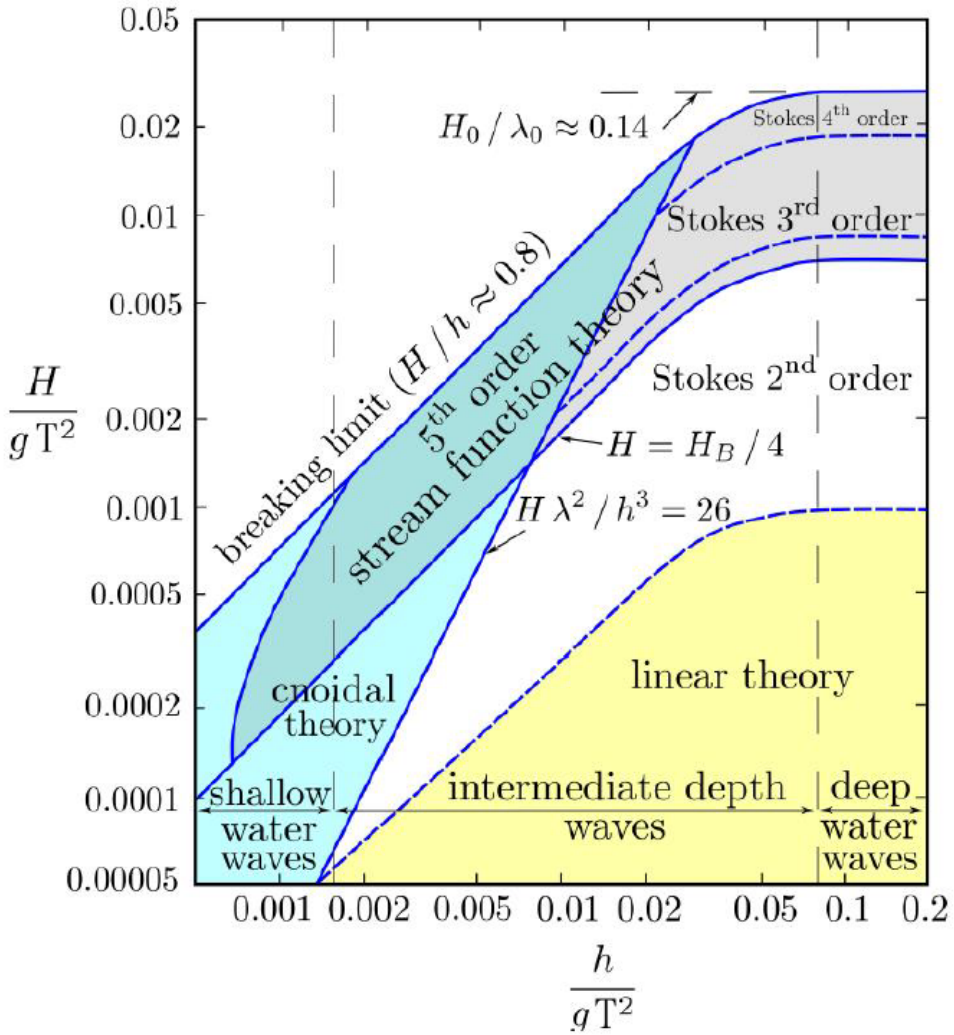

Appendix C

OpenFOAM mesh convergence

The waves presented in this appendix have ϵ=1/45, T=1.3 and H=0.058 m.

C.1 Band passed between 0.2ω and 4ω

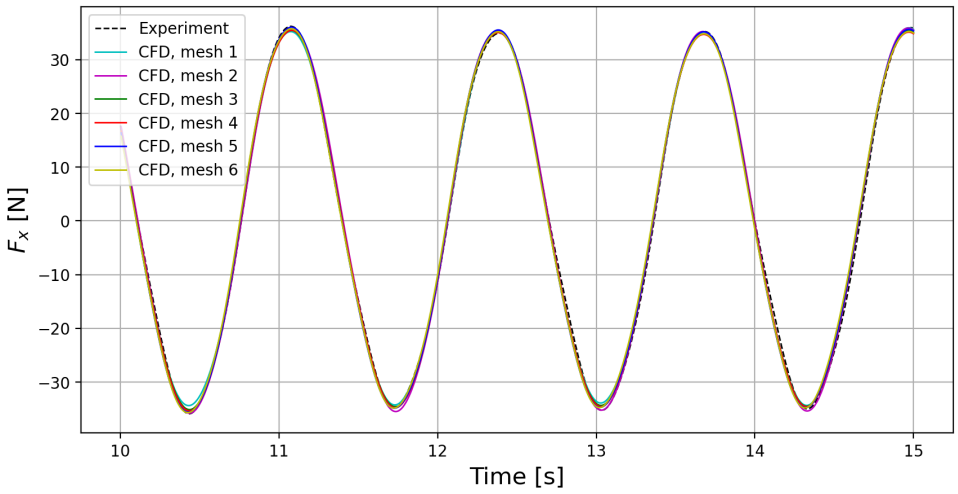

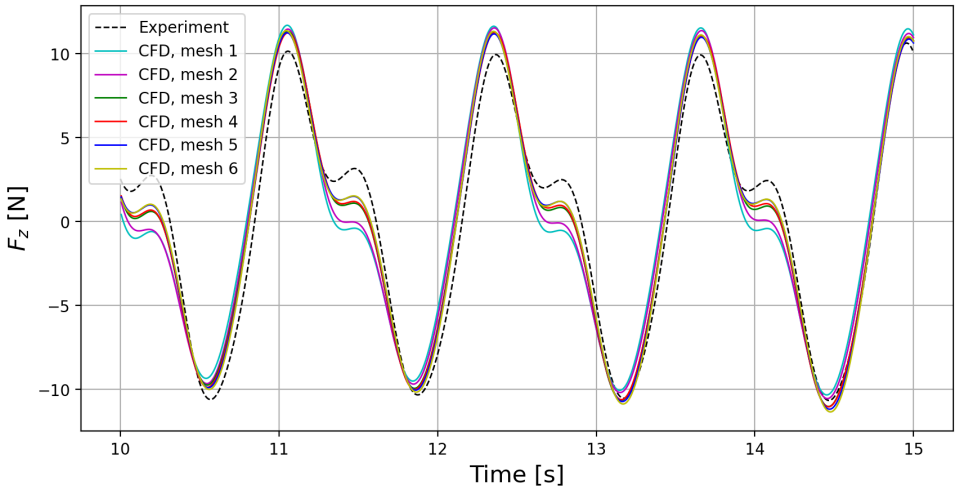

C.2 1st harmonic

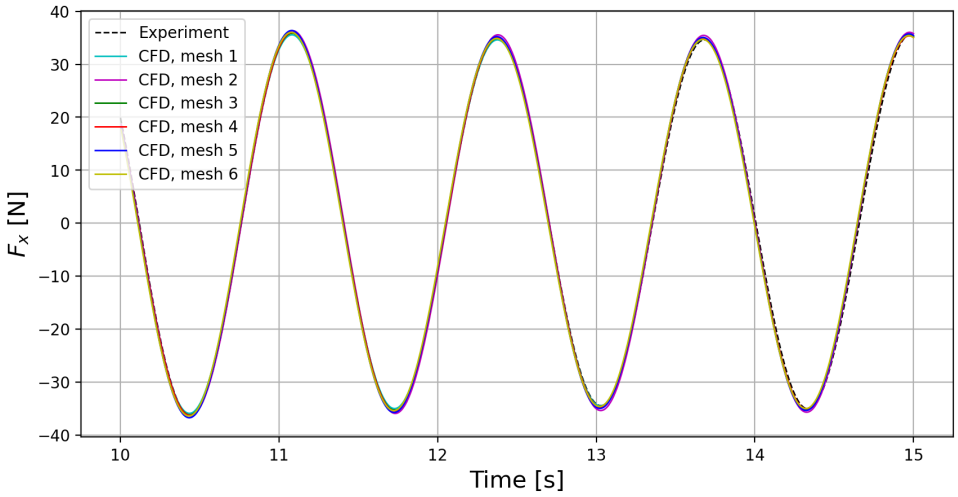

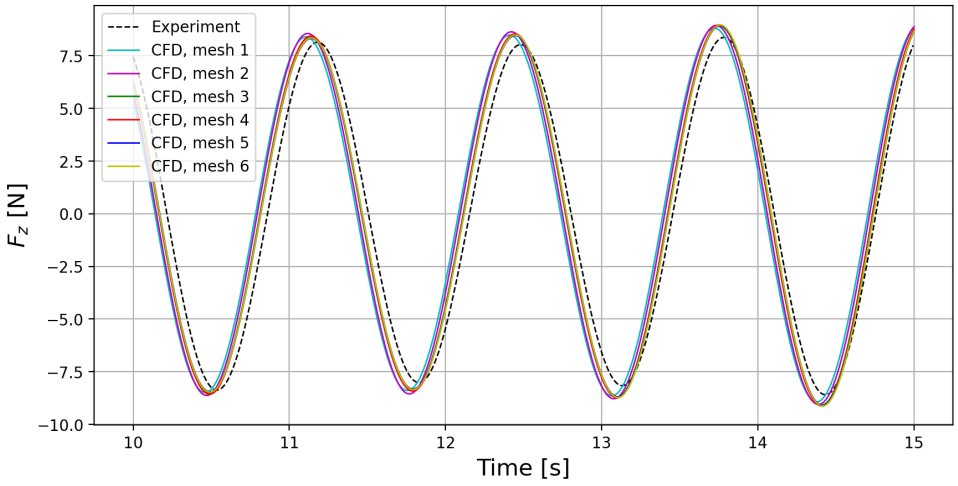

C.3 2nd harmonic

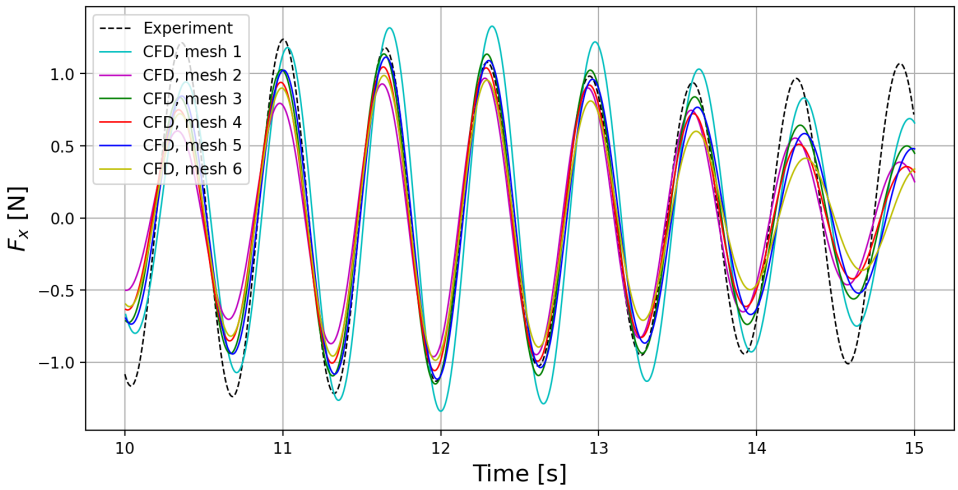

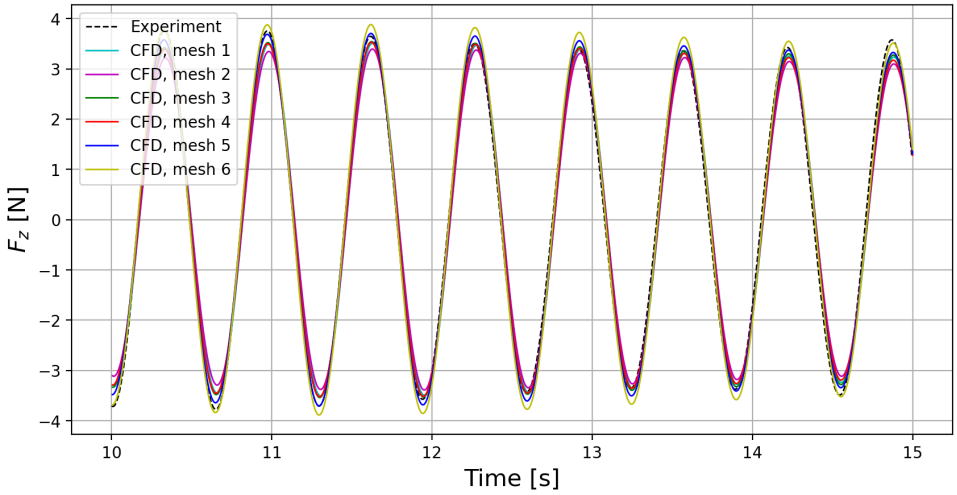

C.4 3rd harmonic

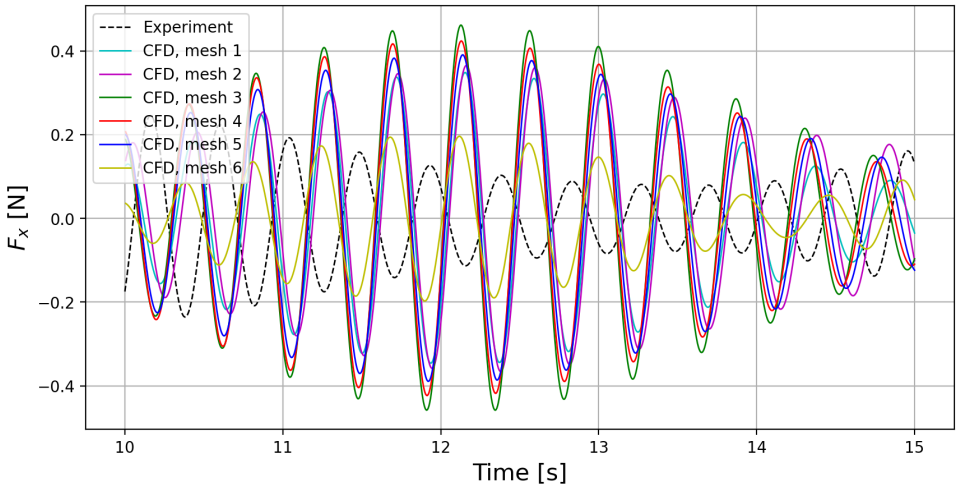

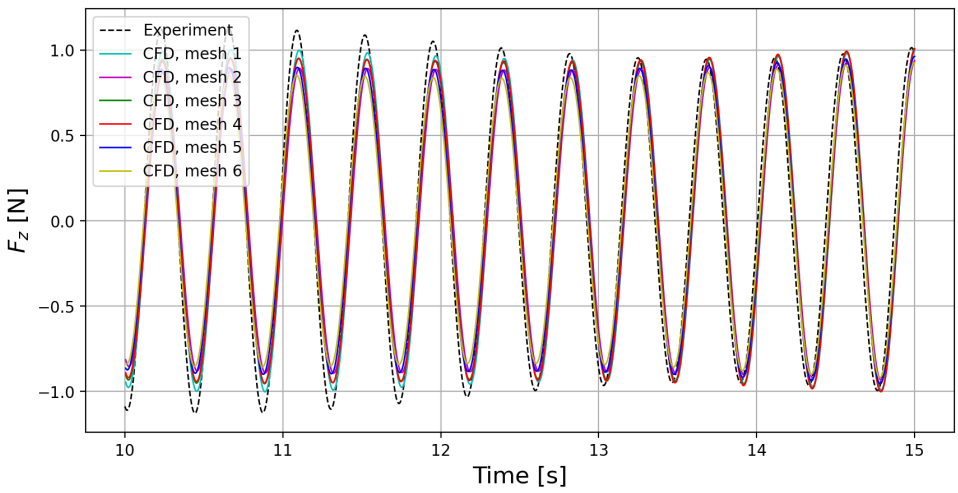

Appendix D

OpenFOAM time step convergence

D.1 Band passed between 0.2ω and 4ω

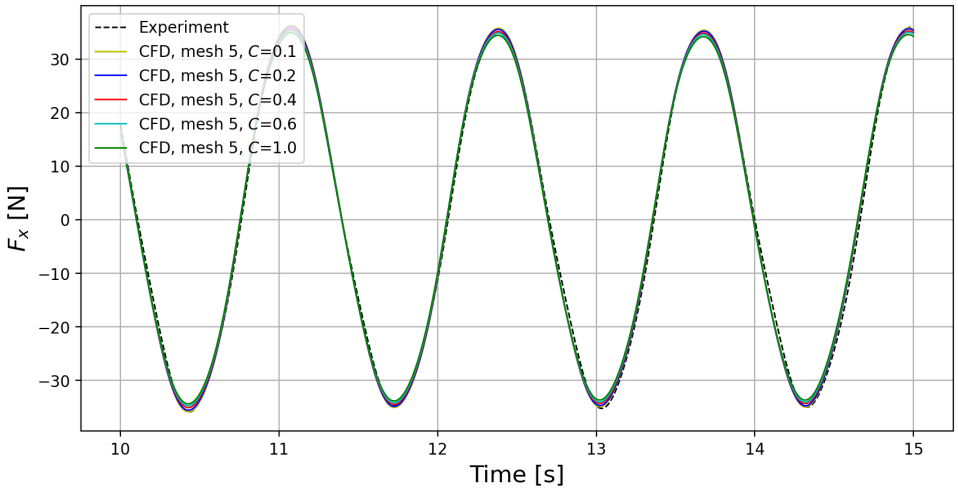

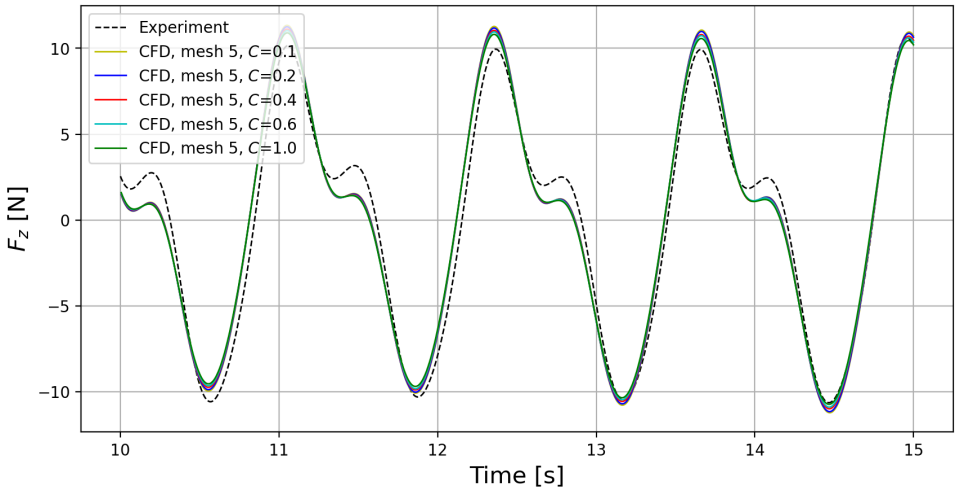

Appendix E

Experiment vs. CFD, wave profile

The waves shown below have ϵ=1/45,T=1.3 s and H=0.058 m.

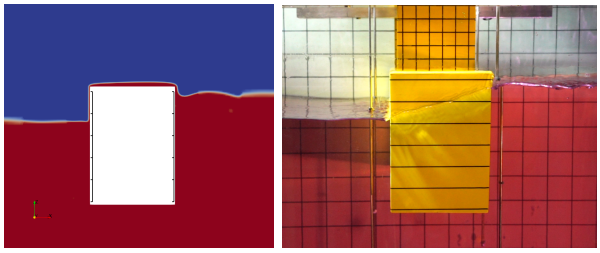

t=10.5 s

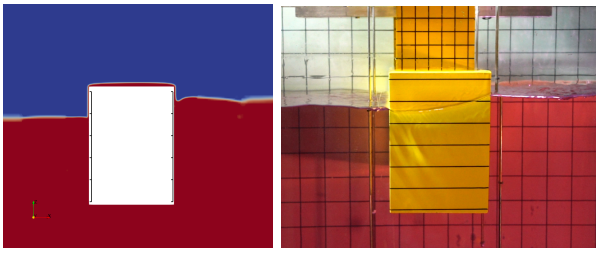

t=10.6 s

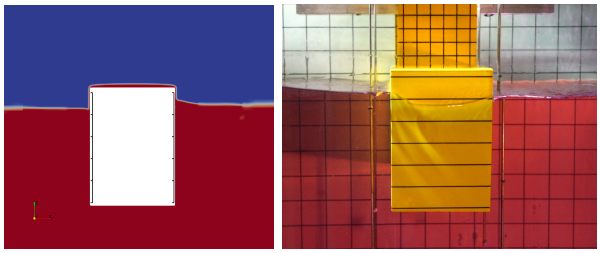

t=10.7 s

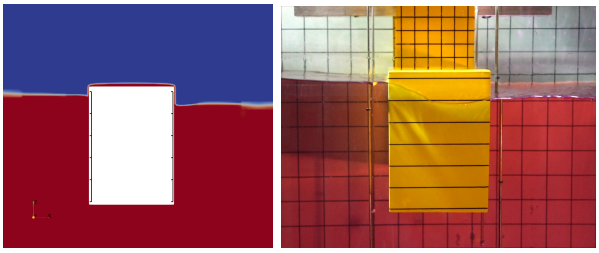

t=10.8 s

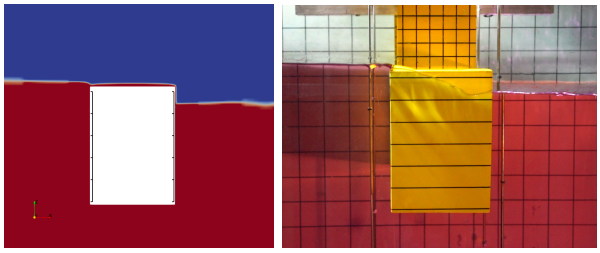

t=10.9 s

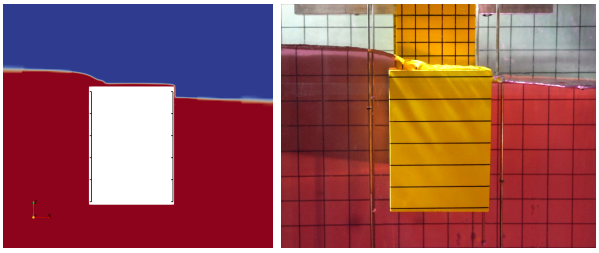

t=11.0 s

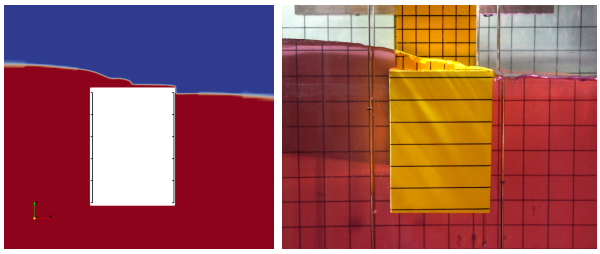

t=11.1 s

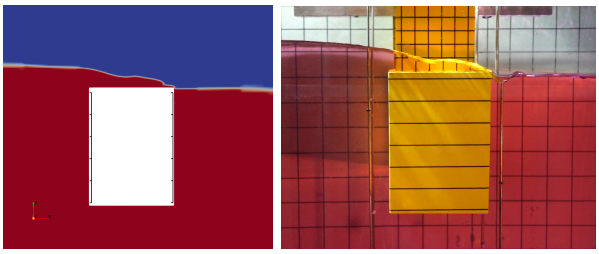

t=11.2 s

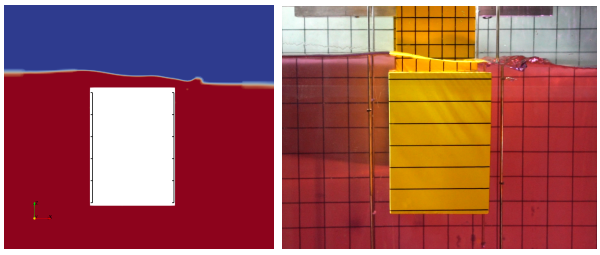

t=11.3 s

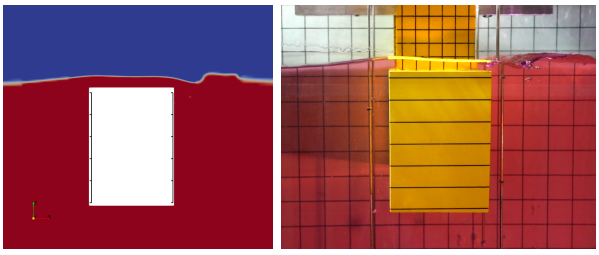

t=11.4 s

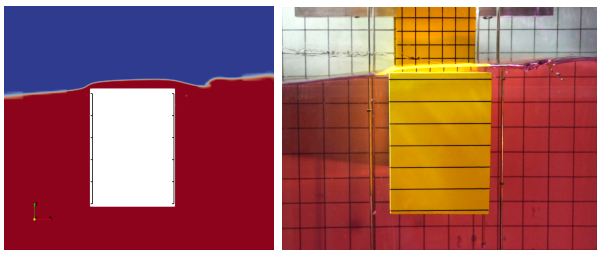

t=11.5 s

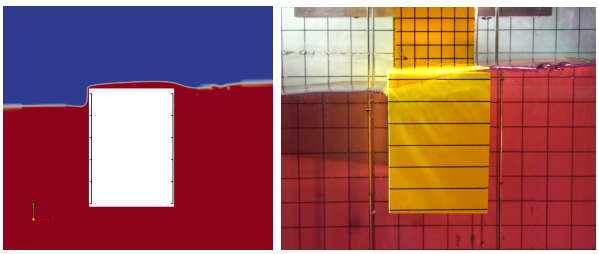

t=11.6 s

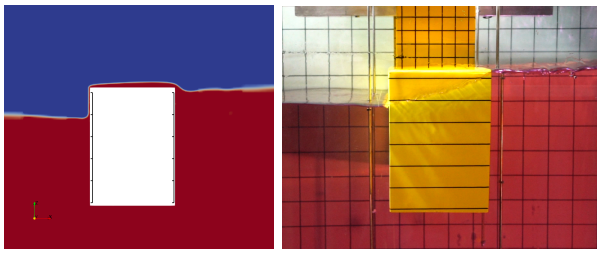

t=11.7 s

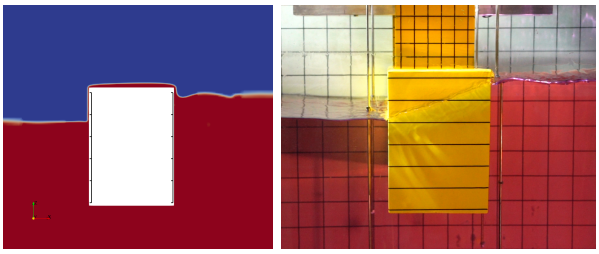

t=11.8 s

Appendix F

Maximum overtopping for steepness of 1/30

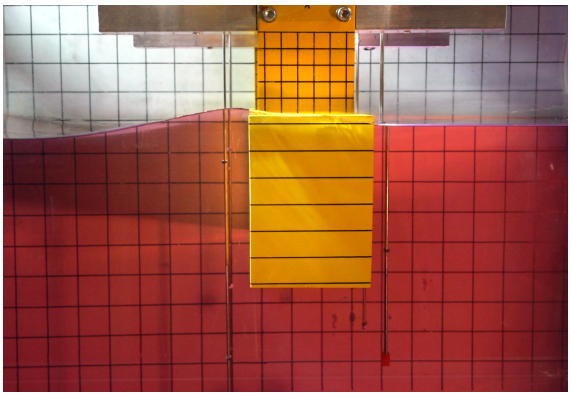

(a) T=0.6 s

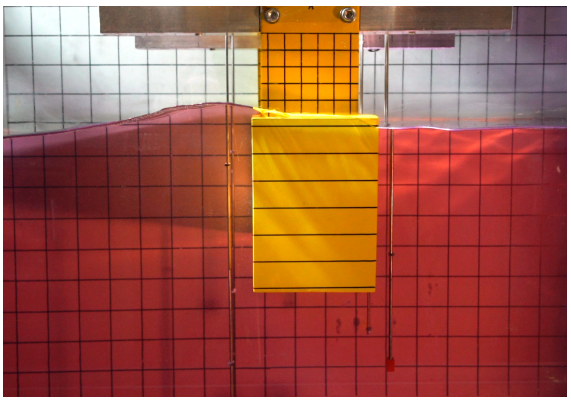

(b) T=0.7 s

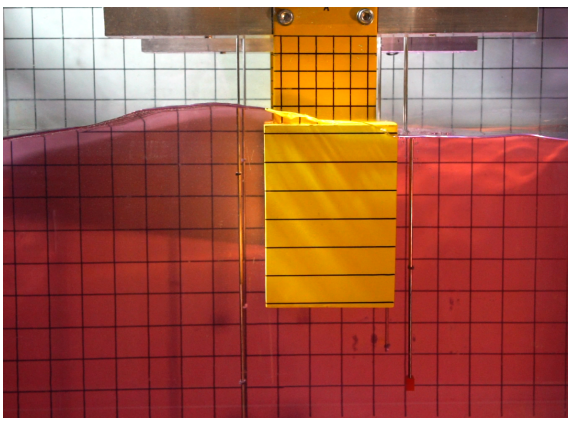

(c) T=0.8 s

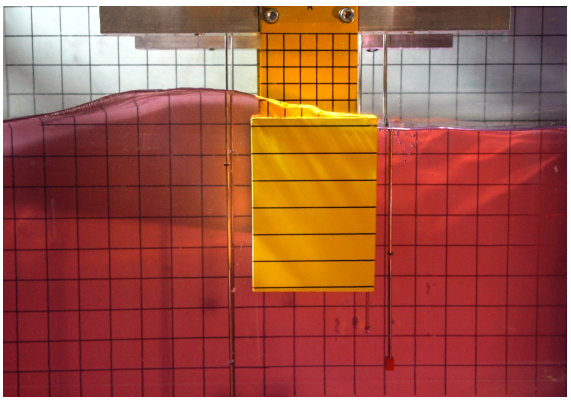

(d) T=0.9 s

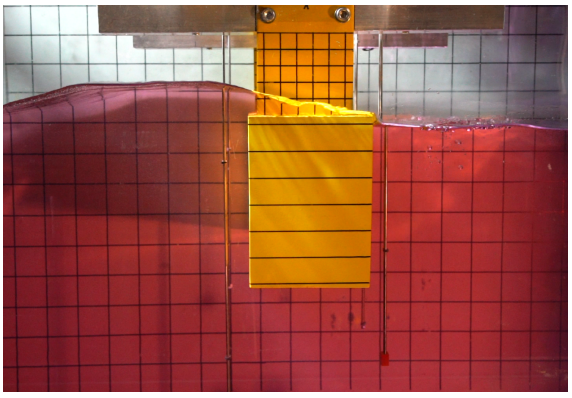

(e) T=1.0 s

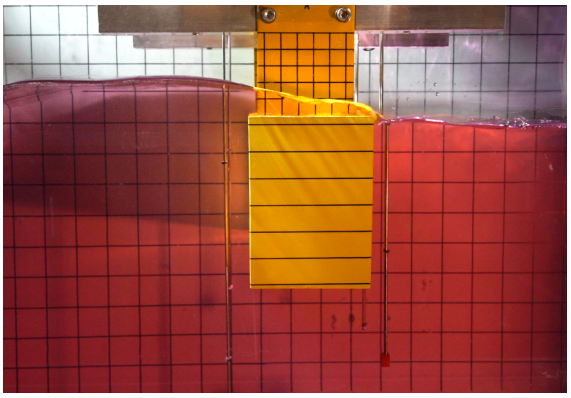

(f) T=1.1 s

(g) T=1.2 s

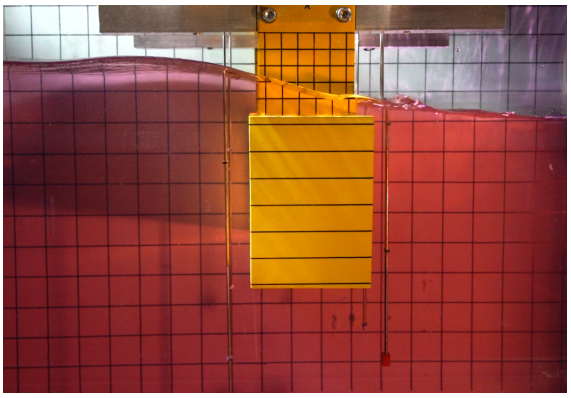

(h) T=1.3 s

Appendix G

Simulator time series

The presented time series in this appendix is from a wave with ϵ=1/60, T=4.0 s and H=0.42 m.

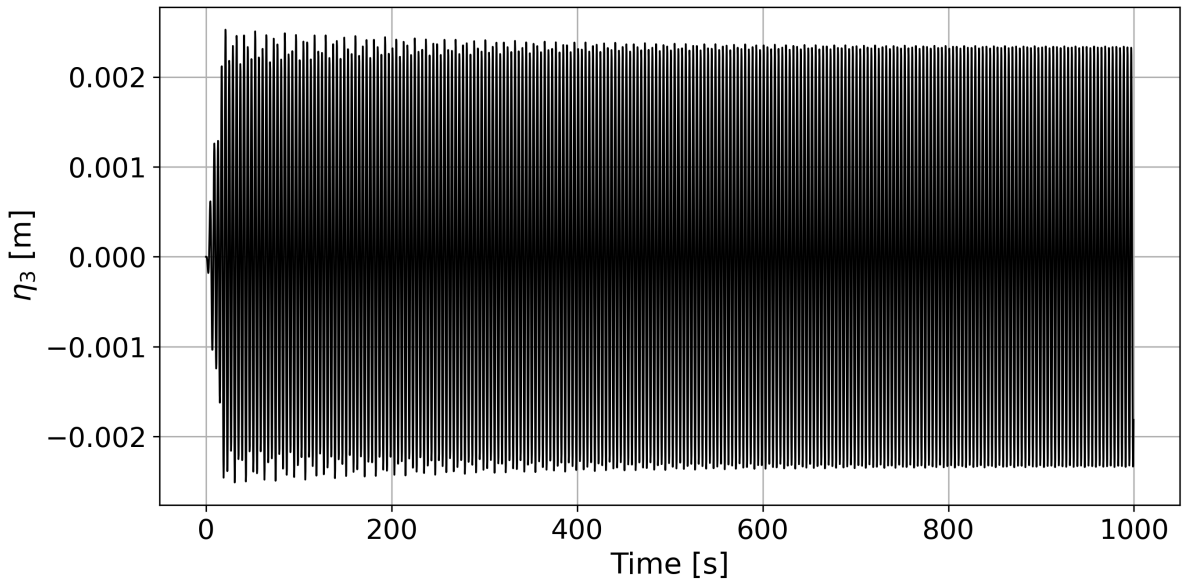

Eivind Hexeberg Dysvik

Experimental and Numerical Study of Non-Linear Motions of Ocean Farm 2 at Inspection Draught

NTNU
Norwegian University of
Science and Technology

GLOBAL
MARITIME